Nanoscale

rsc.li/nanoscale

ROYAL SOCIETY
OF **CHEMISTRY**
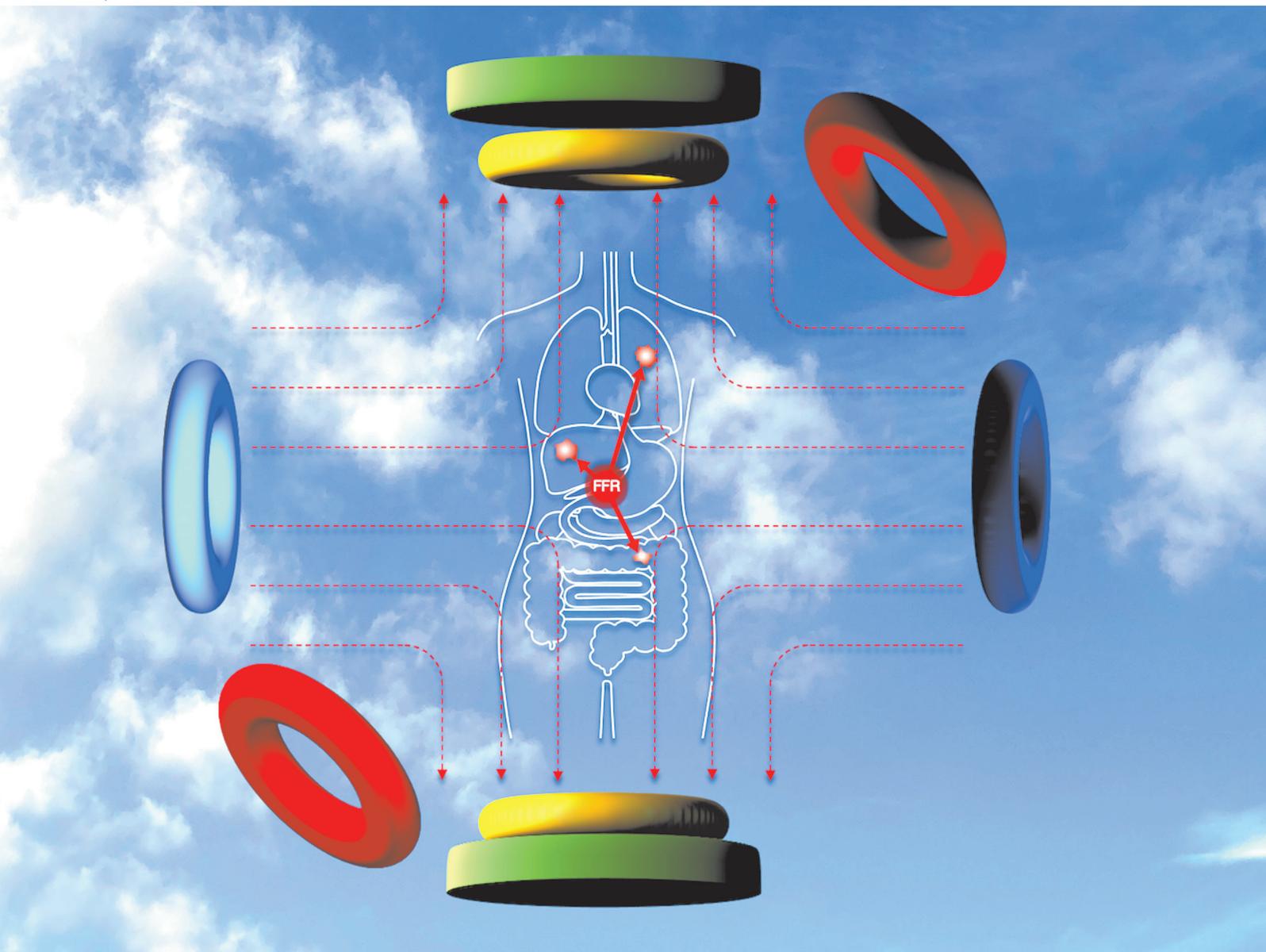
REVIEW ARTICLE
Nguyễn Thi Kim Thanh *et al.*
Magnetic particle imaging: tracer development and the
biomedical applications of a radiation-free, sensitive, and
quantitative imaging modality

NCNST

Magnetic particle imaging: tracer development and the biomedical applications of a radiation-free, sensitive, and quantitative imaging modality

Stanley Harvell-Smith, [ID] [a,b] Le Duc Tung[a,b] and Nguyen Thi Kim Thanh [ID] *[a,b]

Magnetic particle imaging (MPI) is an emerging tracer-based modality that enables real-time three-dimensional imaging of the non-linear magnetisation produced by superparamagnetic iron oxide nanoparticles (SPIONs), in the presence of an external oscillating magnetic field. As a technique, it produces highly sensitive radiation-free tomographic images with absolute quantitation. Coupled with a high contrast, as well as zero signal attenuation at-depth, there are essentially no limitations to where that can be imaged within the body. These characteristics enable various biomedical applications of clinical interest. In the opening sections of this review, the principles of image generation are introduced, along with a detailed comparison of the fundamental properties of this technique with other common imaging modalities. The main feature is a presentation on the up-to-date literature for the development of SPIONs tailored for improved imaging performance, and developments in the current and promising biomedical applications of this emerging technique, with a specific focus on theranostics, cell tracking and perfusion imaging. Finally, we will discuss recent progress in the clinical translation of MPI. As signal detection in MPI is almost entirely dependent on the properties of the SPION employed, this work emphasises the importance of tailoring the synthetic process to produce SPIONs demonstrating specific properties and how this impacts imaging in particular applications and MPI's overall performance.

[a]*Biophysics Group, Department of Physics and Astronomy, University College London, Gower Street, London WC1E 6BT, UK. E-mail: ntk.thanh@ucl.ac.uk*
[b]*UCL Healthcare Biomagnetic and Nanomaterials Laboratories, University College London, 21 Albemarle Street, London W1S 4BS, UK*

1. Introduction

MPI is a recently developed tracer-based modality which has emerged as a promising diagnostic and therapeutic tool with wide ranging potential applications. It can generate 2D projection images or true 3D tomographic images that are easily

Stanley Harvell-Smith

Stanley Harvell-Smith obtained his Master's First Class degree in Chemistry from the University of Sheffield in 2020. Currently, he is studying for a Ph.D. under the supervision of Professor Nguyen T. K. Thanh based at the UCL Healthcare Biomagnetics and Nanomaterials Laboratories. His interests are focused on the synthesis and characterisation of magnetic nanoparticles for MPI, and applications in theranostics such as magnetic hyperthermia.

Le Duc Tung

Dr Le Duc Tung received his Ph.D. degree in Physics from University of Amsterdam in 1998. He was a postdoctoral fellow at the University of New Orleans (2001–2003), University of Warwick (2003–2007), University of Liverpool (2007–2010). Currently he is a senior research fellow at Biophysics Group, Department of Physics & Astronomy, University College London. His research interests are in magnetism and magnetic materials and recently focused on biomedical applications of magnetic nanoparticles, with 96 scientific publications.

interpretable, stemming from their 'positive contrast', a trademark of other tracer-based techniques like positron emission tomography (PET), single-photon emission computed tomography (SPECT), and optical imaging techniques. The tracer employed by MPI are SPIONs. MPI utilises a gradient field with strong gradients and weak field strengths, and the unique, intrinsic, non-linear magnetic response of these SPIONs to the gradient field is directly detected to generate an image.

Professor Nguyễn Thị Kim Thanh, FRSC, FInstP, FIMMM FRSB (http://www.ntk-thanh.co.uk) held a prestigious Royal Society University Research Fellowship (2005–2014). She was appointed a Full Professor in Nanomaterials in 2013 at University College London. She leads a very dynamic group conducting cutting edge interdisciplinary and innovative research on the design, and synthesis of magnetic and plasmonic nanomaterials for biomedical applications. In 2019, she has been honoured for her achievements in the field of nanomaterials, and her impactful project proposal and was awarded highly prestigious Royal Society Rosalind Franklin Medal. Currently, she is Vice Dean for Innovation and Enterprise at Faculty of Maths and Physical Sciences. She published over 140 research papers, book chapters, theme issues, proceedings with total ~15 000 citations. She has been Visiting Professor at various Universities in France, Japan, Singapore. She has been invited to speak at over 270 institutes and scientific meetings. She has been chairing and organising over 45 high profile international conferences. She is Editor-in-chief of the Royal Society of Chemistry book Series, Nanoscience and Nanotechnology. She edited 7 theme issues including: (2021) Nanoscale Web themed issue on "Advanced Functional Nanomaterials for Biomedical Applications". The Royal Society (2016), Interface Focus, "Multifunctional nanostructures for diagnosis and therapy of diseases"; The Royal Society Chemistry, RSC (2014), Faraday Discussions, "Physical Chemistry of Functionalised Biomedical Nanoparticles"; RSC (2013) Nanoscale, Special issue "Functional Nanoparticles for Biomedical Applications" and Philosophical Transactions of the Royal Society A (2010), "Nanoparticles"; MDPI (2021) Biomedicines "Advanced Functional Nanomaterials for Biomedical applications". She is the sole editor of two seminal books on Magnetic Nanoparticles from Fabrication to Clinical Applications in 2012 (ISBN 9781439869321) and Clinical Applications of Magnetic nanoparticles in 2018 (ISBN 9781138051553). She is co-organising a Magnetic Carrier Meeting in Jun 2022 in London.

Nguyen T. K. Thanh

MPI is the first new imaging modality in 30 years. It was first introduced by Gleich and Weizenecker in 2005 at the Philips Research Laboratory (Germany).[31] Then from 2007, Conolly and Goodwill at the University of California, Berkeley, developed a series of prototype alternative MPI scanners based on the same basic MPI principles but different reconstruction approaches and scanning techniques.[32,33] Philips later licensed the production of their MPI systems to Bruker BioSpin AG (Switzerland), who subsequently released the world's first preclinical scanner to the market in 2013.[34] Around 2014, Magnetic Insight Inc. (USA) was founded, later becoming the second company to release a commercial pre-clinical MPI scanner in 2016. Other academic labs and companies across the world have also contributed to the development of this technology.[35–40] Until now, MPI has not been implemented clinically, but multiple groups are working on human clinical systems.[41–43]

Application of MPI has many benefits. SPIONs are a sensitive, safe, and biocompatible tracing material with potentially long physical half-lives, where the MPI signal can remain constant over long time-periods, enabling longer-term imaging of labelled cells.[18] Both the SPION tracers and the scanners themselves have an excellent safety profile, remaining ionising radiation-free. Additionally, MPI is highly applicable *in vivo* as it provides unambiguous depth-independent detection of SPIONs, with the magnetic field capable of passing transparently through any anatomical tissue or bone without any signal attenuation.[44] Also, without the presence of endogenous background signal, MPI has an essentially infinite contrast, and it can produce highly sensitive and specific images,[45] with detection limits as low as ~200 labelled cells, containing a total of 5.4 ng of iron.[26] Furthermore, MPI is truly linearly quantitative, meaning there is a strong linear relationship between the signal intensity produced and the iron content, and this close relationship holds true for even very small quantities of iron, and at any depth.[46,47] The coefficient of determination indicates the relationship is almost perfectly linear ($R^2 = 0.99$),[44] thus permitting estimation of SPION concentration in target tissues, based on just the signal intensity. Moreover, the temporal resolution of MPI is very high (<1 s),[48] allowing real-time *in vivo* imaging and the potential for immediate assistance during medical interventions.[49,50]

These well-established characteristics make MPI greatly suitable for many applications of clinical relevance, including those previously inaccessible using other imaging modalities. For successful imaging, tailored SPIONs with specific properties are required, as the signal detection in MPI is almost entirely dependent on the properties of the SPION tracer employed. As a consequence, there has been extensive research on the syntheses of novel monodispersed SPIONs, controlling the size, shape, and crystallinity of the core, whether there is any surface modification, and the aggregation state.[51–54]

Because of the fundamental importance of optimising the characteristics of the SPION for performance in MPI and its applications, the bulk of this review will comprise a comprehensive study of the current research directions in the production of MPI-tailored SPIONs, as well as an in-depth discus-

sion on the up-to-date literature for developments in the current and promising biomedical applications of this rapidly advancing technique. The key areas of focus are divided into applications in theranostics, cell tracking, and perfusion imaging. Prior to this discussion, the simplified principles of image generation in MPI are explained, along with a basic description of the physics and hardware operating within the system. Also included is a detailed comparison between the fundamental properties of MPI and other common imaging modalities with their relative advantages and disadvantages, and a detailing on the recent progress in MPI's clinical translation. Though research in MPI is still in the early stages, we hope this discussion on the major advancements and research directions in this rapidly advancing field over the past 5 years will encourage further exploration into the applications of MPI, as well as in the development of its SPION tracers.

2.   MPI background and theory

2.1.   Hardware and basic imaging principles

In this section, a simplified description of MPI's hardware and the basic principles for image acquisition and reconstruction is provided. Detailed descriptions of these methods can be found elsewhere.[31,46,55,56] To utilise the magnetic properties of SPIONs for imaging, a standard MPI system consists of three major components: a selection field, a drive field, and a receiving coil. In the first MPI scanner developed in 2005,[31] the selection field was generated through two permanent magnets positioned such that their field lines are pointing directly towards each other. This alignment produces a strong magnetic field gradient with a sensitive point located in the centre, known as the field free region (FFR), or in this case, the field free point (FFP) (Fig. 1a). The FFP is an area that is void of any magnetic field. This original scanner was able to generate

magnetic field gradients of ~3.4 T m^{-1}, however, the hardware setup in current preclinical scanners, permits gradients of up to 7 T m^{-1} to be reached.[57–59] The second component, the drive field, is an alternating magnetic field (AMF). In the original scanner, it is generated by three opposing pairs of drive field coils, one for each respective direction in space (Fig. 1b), each with an amplitude of 10 mT.[31] The AMF causes changes in the oscillations of the SPION tracers, which results in variation in their magnetisation that is subsequently detected by the receiving coil. However, the strong magnetic field gradients produced by the selection field saturate all SPIONs except those within the FFP, thus inhibiting the effect of the AMF. Therefore, just SPIONs within the FFP respond to the AMF. Here, it is important to consider the unique magnetic properties of SPIONs in the presence of an external magnetic field.[31] First, the two most commonly encountered SPION systems for MPI, single- and multi-core SPIONs, must be described, where their structural differences significantly alter the magnetic properties, resulting in nanoparticles with differing magnetic behaviour in the external AMFs applied in MPI. "Single-core" have just one magnetic core per particle, whereas "multi-core" contain several closely aggregated magnetic cores per cluster, where the cores are most often linked through dipole–dipole interactions.[60,61] Single-cores have a permanent magnetic moment, whereas, multi-cores acquire a magnetic moment in the presence of strong applied fields. Within an MPI system, when SPIONs are exposed to the strong magnetic selection fields in proximity to the magnets, both types of SPIONs are fully magnetised to a state of saturation, and therefore, do not generate an MPI signal. However, when exposed to small or no magnetic field, as in the FFP, the nanoparticles are randomly oriented and constantly oscillate. The FFP is shifted over the entire field-of-view (FOV) via rapid variation of the drive field. Whenever it crosses a SPION, the magnetic dipole of the nanoparticle flips orientation instan-
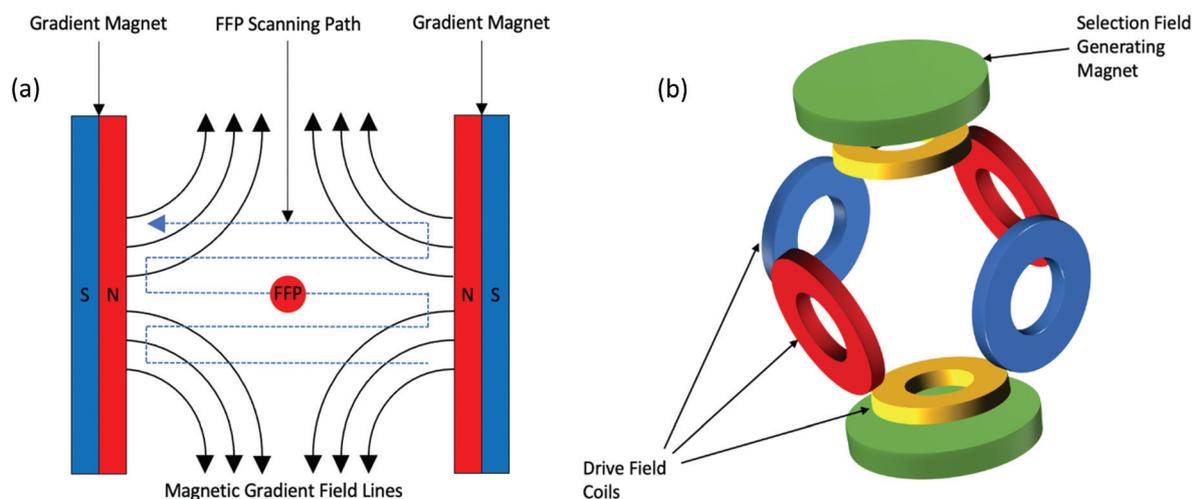

Fig. 1   (a) The magnetic gradient field generated by an MPI scanner with two permanent magnets, producing an FFP along with magnetically saturating regions. The FFP is rapidly scanned over the FOV via variation of the drive field, generating signal from the reorientation of the SPIONs magnetisation. (b) Configuration of drive field coils required to generate a drive field.

taneously to become aligned with the field lines, and in accordance with Faraday's law of induction, induces a voltage that is detected by the sensitive receiver coils. Single-core SPIONs simply orient their non-zero permanent magnetic moment in the direction of the applied field, whereas under the same conditions, multi-core SPIONs first become magnetised and then orient their induced magnetic moment in the direction of the applied field.

This concept can be utilised to generate a 2D projection image of SPION distribution, allowing for spatial encoding of the particle signal, indicating the presence and location of SPIONs within the FOV.[62,63] This spatial reconstruction process requires complex algorithms, the most well-established of which, are system function reconstruction (SFR) based processes,[31,50,56,64–69] and x-space processes.[32,44,46,55,57,59,70] These two processes rely on the same basic hardware and imaging principles, assigning the signal to a location that corresponds to the respective location of the FFP within the region of interest. The voltages induced in the coil are also linearly proportional to the concentration of SPIONs at the instantaneous location of the FFP, enabling their quantification. This linearity of signal intensity with the density of SPIONs has been confirmed in theory.[44] Furthermore, through rotation of the system around the sample, it is possible to capture 2D projection images at multiple angles, where these data can then be converted into a 3D image.

When MPI was first established, SFR-based processes were primarily employed for image reconstruction.[31,56,64,65,67–69] These processes require a pre-characterisation of the SPIONs, whose signal response is formulated into a system matrix containing Fourier harmonics of the temporal signal for all possible locations of a point source.[32] The system matrix is typically measured physically using a SPION sample,[50] but may also be estimated through application of a model.[67] Reconstruction of the image is achieved using matrix inversion and regularisation techniques. However, this inversion is often complex since the matrix is large, comprising millions of elements. Additionally, the system matrix is greatly specific to the SPION sample in solution, and thus the accuracy of reconstruction will be less if the SPION behaves differently in tissue, or if the model is inaccurate. Nowadays, x-space processes have received more research attention and are more frequently implemented.[22,71–73] In these processes, a fast reconstruction algorithm computes the MPI image without any requirement for pre-characterisation, modelling, and matrix inversions,[32] resulting in robust, real-time imaging. An x-space MPI image is reconstructed from a raw MPI signal through a simple two-step process of velocity compensation of the received signal, followed by gridding of said signal to the instantaneous position of the FFP.[70] Velocity must be compensated in the received signal as the induced signal is proportional to the instantaneous velocity of the FFP.

Recent developments have shown that MPI sensitivity can be significantly improved through application of a more expansive spatial encoding scheme. Instead of scanning the FOV with an FFP, a field free line (FFL) can be utilised.[37,74,75] An FFP integrates signal from just a small area, whereas an FFL allows for spatial encoding along a line, integrating signal from an area ∼10 times greater. This yields a correspondent theoretical sensitivity increase of a factor of 10, and an increased signal-to-noise ratio (SNR).[76] Additionally, a lower level of power consumption is required.[77] The first experimental setup of an FFL was presented by Knopp *et al.*, where the line is generated by two orthogonal Maxwell coil pairs.[78] The magnetic fields generated by the opposing coils flow in exact opposite directions, thus generating an FFP between each coil pair as before. However, superposition of the generated magnetic fields leads to production of an FFL centered along the bore axis of the scanner. Top *et al.* recently engineered the first open-sided FFL prototype MPI scanner.[79] Along with the ability to electronically scan the FOV to generate tomographic images, this open-sided design permits interaction with the subject for potential real-time interventional procedures. The results from initial 2D imaging experiments have shown that high quality images with comparatively low resolutions of 2.5 mm can be produced using very low gradient levels (0.6 T m^{-1}).

2.2. The Langevin model

In a simplified model, this non-linear magnetisation response of SPIONs in the presence of an AMF follows the classic Langevin magnetisation curve (Fig. 2a), so long as anisotropy, hysteresis effects, and any particle interactions are disregarded.[80] To explain this in terms of an ideal system of single-core SPIONs, or multi-core SPIONs, when the applied field is strong in a particular direction to one side of the particles, the magnetisation starts in a saturated state with the SPIONs aligned in the direction of the field. As the applied field is shifted across the particle, the magnetisation desaturates, eventually to a state where the applied field is ∼0 mT, and the SPIONs become randomly oriented. SPIONs have zero
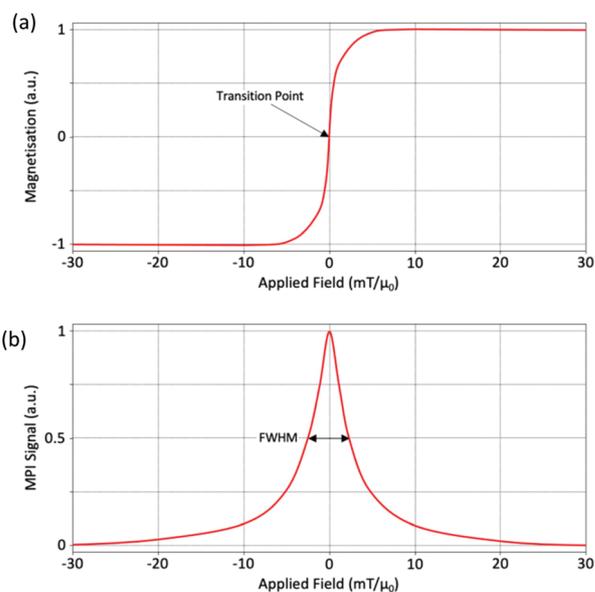

Fig. 2 (a) Langevin curve and (b) PSF for an ideal SPION.

remanence and zero coercivity, so as the applied field is further shifted across the particles, there is a linear transition in the curve, shown in Fig. 2a, and the orientation of the nanoparticles flips rapidly with respect to the externally applied AMF. Following this transition, and with a still shifting applied field, the SPIONs re-saturate to the same intensity as before once the field strength has passed a certain threshold, but with reverse polarisation and alignment. The exact opposite process occurs when shifting the applied field in the opposite direction.

In *x*-space reconstruction, the imaging effect can be described by a point spread function (PSF).[55] A PSF is generated from the differential of this Langevin behavior and provides important information about the signal produced (Fig. 2b). The PSF of a particular SPION is a measure of the change in magnetisation as a function of the applied drive field. There are two important parameters to consider when looking at a PSF: the signal intensity, which reflects the sensitivity of the nanoparticle, and the full-width at half-maximum (FWHM), which is related to the effective spatial dimensions of the signal, and thus the spatial resolution of the nanoparticle. The FWHM is often referred to as the 'nanoparticle resolution'.[81] By dividing the value for the FWHM of the PSF by the imaging gradient strength, it is possible to estimate the overall MPI spatial image resolution.[32,55] It is also possible to compare the FWHM, and thus resolutions, for two different SPIONs. To do so it is necessary to first normalise the signal obtained by the SPION concentration in the sample.

2.3. SPION relaxation

Upon application of the externally applied drive field, the dynamics of SPION magnetisation changes with the relaxation time constant, $\tau^{-1} = \tau_{\text{Brownian}}^{-1} + \tau_{\text{Néelian}}^{-1}$,[82] which is influenced by the Néel time constant ($\tau_{\text{Néelian}}$), and the Brownian time constant (τ_{Brownian}). Therefore, it can be stated that the magnetic moments of SPIONs relax to align with the external field through joint Néel and Brownian processes.[83–85] The Néel time constant describes the internal flip in magnetisation of the particles from one orientation to another without physical rotation of the particle. This occurs on a timescale of nanoseconds. Whereas the Brownian time constant describes the

physical rotation of the particle in space without a change in the internal magnetisation of the particle. This rotation happens on a scale of microseconds. Both time constants are affected by different parameters.[83,84] The Néel relaxation process is primarily affected by temperature fluctuation, the particle's composition and size, effective magnetic anisotropy, and any interdomain interactions within the particles. Conversely, the Brownian relaxation process, whilst also effected by temperature fluctuation and particle size, is influenced by the hydrodynamic volume of the SPIONs, the local microenvironment and the liquid medium viscosity of the immediate surrounding. Though both relaxation mechanisms coexist and often take place simultaneously, in general, SPIONs with smaller core sizes exhibit Néel relaxation to guide the dynamic magnetic responses of SPIONs and produce their signal in MPI, whereas larger core size SPIONs are instead Brownian relaxation dominant.[83,85] For further information on these processes, the interested reader should refer to a review written by Krishnan.[86]

3. Comparison of MPI to other *in vivo* imaging modalities

Each *in vivo* imaging technique has its own advantages and disadvantages depending on the application scenario. Table 1 illustrates a basic comparison of the qualities of MPI with other widely applied clinical and pre-clinical modalities. Some of the primary comparative advantages of MPI that can be inferred are its true quantification, high sensitivity and temporal resolution, and radiation-free labelling.

3.1. Nuclear medicine

One of the more popular non-invasive imaging modalities that draws easy comparisons to MPI in terms of its properties is nuclear medicine.[87–89] SPECT and PET scans are the two most frequently applied nuclear medicine imaging modalities, with significant clinical potential in that they are highly quantitative, and show great tissue penetration capability.[90,91] Both MPI and nuclear medicine are highly sensitive and operate through

Table 1 Comparison of MPI to other common clinical imaging modalities. Adapted with permission of Elsevier, and the American Society of Neuroradiology, from ref. 48, and ref. 62, respectively; permissions conveyed through Copyright Clearance Center, Inc

Modality	Contrast agents/ tracer	Type of labelling	Sensitivity	Spatial resolution	Temporal resolution	Quantitation	Patient risk	Cost
MPI	SPIONs	Hot spot	0.1 μM	<1 mm	<1 Second	Yes	Heating and peripheral nerve stimulation	Medium
^{1}H MRI	Gd, Mn, SPIONs	Contrast	mM	25–100 μm	Seconds to hours	No	Heating and peripheral nerve stimulation	High
PET	Radionuclides (*e.g.*, ^{18}F, ^{68}Ga)	Hot spot	pM	2–4 mm	Minutes	Yes	Ionising radiation	High
SPECT	radionuclides (*e.g.*, ^{111}In, ^{99m}Tc)	Hot spot	pM	3–10 mm	Minutes	Yes	Ionising radiation	Medium
CT	iodine	Contrast	mM	50–200 μm	Seconds	Yes	Ionising radiation	Medium
US^a	microbubbles	Contrast	mM	1 mm	<1 Second	No	Heating and cavitation	Low

^{a} Ultrasound.

a 'hot spot' detection mechanism of their tracers within a sample. The primary difference between MPI and these techniques, however, is the tracing modality. MPI makes use of SPION tracers, whereas nuclear medicine detects radioactive tracer agents or isotopes. Whilst both MPI and nuclear medicine are highly sensitive with no background signal nor signal attenuation from the tissues, the radionuclides used in PET and SPECT have shorter half-lives on the order of minutes to hours (*e.g.*, PET tracer: $t_{1/2}$(^{18}fluorodeoxyglucose (FDG)) = 2 h; SPECT tracer: $t_{1/2}$(^{99m}Tc) = 6 h),[92] in comparison to that of SPIONs which has enabled researchers to track the location of SPION-labelled cells for longer time periods (see section 4.2).[26] Additionally, SPIONs do not produce harmful ionising radiation as with radionuclides.[87,89,92] The shelf life of SPIONs are also orders of magnitude longer, obviating the need for preparation of the tracers immediately before patient use.[93] It's also worth noting that the production costs of SPIONs are significantly lower than those of radionuclides.[93]

3.2. Magnetic resonance imaging (MRI)

Another prevalent modality easily comparable to MPI is MRI. It is an anatomical technique that operates through measurement of tissue-dependent proton-spin relaxation times, showing great soft tissue contrast and high values of spatial resolution (25–100 μm).[77,91,94,95] One of the major differences between MRI and MPI is in the physics required for signal generation.[46,91,96] MRI utilises a strong field strength, weak gradients, and images across a high uniform magnetic field, whereas MPI utilises a weak field strength, strong gradients and images in the previously described FFR, as generated by the gradient field. Visualising the change in magnetisation *via* Faraday's law with a receiver coil in MPI is not dissimilar to the process for image generation in MRI. However, unlike MRI, the magnetisation change in MPI is of electronic, rather than nuclear magnetisation.[97] This contributes to a higher sensitivity in MPI, as the electronic magnetisation of iron detected in MPI is 22×10^6 times stronger than that of the nuclear magnetisation of water detected in MRI.[92,98] On another note, where the SPIONs employed by MPI act as a tracing modality detected *via* 'hot spots', the SPIONs that may be employed by MRI act as contrast agents, where the contrast generated is from proton density and the relaxation effects of protons in the vicinity of the particles.[99]

MRI contrast agents are generally differentiated as either "positive" T_1-weighted contrast agents or "negative" T_2 (or T_2*)-weighted contrast agents, where each class manifests proton-spin relaxation times in different ways.[100,101] T_1-weighted contrast agents shorten longitudinal spin–lattice relaxation times, generating an overall bright image. Conversely, T_2-weighted agents shorten transverse spin–spin relaxation times, generating an overall dark image. SPIONs have many favourable chemical and physical properties that benefit application in MRI, including great magnetic characteristics, targeting capability, limited toxicity, and a unique biodistribution and pharmacokinetic profile. The development of these nanoparticles as MRI contrast agents results in better, safer alternatives to

the conventional, toxic, gadolinium-based paramagnetic agents.[102–106] A number of different parameters including core shape, hydrodynamic diameter, aggregation, and coating choice influence the longitudinal and transverse relaxation times of SPIONs, but the most important determination as to whether SPIONs can be implemented as T_1- or T_2/T_2*-weighted contrast agents is their core size.[107] Generally, larger SPIONs (≥5 nm) function as T_2/T_2* contrast agents, whereas smaller SPIONs (≤4 nm) function as T_1 contrast agents. The properties of SPIONs ideal for MPI is discussed further in section 4.1. Generally, SPIONs that are used as T_2/T_2* contrast agents can also function as MPI tracers, however they may not be ideal for MPI performance.

SPIONs in MRI are most implemented as T_2 (or T_2*) contrast agents, rather than T_1 contrast agents. Despite them being the most effective T_2 MRI contrast agents to date, with excellent T_2 field-dependent relaxivities surpassing 100 m M^{-1} s^{-1},[108] they have several drawbacks. As a negative contrast agent in MRI, SPIONs create 'black holes', obscuring the underlying anatomical tissue structures.[12,99,109] Additionally, other endogenous sources of contrast may be mistaken for the exogenous SPIONs, such as haemorrhagic tissue or air-tissue interfaces (*i.e.*, in lung, skin surface, and bowel studies). As a result of this, and since they are not detected directly but instead indirectly, it is not possible to reliably quantify the concentration of SPIONs in targeted tissues.[12,99] This is in stark contrast to positively-contrasted MPI, which allows efficient quantitation.[24,46,47] There have been several studies demonstrating the potential for SPIONs in positively-contrasted T_1 MRI, yet research in this field remains uncommon.[110–119] In a recent paper, Thanh *et al.* synthesised monodisperse SPIONs, with sizes ≤5 nm, through application of a millifluidic multistage flow reactor.[120] These flow-synthesised SPIONs generated great values for enhancement of the T_1 contrast, with longitudinal relaxivities (r_1) greater than 10 mM^{-1} s^{-1}, and transversal relaxivities (r_2) reduced to just 20.5 mM^{-1} s^{-1}. On a final note, scanning and imaging in MPI is much more rapid and straightforward than in MRI, with no specialised training required to acquire or interpret the images.

3.3. Multi-modal imaging with MPI

A key disadvantage of modalities like MPI and nuclear medicine are that the images produced do not provide any anatomical information. They are only able to generate morphological information from contrasted structures. Therefore, to provide context about where the SPIONs have accumulated in the animal, MPI requires an anatomic reference. MRI and CT are examples of anatomical imaging modalities. They may provide complementary images of the structural information of a sample, with which an MPI signal can be referred against.

Dual modality MPI systems are currently being investigated, looking to combine the advantages of two techniques within one system, similar to how PET/MRI or PET/CT systems complement each other.[121–123] MPI is most frequently co-registered with MRI as it is possible to employ the same type of SPION for both techniques, and because both modalities utilise mag-

netic fields to generate their images. Typically, the imaging is performed in their respective devices and the information is combined *via* post-processing procedures to produce a 3D tomographic image of the sample.[124,125] The first *in vivo* studies for co-registered MRI/MPI images were conducted by Kaul *et al.*, in which measurements with preclinical 7 T MRI were performed before and after MPI scan.[124]

Recently there has been lots of work on the construction of hybrid MPI/MRI scanners to help ease the co-registration process.[122,123] High spatial registration accuracy can be achieved as MRI and MPI modalities share the same FOV. However, both modalities require very different magnetic field topologies, and the field strength required for MRI is so great that the SPION tracers become fully saturated. Consequently, simultaneous imaging is difficult to realise, and acquisition of data sequentially has been employed instead. The first instrument setup to combine both modalities within a single system was introduced by Franke *et al.* in 2013, wherein, all magnetic components are arranged concentrically and with an identical magnetic centre.[126] The subject can therefore be sequentially imaged with both modalities without the need for repositioning or transportation of the subject. From this initial magnet design, the first fully integrated pre-clinical MPI/MRI system for static 3D imaging was presented.[122,127] Successful initial phantom measurements were taken, demonstrating the feasibility of this system. The first *in vivo* results from this new methodology were gathered later by the same group, presenting a rapid, quantitative, and non-invasive *in situ* cardiovascular assessment of a beating rat's heart.[128] In this work, 3D anatomical information obtained through MRI is combined with 3D information on the *in situ* location of SPIONs from MPI, following a bolus tail vein injection. These results demonstrate the potential of this system for future clinical applications.

The benefits of imaging simultaneously rather than sequentially have been appreciated with other hybrid modalities such as PET/CT.[129–131] As established above; this mode of imaging is difficult to realise with MPI/MRI hybrids. However, Vogel *et al.* have developed a hybrid MPI/CT scanner that can indeed provide simultaneous data acquisitions.[132] The MPI component is based upon a unique concept for generating a static FFL, working through the integration of Halbach rings into a rotating gantry.[72] This offers an open design, providing a 'window' for direct feedthrough of X-rays and thus, CT imaging. As a result, the quantitative SPION distribution as well as the anatomical information of the surrounding tissue material can be visualised simultaneously and rapidly, providing a potential basis for improving diagnostic accuracy in pre-clinical imaging.[132]

4. Development of SPIONs as MPI tracers

4.1. Introduction to SPIONs

Signal detection and imaging quality in MPI is almost entirely dependent on the specific SPION tracer used.[53,133] This stems from direct detection of the non-linear magnetisation of

SPIONs by the system for signal generation, without any background interference from tissues or signal noise. Hence, for improved MPI performance, tailored tracers with specific properties are required. Generally, SPIONs used in MPI comprise a spherical crystalline core, typically of maghemite (Fe_2O_3) or magnetite (Fe_3O_4) crystals, which are colloidally stabilised using biocompatible magnetically neutral polymeric coatings like polyethylene glycol (PEG) or carboxydextran. These particles tend to have a hydrodynamic diameter between 50 and 100 nm.[134] At this size, iron oxide nanoparticles show superparamagnetic behaviour, with zero remanent magnetisation and coercivity following removal of the field, in the case of multi-core SPIONs or a system of single-core SPIONs.[135,136] This intrinsic property of SPIONs, together with the non-linear Langevin behavior detailed above,[80] allows for signal differentiation and detection of SPIONs in MPI.

The application of SPIONs as a tracing material is highly advantageous, not just in MPI, but in other SPION-compatible imaging modalities also. This was demonstrated in section 3.2, through a discussion of how MRI performance can be enhanced through implementation of SPION contrast agents. Generally, SPIONs are widely available, easy to handle, and relatively inexpensive compared to other commonly used tracers.[62] Furthermore, SPIONs are non-radioactive, and their signal does not decay over time. This enables effective longitudinal tracking studies of cell-based therapeutics.[26] Outside of MPI, SPIONs have been implemented in a wide variety of applications. They have shown promising clinical indication in iron supplementation therapy for anaemic candidates,[137,138] cell separation,[139,140] drug delivery,[141] hyperthermia,[142] mapping of lymph node metastases,[143,144] diagnosis of liver cancers,[145,146] and as a T_1 agent for angiographic MRI,[147] to name a few. There are several SPIONs that have either received approval from the USA Food & Drug Administration (FDA) for clinical applications or are in/close to a clinical trial.[148–153] A selection of these formulations, as well as some well-established pre-clinical SPIONs that could potentially serve as tracers in MPI, are presented in Table 2.

A particularly important feature of SPIONs, which is true of all nanomedicine, is that there is great modularity and flexibility possible when altering the structure and properties of the nanoparticle. This tunability is particularly valuable in MPI where the advantages of a particular SPION in a particular application is dependent on so many factors, including the size and shape of the iron oxide core, the type of surface coating, and whether there is any additional surface modification.[18,153,154] As a result, researchers can produce meticulously engineered tracers in MPI with different physical and biological properties specific for different applications (Fig. 3).

At the beginning of MPI exploration, SPION tracers that were designed as T_2^* or T_1-weighted MRI contrast agents were evaluated for their MPI performance.[134] However, since MRI and MPI have totally different physics, it was determined that these existing tracers were not ideal for reliable application in MPI and that new SPIONs would have to be tailored to MPI's unique set-up.[51,63,161]

Table 2 Well-documented examples of clinical or pre-clinical SPION formulations that have been used or may have potential as MPI tracers

Name	Company	Coating	Hydrodynamic diameter (nm)	Core diameter (nm)	Applications	Market status
Ferucarbotran:82 Resovist®/VivoTrax™ (USA, Japan, EU)[a]; Cliavist® (France)	Bayer AG (Resovist®/Cliavist®); Magnetic Insight (VivoTrax™)	Carboxydextran	62	Multi-core, ~4 each core	MRI contrast agent & MPI	Clinically approved (Resovist® in EU, Japan)
Ferumoxytol:155 Feraheme® (USA); Rienso® (EU)	AMAG Pharmaceuticals (Feraheme®); Takeda Pharma (Rienso®)	Carboxymethyl-dextran	30	3–4	Iron supplementation therapy & MRI angiography	Clinically approved (USA)
Feruglose:156 Clariscan™	GE Healthcare	PEGylated starch	20	5–7	MRI blood pool agent	Clinical trial
FeraSpin® XXL[157]	Miltenyi Biotec	Carboxydextran	65	Multi-core, 5–7 each core	MRI blood pool agent	Pre-clinical
LS-008[3]	LodeSpin Laboratories	PMAO[b]–PEG	80	25	MPI blood pool agent	Pre-clinical
Perimag®[158]	MicroMod	Dextran	130	Multi-core, ~5.5 each core	MRI contrast agent	Pre-clinical
PrecisionMRX®[159]	Imagion Biosystems	mPEG	41	24–25	MRI contrast agent & MPI	Pre-clinical
Synomag®-D[160]	MicroMod	Dextran	56	Multi-core, 5–15 each core	Hyperthermia & MPI	Pre-clinical

[a] Locations where commercially available. [b] Poly(maleic anhydride *alt*-1-octadecene).
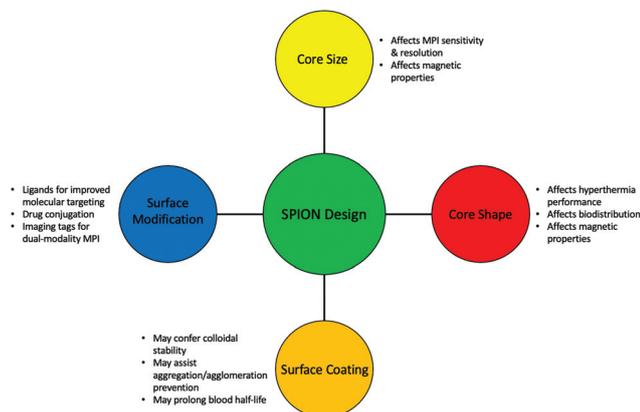

Fig. 3 Important structural modifications that could be considered when synthesising a SPION tailored for different MPI applications.

Multi-core SPIONs are far more common than their single-core counterparts.[5,157,162,163] Many of the frequently implemented commercial SPIONs have multi-core structures, as demonstrated in Table 2. It is, however, very complex to control the structural uniformity of clustered cores, as there are many structural variables that need to be considered, including, the number of cores per cluster, the cluster diameter, shape, density, and the inter-core distances and spatial distribution.[60] Any alteration in these parameters will lead to considerable changes in the packing arrangements, and this can significantly affect the dipole–dipole or exchange-interactions between the tightly associated cores, which strongly influence the magnetic behaviour of the SPIONs.[164–166] Because of this, in general, multi-core SPIONs have less uniform magnetic properties than standard single-core formulations, and produce poorer signals in MPI. Despite this, the presence of multiple cores can also be advantageous, if there is proper control of the structure during the synthesis.

Many recent studies on the synthesis of single-core SPIONs for MPI have been focussed on the effect of core size on MPI performance and sensitivity. One of the principal reasons for the poor performance of MRI-tailored SPIONs in MPI is the small size of their magnetic iron oxide cores (generally <10 nm), which results in lower magnetic moments for the nanoparticles.[53,167]

Both core structures hold equally important roles in MPI applications. Individually coated single-core SPIONs have demonstrated significantly increased blood half-lives *in vivo*,[168] favouring their use in perfusion imaging.[58,169,170] Additionally, the structural uniformity is beneficial for the targeted delivery of SPIONs to a therapeutic site, since core size is a major determinant of a SPIONs pharmacokinetic behaviour, and therefore its biodistribution.[171] On the other hand, multi-core SPIONs have also been implicated as greatly beneficial for many biomedical applications. The presence of the magnetic coupling interactions between the clustered cores is particularly advantageous in magnetic hyperthermia applications.[164] The improved magnetic moment renders advantages in standard magnetic fluid hyperthermia (MFH) techniques,[172–176] as well as MPI-coupled MFH.[177–180] The benefits of MPI–MFH is discussed in depth in section 5.2.2.

The shape of the core, or cores in the case of a multi-core formulation, is another factor that demonstrates strong influence over SPION performance in MPI. To date, most SPION cores developed for MPI, and its applications, have a spherical shape. However, it is known that non-spherical MNPs can offer significant advantages in many different biomedical applications, as a consequence of altered physical properties, and the potential for improved magnetic characteristics, including M_s, magnetic anisotropy,[181–183] and heating properties.[184,185] Additionally, as alternative MNP shapes present larger available surface areas for cell interactions, as compared with equivalently sized spherical nanoparticles, they often demonstrate greater cellular uptake.[186] As well as this, they have potential for enhanced blood circulation half-lives.[187]

In theory, the potential for improved magnetic properties, through the synthesis of non-spherical SPIONs, should be an effective way enhance MPI sensitivity and spatial resolution. As a result, such work has attracted the attention of various research groups. In particular, there has been sustained recent interest in the implementation of cubic SPIONs in MPI.[18,188] These nanocubes have a lower proportion of disordered spins at their surface and smaller surface anisotropies in comparison to equivalently sized spherical SPIONs.[189] This results in higher values for M_s and magnetic susceptibility, and consequently improved MPI performance, at certain sizes.[190] Along with this enhanced magnetic performance, the tendency of cubic SPIONs to spontaneously form chain-like arrangements has led to improvements in the performance of SPIONs in MPI–MFH.[13,190,191] A recent study from Avugadda *et al.* showcased the advantages of SPIONs, comprising a controlled number of cubic cores, on MPI, and potential MPI–MFH performance.[5] Among the variety of magnetic assemblies synthesised in this study (Fig. 4a), multi-core dimer and trimer structures exhibited the greatest MPI properties (Fig. 4b and c). The other structures investigated were larger multi-core clusters of nanocubes, and individual single-core nanocubes, all synthesised using the same polymer coating. The enhanced performance is attributed to the beneficial uniaxial magnetic dipolar coupling present in the chain-like smaller multi-core assemblies.[192]

Another key consideration in the design of SPIONs for MPI applications is the choice of biocompatible surface coating. As a general trend, a coating must confer colloidal stability to the particle, assisting aggregation prevention under various complex physiological environments, whilst also mediating any interactions with biological entities. This further stability can also potentially prolong half-life in the bloodstream, help prevent agglomeration during storage or application, and counteract possible oxidation.[107,193] It is also important to ensure the coatings promote cellular uptake yet preserve the optimal magnetic response of the SPIONs when dispersed in the acidic endosomal environment. There are many common choices of coating, each with their own advantages and functions depending on their molecular structure. Polymers are among the most popular coatings for SPIONs.[194,195] Early MPI research typically relied on multi-core ferucarbotran (Resovist,
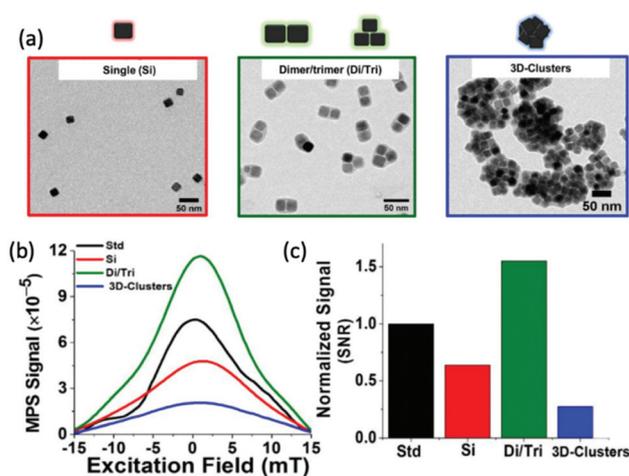

Fig. 4 Magnetic assemblies comprising a controlled number of cubic cores, designed for optimal MPI performance. (a) Transmission electron microscopy (TEM) images of the different SPION assemblies made from iron oxide nanocubes encapsulated in a poly(styrene-*co*-maleic anhydride) coating. The assemblies synthesised were single nanocubes (Si), short-chain dimers/trimers (Di/Tri), and various 3D-cluster configurations. (b) PSF demonstrating the MPI signal obtained for each synthesised sample, in comparison to that of the reference, VivoTrax (Std). (c) Histograms of the corresponding SNRs for each synthesised sample and the commercial reference. Reproduced from ref. 5 with permission from the Multidisciplinary Digital Publishing Institute. This is an open access article distributed under the terms of the CC BY License (https://creativecommons.org/licenses/by/4.0/). Copyright 2020, the authors. Article can be found at: https://www.mdpi.com/2079-4991/11/1/62/htm. No changes were made to the original figure.

Bayer AG), a SPION originally clinically approved as an MRI contrast agent in the liver. Ferucarbotran nanoparticles are coated by a carboxydextran polymer.[50] More recently, PEG and dextran polymer coatings have been employed most frequently. This is because they are not rapidly recognised by macrophages in the liver and spleen when administered intravenously and consequently have enhanced circulation time.[196,197] They have also been generally recognised as safe by the FDA.[107] The biodistribution of PEG- and carboxydextran-coated SPIONs was studied by Keselman *et al.*[198] While the carboxydextran-modified SPIONs are cleared rapidly to the liver, the PEG-coated particles are sustained for a relatively long blood half-life of 4.2 h before eventual excretion through the reticuloendothelial system (RES), illustrating the benefit of PEG-coated SPIONs for *in vivo* studies.

It is also worth noting that coatings can be altered to tailor their biochemical properties towards a specific physiological application. Examples of such alteration are that the coating may be grafted differently (*i.e.*, it can be chemisorbed, physisorbed, covalently bonded *etc.*), or that different graft densities and molecular weights of coating may be applied. Guzy *et al.* demonstrated the importance of polymer coating choice, and coating molecular weight, on SPIONs undergoing biodegradation.[81] SPIONs can undergo a variety of physicochemical changes as they degrade, which generally results in

detrimental effects on MPI signal properties and 'nanoparticle resolution'. It was found that larger polymers with a greater molecular weight will degrade more slowly in harsher endosomal conditions, such as at a tumor site, and thus their MPI signal will remain for longer.

The surface coating can also act as a structural support for additional surface modification, with the potential to conjugate a huge variety of possible functional molecules like drugs and ligands to improve molecular targeting, and proteins, antibodies, or aptamers for highly specific chemical interactions with complex biological systems. It can also provide a platform for imaging tags, specifically molecules that allow dual modality imaging with MPI, for example fluorophores for fluorescent microscopy.[4,199] Following successful surface-modification, the resulting SPIONs may be employed for MPI.

4.2. Synthetic methods

The modularity in SPION design in Section 4.1 is incredibly useful. To ensure production of SPIONs with desired properties, it is fundamentally important to choose the most appropriate method of synthesis. The choice has a strong influence on key physical characteristics of SPIONs such as crystal structure, core size, and size distribution, and consequently, on the magnetic properties of the nanoparticles. A comparison between five of the most employed synthetic methods are briefly summarised in Table 3, demonstrating their specific advantages and downsides. Besides those outlined in the table, SPIONs can be effectively prepared by various other techniques, including sonochemical and electrochemical deposition, microwave irradiation, laser pyrolysis, and reduction methods.[194,200–202]

Co-precipitation and thermal decomposition and are preferred for the synthesis of SPIONs for MPI.[203] Co-precipitation works by the simultaneous precipitation of Fe^{3+} and Fe^{2+} aqueous salts following addition of a basic solution.[204] It is a cost-effective and simple process, capable of high-yielding, scalable syntheses. Additionally, the synthesis does not require an organic solvent and the precursors used are generally environmentally friendly.[205] Despite these beneficial qualities, the nanoparticles formed are often relatively polydisperse with a

low degree of crystallinity.[206,207] This can result in an appreciably weakened MPI signal. Differently, SPIONs with a very narrow size distribution and excellent crystallinity can be prepared through thermal decomposition.[208,209] In this method, SPIONs are synthesised through the decomposition of organoiron precursors in organic solvents with high-boiling points, in the presence of stabilising surfactants. These surfactants bind to the growing nanocrystals, controlling their nucleation and growth. However, despite formation of high-quality samples, this technique requires expensive, and generally toxic reagents and solvents, and is therefore not environmentally friendly.[107] Furthermore, as a hydrophobic coating is formed on the surface of the SPIONs during synthesis, an additional surface modification step is required to obtain the biocompatible, water dispersible SPIONs to be used in biomedical applications. An in-depth description of all syntheses techniques is not within the scope of this review, thus, for further description of the other techniques, interested readers should refer to reviews by Thanh *et al.*[210,211]

4.3. Recent developments in SPION research

Similar to when SPION contrast agents were first realised for MRI in the 1980s,[212] research on the development and synthesis of monodispersed novel MPI-tailored SPIONs has recently become an important area of research.[5,63,188,213–216] These new particles can be functionalised and optimised for improved performance in specific applications, like for increased circulation time or for more efficient cell targeting. Whilst MPI-optimised tracers will have to undergo a lengthy evaluation before clinical approval, the exploration and development of better performing SPIONs should spur further work towards clinical applications.

The development of tracers with long circulation times is crucial for many applications. Typically, when nanoparticles are administered into bloodstream circulation, there is just a narrow time window to image the particles before they accumulate in the liver and spleen for excretion, where the concentration of the particles decreases such that MPI can no longer get a meaningful signal.[102] Studies on the circulation time of carboxydextran-coated multi-core ferucarbotran

Table 3 A summary of well-established synthetic methods for SPIONs. Adapted with permission of John Wiley & Sons, from ref. 220; permission conveyed through Copyright Clearance Center, Inc. Also adapted from ref. 207 with permission from Taylor & Francis. This is an open access article distributed under the terms of the CC BY License (https://creativecommons.org/licenses/by/4.0/). Copyright 2020, the authors. Article can be found at: https://www.tandfonline.com/doi/full/10.1088/1468-6996/16/2/023501

Synthetic method	Synthesis complexity	Reaction temperature (°C)	Reaction length	Solvent	Size distribution	Shape control	Yield
Co-precipitation	Very simple, ambient conditions	20–90	Minutes	Water	Relatively narrow	Poor	High, scalable
Thermal decomposition	Very complicated, inert atmosphere	100–320	Hours-days	Organic compound	Very narrow	Very good	High, scalable
Hydrothermal	Simple, high pressure	150–220	Hours-days	Water–ethanol	Relatively narrow	Very Good	Medium, scalable
Microemulsion	Complicated, ambient conditions	20–50	Hours	Organic compound	Relatively broad	Good	Low, not scalable
Sol–gel	Complicated, ambient conditions	25–200	Hours	Water–ethanol	Relatively broad	Good	Medium, scalable

(Resovist), which is generally considered the 'gold-standard' of MPI tracers, show that following administration to rabbits, the MPI signal decreased to ~12% of the initial intensity after just 15 min, and within 30 min, the signal had disappeared entirely.[217] Another commercially available tracer with potential use in MPI is dextran-coated Synomag-D (MicroMod), where the MPI performance shows better circulation times ($t_{1/2}$, ~1 h) as compared to Resovist.[20] Khandhar et al. developed a new single-core nanoparticle known as LS-008 (LodeSpin Lab) through a post-synthesis oxidation method.[218] This MPI-tailored tracer of core diameter, 25 nm, produced outstanding resolutions (1.6 mm at a 7 T m^{-1} μ_0^{-1} field gradient) and was designed for long blood circulation times ($t_{1/2}$, ~105 min in mice), with an exceptionally stable PMAO–PEG coating. However, for many of the potential applications of MPI, much longer half-lives are required.[3,58,92,169,170,219] Additionally, the availability of longer-circulating tracers will reduce the quantity of tracer required and/or the number of tracer administrations for treatment.

New MPI tracers with long blood circulation half-lives of 7 h were obtained by Liu et al., termed RL-1, as shown in Fig. 5a.[20] These single-core SPIONs were developed using a semi-batch thermal decomposition process with molecular oxygen addition. This was followed with an optimised PEG–silane ligand exchange process, producing SPIONs with high values for spatial resolution (~2 mm at 5.7 T m^{-1}) and sensitivities greater than multi-core Synomag-D, and ~3 times greater than multi-core ferucarbotran (Resovist) (Fig. 5b). Another long-circulating tracer was developed by Song et al.,[28] composed of a Janus iron oxide@semiconducting polymer nanostructure (Fig. 5c) synthesised through a nanoprecipitation method reported prior by the same group, shown in Fig. 5d, where the semiconducting polymers employed demonstrate great biocompatiblity.[12] These particles provide a nano-platform for ultrasensitive multi-modal imaging (MPI/MRI/photoacoustic/fluorescence, termed MMPF nanoparticles) of tumor xenografts in living mice, possessing exceptionally long-term blood circulation times ($t_{1/2}$, ~49 h) and consequently very high tumor uptake.[28] This half-life permits the tracer to be tracked and quantified in the mice longitudinally for up to 85 d (Fig. 5e).

An alternative approach to increasing circulation times includes entrapping the SPIONs into human red blood cells (RBCs).[221] Through nuclear magnetic resonance measurements, such loaded RBCs were demonstrated to circulate for over 12 d in mouse models before an obvious reduction in concentration could be detected.[222] For RBCs loaded with Resovist, transmission electron microscopy images show that the particles have a spatially uniform distribution within the cells, without any discernible indication of particle aggregation.[223] Utilising Resovist-loaded RBCs, Rahmer et al. presented the first evidence that SPION-loaded cells could be imaged in vivo with MPI, showing clear imaging of the blood pool in mice several hours following injection.[224] This observation was supported with magnetic particle spectroscopy (MPS) measurements, performed to determine the concen-
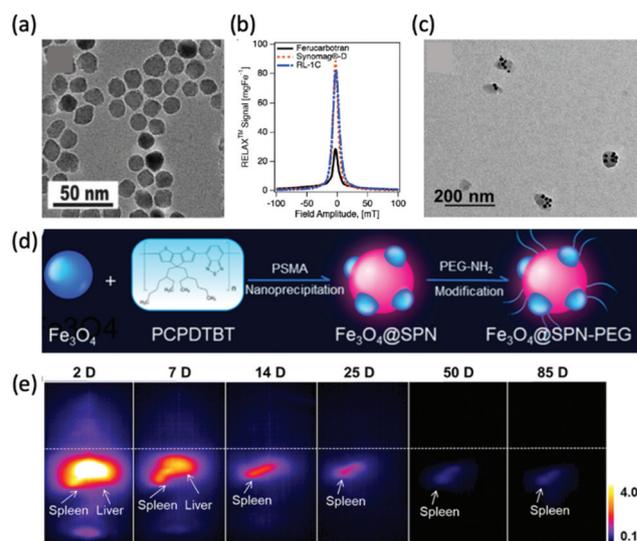

Fig. 5 MPI-tailored SPIONs, designed for long blood circulation half-lives. (a) TEM image of RL-1 SPIONs. (b) PSF demonstrating the MPI signal obtained for the RL-1 SPIONs, in comparison to that of the references, Synomag-D and ferucarbotran SPIONs. Reproduced from ref. 20 with permission from Ivyspring International Publisher. This is an open access article distributed under the terms of the CC BY License (https://creativecommons.org/licenses/by/4.0/). Copyright 2021, the authors. Article can be found at: https://www.ncbi.nlm.nih.gov/pmc/articles/PMC8040827/. No changes were made to the original figure. (c) TEM image of MMPF SPIONs. (d) Schematic demonstrating the synthetic preparation route of MMPF nanoparticles, where PCPDTBT is poly[2,6-(4,4-bis(2-ethylhexyl)-4H-cyclopenta[2,1-b;3,4-b']dithiophene)-alt-4,7 (2,1,3-benzothiadiazole)], and PSMA is poly[styrene-co-maleic anhydride]. (e) Longitudinal MPI images of mice injected with MMPF SPIONs, demonstrating effective imaging for up to 85 d. Reproduced with permission from ref. 28. Copyright 2019 American Chemical Society.

tration of iron in samples of blood extracted from the mice at different time points following injection. Antonelli et al. also performed a study encapsulating different commercially available SPIONs, Synomag-D and Perimag (MicroMod) into RBCs through hypotonic dialysis.[225] COOH-functionalised Perimag loaded RBCs proved to be viable cells, while the magnetic signal of the equivalently functionalised Synomag-D loaded cells dropped sharply. Therefore, just the Perimag-loaded RBCs have potential for MPI diagnostic applications, showing potential for longer blood retention times than the equivalent free nanoparticles. Successful application of MPI to the imaging of pathological diseases depends on the quantity of nanoparticles that accumulate at a diseased site relative to other sites. Hence, another important area for MPI-tailored tracer development is in the synthesis of nanoparticles with coatings functionalised towards the active targeting of specific pathophysiologies.[226]

One of the more prevalent functional targeting applications is the targeting of nanoparticles towards cancerous cells/tumors. Cancer is one of the global leading causes of death, accounting for almost 10 million deaths worldwide in 2020 alone.[227] Interest in its effective targeting is therefore necessary. Arami et al. conjugated the glioma-targeting glycoprotein,

lactoferrin, to the PMAO–PEG surface coatings of their optimised single-core MPI tracers with diameters of 25–27 nm.[4] Very high-resolution 3D tomographic multi-modal images (MPI/CT/X-ray) demonstrate an enhanced uptake of the functionalised SPIONs in brain cancer xenografts in mice (Fig. 6a and b). This is due to the fact that lactoferrin molecules can pass through the blood brain barrier (BBB) with ease, through a receptor-mediated transcytosis mechanism, for active targeting.[199] Another work in this field, by Tomitaka et al., investigated the functionalisation of gold-coated multi-core SPIONs of ~30 nm with transferrin (Fig. 6c).[30] Like lactoferrin, transferrin is a brain glioma targeting ligand, which has exhibited great specificity due to the high expression of transferrin receptors on the surface of brain glioma and capillary endothelial cells. They demonstrated a high functionalisation efficiency of 58% for the SPION with the targeting ligand, using the procedure in Fig. 6d, and these functionalised particles showed great biocompatibility also.

Another targeting application, which is receiving increased interest, is the targeting of active myeloperoxidase (MPO), a potential inflammatory marker of vulnerable atherosclerotic plaque. Tong et al. developed novel single-core multi-modal SPIONs, as termed 5HFeC nanoparticles conjugated with 5-hydroxytryptamine and a cyanine 7 N-hydroxysuccinimide ester, that can specifically target MPO and identify these high-risk plaques in vivo.[228] These 21 nm nanoprobes image the active MPO in an atherosclerosis mouse model with high sensitivity, thus enabling quantitative evaluation of the severity of inflammation and monitoring of the MPO activity.
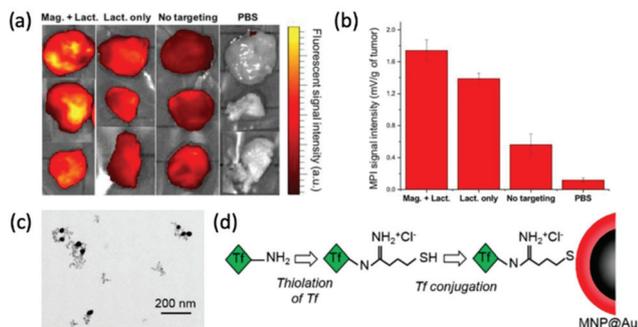

Fig. 6 MPI-tailored SPIONs, designed for efficient targeting towards cancerous cells/tumors. (a) Near infra-red fluorescent images and (b) MPI signal intensities of tumor xenografts excised from mice, under different conditions. 'Mag. + Lact.' corresponds to the injection of Cy5.5-lactoferrin conjugated SPIONs, using magnetic targeting, 'Lact. only' to the injection of conjugated SPIONs, without using magnetic targeting, 'No targeting' to the injection of non-conjugated Cy5.5-labelled SPIONs, and 'PBS', to the use of phosphate buffered solution, as a control. Reproduced with permission of the Royal Society of Chemistry, ref. 4; permission conveyed through Copyright Clearance Center, Inc. (c) TEM image of transferrin-conjugated SPIONs. (d) Schematic demonstrating the process for transferrin conjugation onto MNP@Au, where Tf is transferrin. Reproduced with permission of the Royal Society of Chemistry, from ref. 30; permission conveyed through Copyright Clearance Center, Inc.

4.4. Effect of SPIONs on spatial resolution and sensitivity in MPI

Traditionally, the most significant technical weakness of MPI is the relatively poor spatial resolution (typically ~1 mm).[134] To compete with preclinical CT and MRI, improving these resolutions to the submillimetre range would be an enabling advance. MPI spatial resolution can be defined as the ability to clearly distinguish two signals with the same intensity in space.[97] From a physical and radiologic viewpoint, this depends on two major factors. First is the magnetic gradient strength of the instrument, more specifically, the stronger the gradient, the narrower the FFR, allowing assignment of the generated SPION signal to a narrower space, and thus a greater spatial resolution.[55,56] The second factor comes from the physical and magnetic properties of the SPION utilised. This is based on effects to the FWHM of the PSF, where nanoparticles with narrower PSFs produce higher achievable resolutions. Along with a higher quality image, utilising a SPION with better spatial resolutions could significantly reduce instrument cost. A 10-fold improvement in resolution from MPI-tailored SPIONs could potentially reduce the cost of a clinical instrument by up to 100-fold, as spatial resolution can be exchanged for lower MPI gradients which would be required to be high in a clinical system.[229]

Sensitivity is another important parameter in determining overall MPI performance. A high sensitivity permits the detection of very small amounts of tracer,[26] and this is enabling for many biomedical applications, and is particularly important in cell tracking. It is characterised by the height of the Langevin curve at the transition point, where a taller curve indicates a higher sensitivity.[230] Consequently, a greater signal intensity in a PSF, also signifies a better sensitivity.[231] As with spatial resolution, progressing to the theoretical limits of MPI for sensitivity involves work on both the hardware and tracers.[44,232] In terms of instrumentation, advancements in sensitivity have most frequently been from developments in coil design.[37,74,78,79,233,234] Regarding tracer development for enhanced sensitivity, the signal intensity is governed by the physical and inherent magnetic properties of the tracer, as with spatial resolution, but is mostly dependent on the M_s.[16,18,55] Although the detection sensitivity of MPI is strong currently, through significant advancement it has the potential to become comparable with that of exceptionally sensitive nuclear imaging techniques.[233]

Given what has been discussed, the development of SPIONs with optimal sensitivity and spatial resolution performance has become a crucial part of MPI research. Sustained work in this area will enable high-performing, cost-effective, and safe MPI for humans. Tailoring of the structural parameters of SPIONs, such as their shape and crystallinity, can increase resolution and signal strength through enhancing of M_s.[18,51,52,183] One of the most important factors for improved performance is the size of the magnetic core. For single-core SPIONs, resolution and sensitivity increase cubically with core size, stemming primarily from higher M_s values.[235,236]

Unfortunately, Tay *et al.* demonstrated that the improvement in performance is limited with respect to size, as a result of increased Brownian relaxation blurring and a gradual shift from the superparamagnetic to ferromagnetic regime as sizes increase.[159] This has been described as the Langevin wall, and this phenomena reduces M_s, and as a result, hampers performance. An empirical ideal core size with respect to both resolution and sensitivity performance has been estimated at 24–28 nm for single-core SPIONs.[159,237] Gevaert *et al.* examined the MPI performance of several commercially available SPION tracers, confirming the resolution and sensitivity dependence of SPIONS to core size.[238]

Recently, a new strategy for tracer formation has been established based on strongly interacting particle–particle magnetic dipole interactions which subsequently form nanoparticle chains in fluid, on application of an external magnetic field (Fig. 7a).[239] This chaining was found to amplify the applied field 10-fold, resulting in very sharp PSFs. Through this method, Tay *et al.* demonstrated the potential of a 40-fold boost in sensitivity, and unprecedented 10-fold improvements in spatial resolution (Fig. 7b).[14,229] These properties theoretically allow the tracking of single cells *in vivo*. There have been several other studies testing the 'chaining hypothesis', specifically, examining the parameters that effect chain formation times. Colson *et al.* outlined that for optimised chain formation time, the conditions required are low media viscosities, as viscous solvents can block chain formation, and high nanoparticle concentrations, as the smaller the inter-particle separations, the easier it is for dipoles to interact.[240]

The formation of these 'chained' tracers has also been investigated and modelled computationally.[241] Zhao *et al.* employed simulations to evaluate the effect of the magnetic dipole–dipole interactions on the MPI performance and dynamic magnetisation of individual particles within the chain.[242] The results illustrate similar MPI signal intensity and resolution enhancements to those demonstrated by Tay *et al.*, for interacting chains of ≥2 particles.[14] They also suggest a large parameter space for design that can be used to tailor these chains towards optimised MPI performance, including, the number of particles in the chain and their separation distances, the composition of the SPIONs, and the viscosity of the solution.

Outside of novel 'chaining' approaches, there are other more established methods to improve spatial resolution and sensitivity through tracer synthesis, one of which is through the synthesis of SPIONs with improved monodispersity.[47,243] Monodisperse SPIONs with uniform magnetic domains have smaller FWHMs and higher values of M_s in the PSF, resulting in nanoparticles with higher spatial resolutions and signal intensities. Dadfar *et al.* describe a straightforward co-precipitation synthesis and following sequential centrifugation protocol to obtain monodisperse single-core particles of different sizes from a polydisperse SPION starting formulation.[244] Resulting from the narrow size distribution (polydispersity index (PDI) below 0.1), these optimised dispersions showed substantially improved M_s values, and thus performance in MPI, MRI and MFH, up to 7 times greater in comparison to the polydisperse starting formulation, as well as to commercially recognised SPIONs, such as Resovist. However, this is a two-step process and is not feasible for scale-up, nor is it environmentally friendly. In a different work, Unni *et al.* synthesised monodisperse SPIONs through a modified thermal decomposition process involving the controlled addition of molecular oxygen.[16] The particles synthesised in oxygen presence demonstrate greater magnetic properties (Fig. 8a), and exhibit a better MPI performance (Fig. 8b) than those in the absence of oxygen, with greater M_s values (74 Am² kg⁻¹ *vs.* 17 Am² kg⁻¹, respectively), and consequently improved values for FWHM (12.0 mT *vs.* 15.2 mT, respectively) and signal intensity (39.0 mL mg(Fe)⁻¹ *vs.* 13.1 mL mg(Fe)⁻¹, respectively). This improvement is attributed to appreciably more uniform magnetic and physical domain sizes, and fewer structural defects.

The choice of coating should also not be neglected when optimising SPIONs for higher image resolutions and sensitivities. In one study, Horvat *et al.* reported the positive impact of preparing SPIONs with cross-linked over non-crosslinked
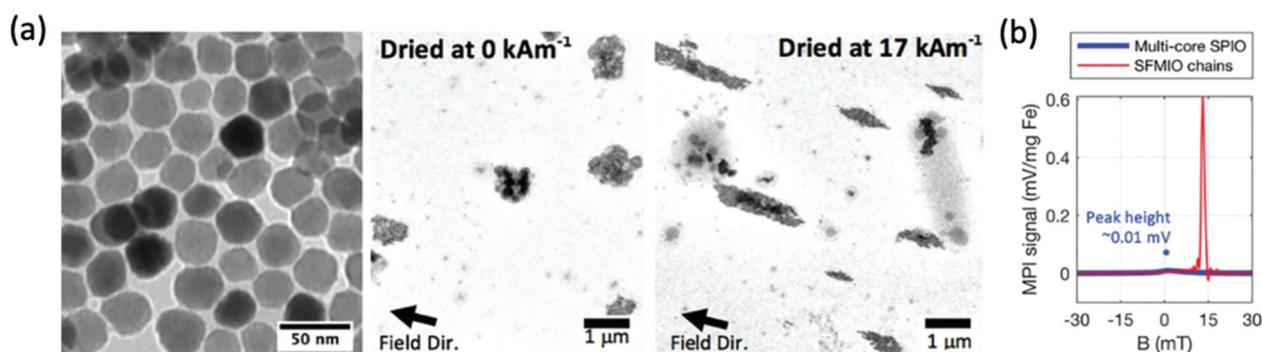

Fig. 7 Microscale linear chain structures, designed for optimal MPI spatial resolution and sensitivity. (a) TEM images showing clear formation of microscale chain structures following application of an external magnetic field. (b) PSF demonstrating order-of-magnitude taller and sharper signal peaks for the chains over standard multi-core ferucarbotran, where SFMIO is a superferromagnetic iron oxide chain. Reproduced from ref. 14 with permission from Wiley-VCH.
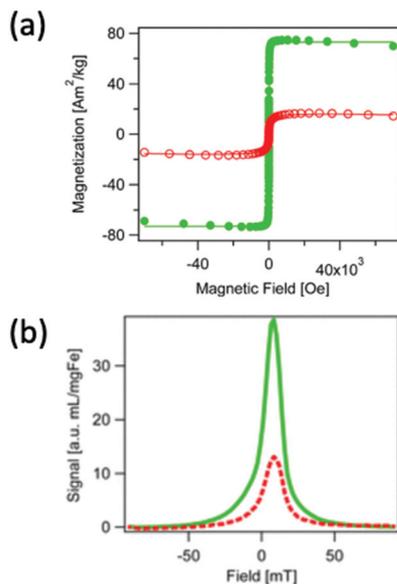
Fig. 8 SPIONs synthesised through a modified thermal decomposition reaction, in the presence and absence of molecular oxygen, designed for optimal MPI spatial resolution and sensitivity. (a) Hysteresis curves displaying the field-dependent magnetism of SPIONs synthesised in the presence of molecular oxygen (closed, green points), and absence (open, red circles). (b) PSF demonstrating the MPI signal for the SPIONs synthesised in the presence (full, green line), and absence (dashed, red line) of molecular oxygen. Reproduced with permission from ref. 16. Copyright 2017 American Chemical Society.

polymeric coatings on performance in MPI.[245] The cross-linked single-core SPIONs of average core size 18 nm, termed PF127DAPG, displayed a superior SNR, and consequently higher spatial resolution than their uncross-linked equivalents, PF127. Resulting from this, an iron quantity of 5.3 μg was required in PF127 SPIONs to produce the same spatial resolution values as 1.3 μg of iron in PF127DAPG SPIONs.

4.5. Development of alternatives to SPIONs as MPI tracers

Whilst almost all tracers designed for MPI have been based on iron oxide species, there has, in recent years, been evidence to suggest the potential of alternative MNPs to SPIONs for MPI, however research in this area remains underdeveloped. Theoretically, any MNP that is both highly biocompatible, and can display superparamagnetic behaviour with favourable M_s values, could potentially be employed as an effective MPI contrast agent.

Almost pure iron nanoparticles have generated exceptionally high values for M_s, up to 176 emu g^{-1}, at sizes of 13 nm.[246] However, as with many metal MNPs, they suffer from poor chemical stability and this has limited their application in imaging.[247] Such nanoparticles are rapidly oxidised to iron oxide following exposure to air, and therefore require stabilisation for application in MPI. Gloag *et al.* prepared superparamagnetic single-core nanoparticles with zero valent iron cores, coated with an iron oxide shell and a strongly binding brush co-polymer (Fig. 9a and b).[1] The iron oxide
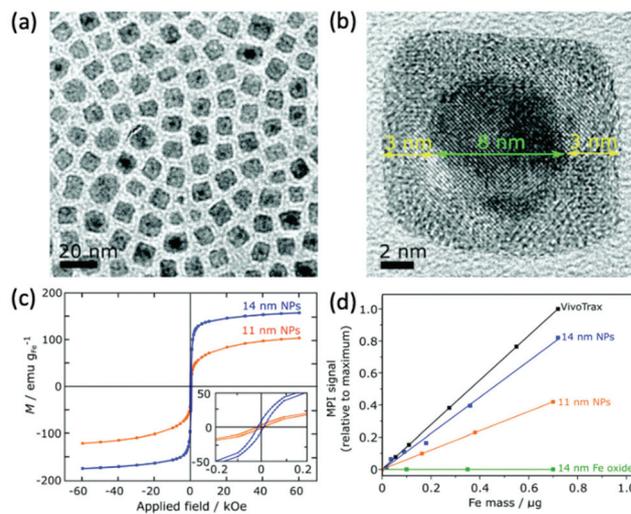

Fig. 9 Stable Fe(0) nanoparticles, designed for optimal MPI performance. (a) Low and (b) high resolution TEM (HRTEM) images of the cubic 14 nm nanoparticles. (c) Hysteresis curves displaying the field-dependent magnetism of 14 and 11 nm Fe(0) nanoparticles. (d) Plot of the MPI signal of the synthesised samples in comparison to that of the reference, VivoTrax, as a function of core mass. Reproduced from ref. 1 with permission from the Royal Society of Chemistry.

coating prevents the rapid oxidation of the metallic core, and the additional polymeric layer provides high colloidal stability, where the nanoparticles could remain water-dispersed for over 8 wk. These nanoparticles show an excellent M_s of 166 emu g^{-1}, at a size of 14 nm (Fig. 9c). At this size, the coated nanoparticles achieve an MPI signal intensity that is ~80% that of the much larger multi-core VivoTrax (Fig. 9d), whilst also having a very similar spatial resolution. In comparison, SPIONs of a similar size could not generate recognisable signals in MPI, due to their weak values for M_s. Strong MPI properties for tracers at this size is significant, opening the door to many potential MPI applications within cells and the brain, that were not possible with larger nanoparticles.

Metal alloy MNPs have also become of interest for MPI and its applications. FeCo alloyed nanoparticles in particular, demonstrate almost unmatched M_s values up to 215 emu g^{-1}.[248] On top of this, they exhibit superparamagnetic behaviour at sizes less than 20 nm, indicating their potential for MPI.[249] However, as with iron nanoparticles, they must be stabilised to prevent oxidation on exposure to air. In a recent study, Song *et al.* synthesised 10 nm FeCo nanoparticles (Fig. 10a) coated with a layer of graphitic carbon and PEG. These exhibit exceptional MPI signal intensities, 6.08 times higher than VivoTrax for equivalent molar core concentrations (Fig. 10b).[10] The graphitic carbon coating prevents rapid oxidation of the unstable FeCo core. Many more alloyed nanoparticles exhibit promising properties for MPI application, including FePt (M_s = 100 emu g^{-1}) and Fe$_5$C$_2$ (M_s = 125 emu g^{-1}) particles, but none, as of now, have been investigated for MPI.[181,250–252]

Ferrites of the M$_x$Fe$_{3-x}$O$_4$ general formula, display a spinel structure where M could theoretically be any divalent tran-
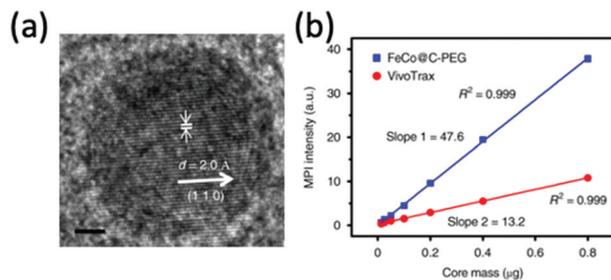
Fig. 10 Stable FeCo@C–PEG nanoparticles, designed for MPI and magnetic hyperthermia performance. (a) HRTEM image of the FeCo@C–PEG nanoparticles. (b) Plot of the MPI signal of the FeCo@C–PEG nanoparticles in comparison to that of the reference, VivoTrax, as a function of core mass. Reproduced with permission of Nature Research, from ref. 10; permission conveyed through Copyright Clearance Center, Inc.

sition metal ion. In the standard Fe_3O_4 SPION structure, M is Fe^{2+}. Doping of this structure with appropriate metal ions can improve the MPI performance of the particles by altering their magnetic properties.[54] Upon doping, the Fe^{2+} ion is substituted to a desired extent with the new divalent cation dopant (*e.g.*, Zn^{2+}, Co^{2+}, or Mn^{2+}). However, for potential use in biomedical applications, biocompatibility and toxicity of the ferrites is a concern.[253]

In one recent study, Silvestri *et al.* synthesised cubic ferrite nanoparticles with a tunable quantity of doped Co and Zn, which were then analysed for their MPI capability.[13] Firstly, they synthesised high quality Co-ferrite through a non-hydrolytic synthetic procedure (Fig. 11a). By altering the metal precursors used in this process, the cobalt ions could either be partially substituted with zinc ions, producing mixed Zn–Co-ferrite (Fig. 11b), or totally substituted, producing Zn-ferrite (Fig. 11c). All the cubes were synthesised within a similar size range below 15 nm. Among the different synthesised ferrites, the most impressive MPI properties were achieved with the superparamagnetic Zn-ferrite nanocubes, demonstrating the narrowest FWHM and greatest SNR (Fig. 11d and e). Notably, compared to VivoTrax, the Zn-ferrite nanocubes showed 3-fold higher values for SNR, whereas the Co-ferrite nanocubes exhibited almost zero signal in MPI. These results, combined with the fact that the Zn-ferrite composition is generally deemed more biocompatible than Co-ferrite, with much higher recommended daily intake quantities for Zn than Co,[254] indicate the potential of just the Zn-ferrites as effective MPI tracers. These impressive properties of Zn-ferrites in MPI have been echoed in other studies in the literature.[190,213,215]

Other ferrite nanoparticles that have been investigated for their MPI properties include Ni- and Mn-ferrites. Irfan *et al.* synthesised small Ni-ferrite nanoparticles (9–12 nm), functionalised with either a citric acid (CA) or polyacrylic acid (PAA) coating.[255] The MPI performance of the superparamagnetic $NiFe_2O_4$@CA and $NiFe_2O_4$@PAA nanoparticles was evaluated, both showcasing an improved FWHM over commercially available VivoTrax and Perimag SPIONs. In a different study, Du *et al.* designed monodisperse single-core Mn-ferrite nano-

particles, with the intention of producing a highly sensitive tracer with good multi-modal MRI/MPI performance and impressive MFH properties.[24] Along with both 8 nm, and 18 nm superparamagnetic Mn-ferrite nanoparticles, they also synthesised single-core SPIONs of equivalent sizes (Fig. 11f–i). Although the Mn-ferrite nanoparticles generally exhibit a greater M_s (Fig. 11j) and reduced magnetocrystalline anisotropies in comparison to SPIONs of equivalent core size, they demonstrate a poor MPI signal (Fig. 11k).

5. Primary biomedical applications of MPI

5.1. Cell tracking

One of the earliest applications in MPI was the systematic tracking of cells, as with MRI.[256–258] MPI benefits *in vivo* cell tracking in several ways. The most advantageous characteristics are the superior cellular sensitivity and contrast, and that it allows direct quantification of the SPION content and number of labelled cells at any depth.[8] These factors contribute to an *in vivo* cell detection limit down to ~200 labelled cells after implantation,[26] far surpassing the standard detection limits in MRI.[259] There has however been evidence to the capability of MRI to track single cells *in vivo*,[260–262] but as discussed in section 4.4, with advancements in the sensitivity of MPI scanners and tracers, the theoretical detection limit may also be just a single cell.[26] Nonetheless, the current properties of MPI permit efficient monitoring of the fate of cell-based therapies and diagnostics, as well as their biodistribution, clearance and retention. There are two primary cell-labelling techniques for cell tracking with MPI.[263] The first is *in situ* labelling, where SPIONs are administered intravenously, and phagocytic cells take up the nanoparticles *in situ* to deliver them to their target site (Fig. 12a). The second is *ex vivo* labelling, where the relevant cells are collected from the animal, with subsequent incubation/labelling with the nanoparticles *in vitro*, and injection back into the animal *in vivo* (Fig. 12b). Currently, many cells and cell-based therapeutics are tracked for biomedical applications, including cancer cells, stem cells for disease treatment, or immune cells for immunotherapeutic cancer treatment.

One of the most important advantages of SPIONs for this application is their biocompatibility. They have a favourable profile of toxicity, and *in vitro*, generally showing no, or very little short- or long-term effects on cell viability, differentiation or proliferation, in a range of cellular cultures.[264–267] This indicates the great potential for *in vivo* applications, especially cell tracking, and the clinical translation of MPI.[235] One study revealed that rodents can tolerate iron oxide concentrations of up to 3 mmol Fe kg^{-1}.[268] A further phase I clinical study on the commonly used SPION tracer, ferucarbotran (Resovist), demonstrated safe use of the tracer at doses of 5–40 μmol Fe kg^{-1}.[151] As a further point, SPIONs are completely biodegradable and will remain in the bloodstream until they are metabolised and finally excreted, just like endogenous iron, through the =RES.[102] Within this system they are primarily
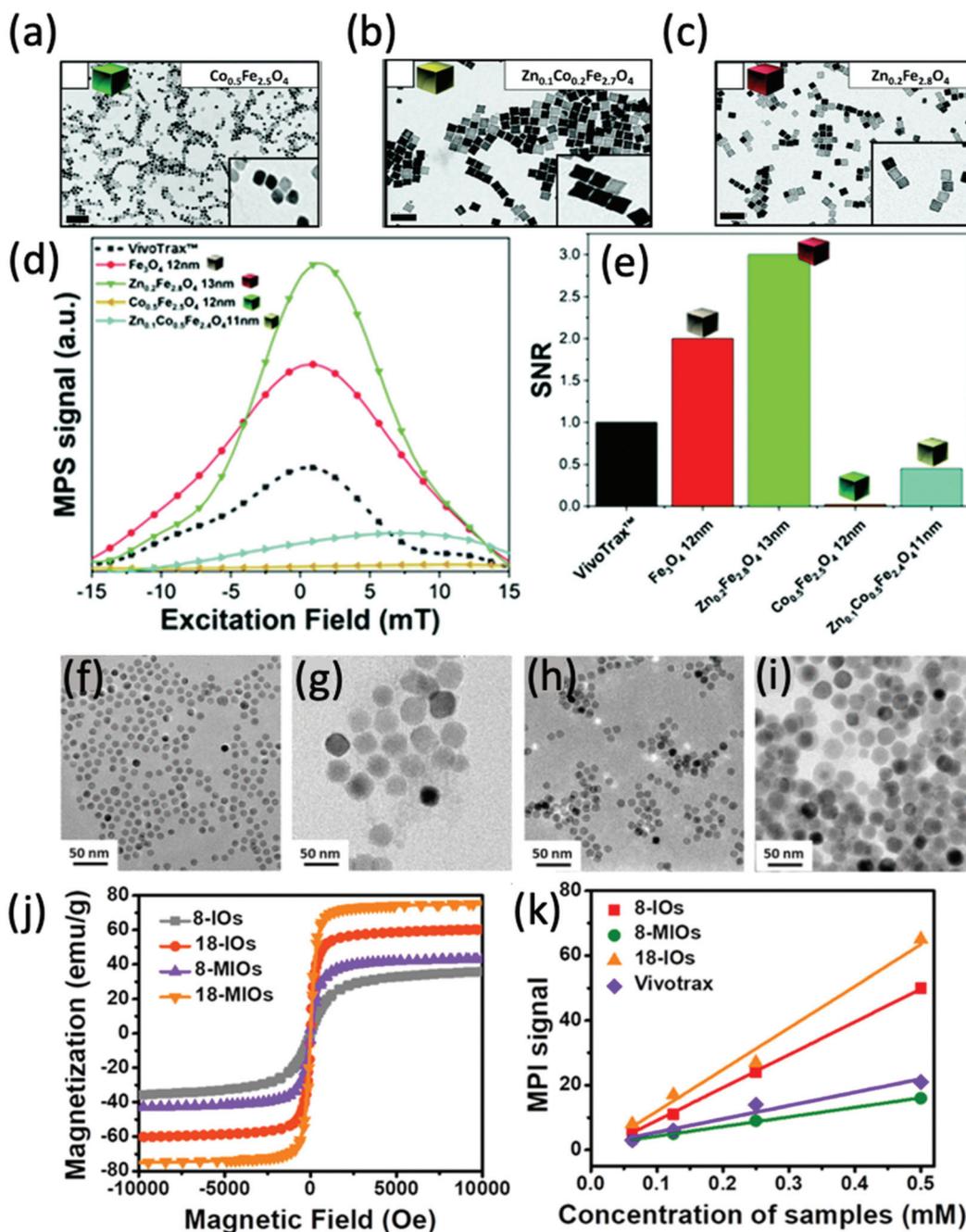
Fig. 11 Ferrite nanoparticles, designed for optimal MPI performance. TEM images of different ferrite nanocubes synthesised. The nanoparticles synthesised were (a) $Co_{0.5}Fe_{2.5}O_4$ nanocubes, (b) $Zn_{0.1}Co_{0.2}Fe_{2.7}O_4$ nanocubes, and (c) $Zn_{0.2}Fe_{2.8}O_4$ nanocubes. (d) PSF demonstrating the MPI signal obtained for each synthesised sample, in comparison to that of references, VivoTrax, and Fe_3O_4 SPIONs. (e) Histograms of the corresponding SNRs for each synthesised sample, the commercial reference, and Fe_3O_4 SPIONs. Reproduced with permission of the Royal Society of Chemistry, from ref. 13; permission conveyed through Copyright Clearance Center, Inc. TEM images of different SPIONs and Mn-ferrites (MIOs) synthesised. The nanoparticles synthesised were (f) 8 nm SPIONs, (g) 18 nm SPIONs, (h) 8 nm MIOs, and (i) 18 nm MIOs. (j) Hysteresis curves displaying the field-dependent magnetism of each synthesised nanoparticle. (k) Plot of the MPI signal of the SPIONs synthesised in comparison to that of reference, VivoTrax, as a function of sample concentration. Reproduced with permission from ref. 24. Copyright 2019 American Chemical Society.

cleared by the liver (80%), spleen (5–8%), and the bone marrow (1–2%).[269]

5.1.1. Cancer cell tracking. MPI has often been used as a cell tracking modality for immortalised cancer cell lines. Song

et al. produced MPI-tailored SPIONs that also possess a good fluorescence imaging performance (Fig. 13a and b).[12] These nanoparticles enabled efficient *ex vivo* cell labelling and were sensitive enough to longitudinally track as few as 250 pre-
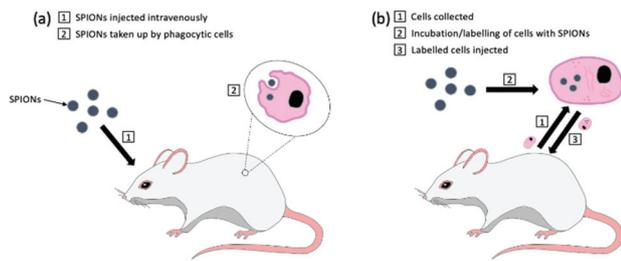
Fig. 12 The two primary cell-labelling techniques for cell tracking with MPI: (a) *in situ* labelling, (b) *ex vivo* labelling.

labelled immortal HeLa cells with MPI, following implantation in mice, as displayed in Fig. 13c. Importantly, the nanoparticles did not demonstrate any influence on the cell viabilities, even following a further 48 h of incubation. In another work, Melo *et al.* compared the quantitative MPI signals and tracking ability of micron-sized iron oxide particles (MPIOs) and 'gold-standard' VivoTrax (Magnetic Insight Inc.), for iron-labelled immortal cancer cell lines in a mouse brain.[29] MPIOs are different from SPIONs typically used for MPI. The particles consist of multiple small cores (~5–10 nm) embedded in a polystyrene matrix. Resulting from the clustered nature of the cores, they can be regarded as having one large superparamagnetic core (~0.9 μm), which contributes to a very large MPI signal (Fig. 13d). The results show that MPIO-labelled cells can be detected and quantified in the mouse brain model much more readily than VivoTrax-labelled cells (Fig. 13e–g), demonstrating the potential of MPIOs for MPI applications in cell tracking.[29]

Recently, there has been momentum towards studying patient-derived xenograft (PDX) models, supplanting tra-

ditional cell lines in cancer research as they better represent the tumor heterogeneity observed in the original tumor.[270] Studied results are, therefore, more clinically relevant. The ability to produce quality images and longitudinally track and study the fate of PDXs *in vivo* would be very valuable. Knier *et al.* demonstrated the first method for the efficient iron-labelling of PDX cells, which was also the first successful iron-labelling of breast cancer cells derived from patient brain metastases.[271] Utilising bioluminescence imaging (BLI) to evaluate cell viability, and MPI for detection and quantification of SPION content, they demonstrated sensitive longitudinal tracking of pre-labelled F2–7 PDX cells with MPIOs, where the signals indicate cell viability and tumor proliferation.

In another work developing imaging tools to target and label primary and metastatic lesions, Parkins *et al.* looked to exploit the tumor self-homing phenomenon.[272] This describes where circulating tumor cells (CTCs) that break away from the primary tumor into the blood stream, preferentially colonise established tumors rather than non-malignant tissues, accelerating metastatic disease. They demonstrate for the first time, the ability of MPI to sensitively detect systemically administered SPION-labelled CTCs and visualise self-homing. This was done in a murine model bearing pre-established human breast cancer lesions, and the labelling demonstrated no detrimental effects on cell viability. The results provide invaluable information about off-target tumor accumulation, as well as the efficiency of CTC infiltration, proliferation, and survival inside tumors, and the potential mechanisms driving self-homing within the body.

5.1.2. Immune cell tracking. A tumour does not just consist of cancerous cells; immune cells (*e.g.*, leukocytes), together with fibroblasts and endothelial cells, form the tumor
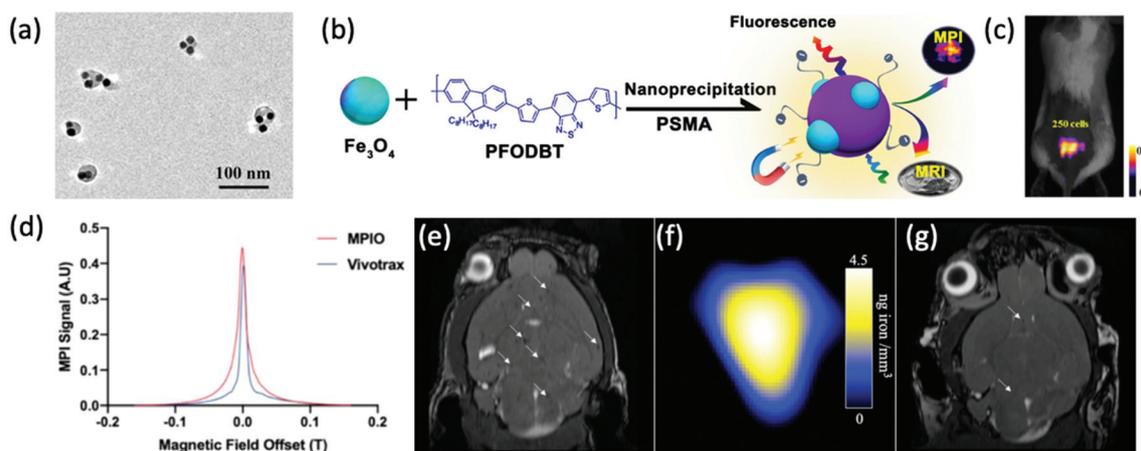

Fig. 13 The application of SPIONs in cancerous cell tracking with MPI. (a) TEM image of Fe_3O_4@PFODBT–COOH Janus nanoparticles, where PFODBT is poly[2,7-(9,9-dioctylfluorene)-*alt*-4,7-bis (thiophen-2-yl)benzo-2,1,3-thiadiazole]. (b) Schematic demonstrating the synthetic preparation route of Fe_3O_4@PFODBT–COOH Janus nanoparticles. (c) Overlay of a 2D projection MPI and white light image of a mouse implanted with 250 nanoparticle-labelled cells, following background subtraction. Reproduced with permission from ref. 12. Copyright 2018 American Chemical Society. (d) PSF demonstrating the MPI signal obtained for MPIO, in comparison to that of the reference, VivoTrax. The (e) MRI, and (f) MPI of a mouse brain injected with 5×10^4 4T1BR5 cells labelled with VivoTrax. The (g) MRI, of a mouse brain injected with 5×10^4 4T1BR5 cells labelled with MPIO. There was no MPI signal detected in the mouse brains injected with 5×10^4 4T1BR5 cells labelled with VivoTrax. Reproduced with permission from ref. 29. Copyright 2020 the authors.
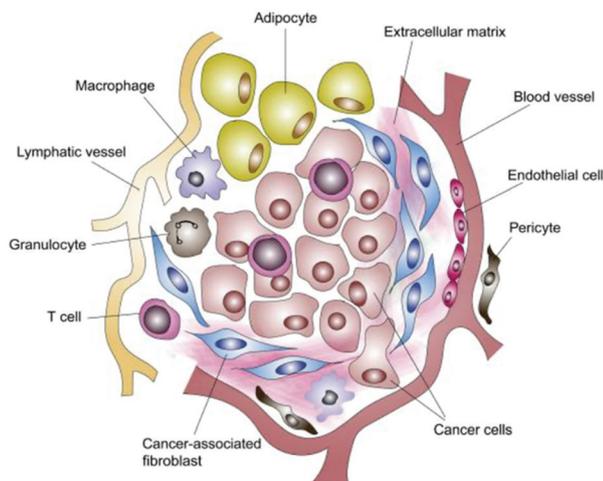
Fig. 14 Schematic representation of the TME. Reproduced from ref. 6, with permission from Elsevier.

microenvironment (TME, Fig. 14).[273] These immune cells interact with tumor cells to influence and modulate the size progression of the tumor. The rapid success and growth of research in cancer immunotherapy has stimulated the need for a method to help determine the location and behavior of immune cells in the TME systematically over time, and to evaluate the efficacy of immunotherapies. Traditionally SPION/^{1}H MRI, or ^{19}F MRI cell tracking techniques are used.[274,275] However, these methodologies are considered inadequate. MPI addresses many of the cell tracking needs for immunology and can track SPION-tagged immune cells *in vivo* for the lifetime of the labelled cell.[26]

The most abundant immune cell type in the TME are tumor-associated macrophages (TAMs). The presence of TAMs has been correlated with many protumoral effects, therefore enhancing and contributing to cancer progression.[276] Due to their role, they can act as a biomarker to quantifiably monitor both cancer detection and prognosis through imaging. In addition to aiding therapeutic development, the ability to label and image TAMs effectively through SPION phagocytosis will assist in the understanding of their recruitment and infiltration in tumors and could be utilised to predict how aggressive a tumor may be.[277]

Previous studies have utilised cellular MRI to indirectly image the spatial distribution of TAMs, through *in situ* SPION uptake.[278,279] More recently, Makela *et al.* demonstrated the first use of MPI in the tracking and detection of SPION-labelled TAMs *in vivo*, which are intravenously injected in a murine model of a 4T1 breast cancer tumor.[277] The images provide quantitative information on the *in vivo* iron labelling of TAMs for macrophage migration and their association with tumors, showcasing the advantages over equivalent MRI scans. Gerosa *et al.* also demonstrated MPI imaging of *in situ* labelled TAMs, where the MPI tumor signal could be detected at doses of just 3 mg kg^{-1} of Synomag-D.[280] Mansfield *et al.* built on these works by investigating the applicability of MPI to non-

invasively track TAMs in response to a CD47 mAb immunotherapy treatment.[281] CD47 is a cell surface glycoprotein often overexpressed by cancer cells that prevents the immune system from recognising the cancer.[282] Administration of the antibody during treatment blocks CD47, therefore modulating the phagocytosis of macrophages in cancer, and potentially triggering elimination of the cancerous cells. MPI images were acquired 1, 3, and 7 d after tracer injection.[281] The increase in MPI signal at the tumor site over this time, in comparison to an untreated control tumor, implies a higher accumulation of TAMs, therefore indicating increased phagocytosis and treatment success.

There is accelerated interest in tracking adoptive T cell cancer immunotherapies with MPI. Adoptive cellular therapy (ACT) is an effective strategy to boost the immune response against many cancers, but faces challenges treating solid tumors and invasive central nervous system malignancies like malignant gliomas.[283] An important step in the success of ACT is achieving efficient trafficking and persistence of T cells in solid tumors. Rivera-Rodriguez *et al.* demonstrate the first application of MPI to track ferucarbotran-labelled T cells *in vivo*, where the labelling did not affect T cell viability, phenotype, or cytotoxic function.[283] The labelled T cells were intraventricularly administered in a mouse model of invasive brain cancer, and their biodistribution and localisation over time was monitored successfully, despite a low uptake of nanoparticles by T cells observed (~1 pg Fe per cell). The non-invasive quantitative tracking of adoptively transferred T cell biodistributions will assist in the development of new and effective ACT strategies.

5.1.3. Imaging localised inflammation. A tumour does not just consist of cancerous cells; immune inflammation is a key process in the body's response to harmful stimuli, including damaged cells and irritants. Hence, the detection and monitoring of localised inflammation could help with the diagnosis of many pathological conditions and the assessment of treatment outcomes following therapeutic intervention. It is characterised by vasodilation, the accumulation of fluid, and the extravasation of immune cells to the inflamed site. Unfortunately, tracking inflammatory processes has traditionally involved low specificity imaging techniques or invasive methods like biopsies.[62] Previous MRI studies have already shown the benefits of SPION tracers for inflammation detection and tracking.[284,285] With MPI, inflammation can be more specifically detected, with a higher sensitivity.[228] Similar to generic cell tracking, there are two primary methods to monitor inflammation with SPIONs.[17] Either the nanoparticles are loaded directly into phagocytotic immune cells like macrophages *ex vivo*, with subsequent injection, or they are directly injected, to be engulfed by the cells *in situ*. Once tagged, these specific cells can be tracked as they migrate and accumulate within regions of localised inflammation.

In a recent example, Mangarova *et al.* implemented MPI in the *ex vivo* monitoring of vascular inflammation in abdominal aortic aneurysms (AAAs).[286] AAAs are defined by a weakening and dilatation in the abdominal aorta, usually in the infrarenal

portion of the artery, and are currently one of the leading causes of death in developed countries. In this study, the inflammatory response in the aneurysmal wall of an Angiotensin II-infused ApoE −/− mouse model was assessed with *in vivo* MRI, *ex vivo* MPI and *ex vivo* MPS.[286] The *ex vivo* MPI was performed 24 h post-intravenous administration of ferucarbotran (Resovist), following 3–4 wk of Angiotensin II perfusion. The results reveal abundant iron concentration within AAAs following their uptake by macrophages, demonstrating the feasibility of sensitive *ex vivo* MPI for the detection of vascular inflammation in AAA. These measurements correlated strongly with the results of *ex vivo* MPS, confirming the inflammatory activity and resulting SPION accumulation in the aneurysmal wall.

The non-invasive tracking of white blood cell (WBC) distributions can also be utilised in the monitoring and diagnosis of inflammation. Traditionally, tracking has been performed using WBCs directly labelled with radionuclides for scintigraphy or SPECT.[17] However, this is not ideal for general screening due to the extensive costs, tracer radioactivity, and high dosage of tracer required. In a very recent work, Chandrasekharan *et al.* explored for the first time, MPI, for the sensitive and radiation-free tracking of WBCs to sites of inflammation and infection.[17] For this, they used the commercially available antibody-conjugated multi-core anti-Ly6G SPION (Miltenyi Biotec GmBH, Fig. 15a) for *in situ* labelling and tracking, which is specific to the Ly6G antigen expressed on neutrophils. Prior to *in vivo* experiments, the MPI capabilities of this SPION were determined, with anti-Ly6G demonstrating improved values for MPI spatial resolution (1.26 mm *vs.* 1.49 mm, respectively) and sensitivity (~1.8 times greater) over multi-core VivoTrax (Fig. 15b and c). The *in vivo* studies were performed in a murine model of lipopolysaccharide-induced myositis, and the nanoparticles were intravenously injected following inflammation induction. MPI was used to image the biodistribution and demonstrated highly sensitive targeting and detection of inflammation at the sites of myositis, with strong contrast-to-noise ratios between 8 and 13 (Fig. 15d).

5.1.4. Stem cell tracking. Stem cell therapies are increasingly recognised as the future of regenerative medicine, demonstrating tissue regeneration potential for a wide variety of conditions.[287] However, for progression of this rapidly growing field to clinical translation, several concerns need to be addressed, most importantly is the poorly understood biological fate and migration of injected or implanted stem cells in the body. Successful therapy requires verification that the stem cells reach and remain at their intended target destination, maintaining viability to ultimately reform functional organs or tissues. It is therefore particularly relevant to monitor and track stem cell biodistribution following administration *in vivo*, as this would provide valuable information for predicting therapeutic efficacy, evaluating potential risk, and optimising treatment outcomes.[288] Standard preclinical imaging modalities have been used for *in vivo* stem cell tracking, including MRI,[94,289,290] US,[291] and radionuclide
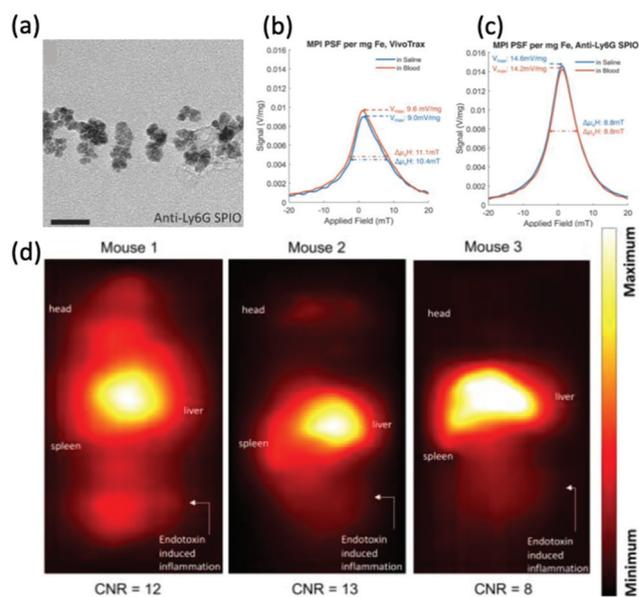

Fig. 15 The application of anti-Ly6G SPIONs in the imaging of localised inflammation with MPI. (a) TEM image of the anti-Ly6G SPIONs. PSFs demonstrating the MPI signal in saline, and blood, obtained for (b) anti-Ly6G SPIONs, in comparison to that of the reference, (c) VivoTrax. (d) Inflammation MPI images in three different mouse subjects undergoing myositis, with administered anti-Ly6G–SPIONs. Reproduced from ref. 17 with permission from Ivyspring International Publisher. This is an open access article distributed under the terms of the CC BY License (https://creativecommons.org/licenses/by/4.0/). Copyright 2021, the authors. Article can be found at: https://www.ncbi.nlm.nih.gov/pmc/articles/PMC7893534/. No changes were made to the original figure.

imaging.[292] MPI offers significant advantages for longitudinal stem cell tracking over other techniques, which has led to an extensive recent publication history.[293,294] It has been demonstrated that rat and human adult stem cells uptake SPION tracers, and that they localise within the cytoplasm.[295]

Mesenchymal stem cells (MSCs), which are found in many types of tissue and are multipotent, have shown particularly promising therapeutic results, where MSC-based therapies have shown success in treating many diseases, like stroke, myocardial infarction, and cancer.[296] Importantly, previous MRI studies displayed no decrease in cell viability, proliferation, or differentiation of MSCs after SPION-labelling.[297] However, targeted MSC delivery remains a challenge. Commonly, intravenous deliveries of MSCs become entrapped in lung microvasculature instead of the target tissue.[298] Zheng *et al.* sought to better understand this observation as they demonstrated, for the first time, the dynamic tracking of MSC administrations *in vivo* in a rat model with MPI, employing Resovist to label MSCs.[296] The labelled cells were intravenously administered, and the transplantation, dynamic biodistribution, and clearance, were monitored over a 12 d period. A 3-(4,5-dimethylthiazol-2-yl)-2,5-diphenyltetrazolium bromide (MTT) viability assay was carried out, and there was no considerable difference in the cell viabilities of unlabelled and labelled hMSC populations. The MPI images, co-registered

with CT, confirm that labelled MSC injections become immediately entrapped in lung tissue and are mostly cleared to the liver within one day. Most significantly though, these results demonstrate that MPI can longitudinally track intravenously administered MSCs safely and quantitatively.

In a different work, Nejadnik et al. utilised dual MPI/MRI to track the status of an implanted MSC scaffold over 14 d.[11] The MSCs were labelled with very small FDA-approved ferumoxytol (Feraheme, AMAG Pharmaceuticals) and ferucarbotran (VivoTrax) SPIONs. These labelled MSCs were successfully quantified with MPI at day 1 and 14 (Fig. 16a), with results indicating that MPI was sensitive to changes in cell number of labelled cells at the transplant site over time, with a significant decrease in SPION content observed at the later timepoints (Fig. 16b). Similarly, Sehl et al. implemented a trimodal imaging approach, utilising iron-based ^{1}H MRI, and quantitative MPI and ^{19}F MRI, to monitor the fate of transplanted ferumoxytol-labelled MSCs and the ensuing inflammation, which is inferred through the tracking of infiltrating macrophages at the transplanted sites in vivo.[19] This is the first time these three modalities have been combined to monitor cell populations in vivo. Significantly, the viability of these cells was unchanged following MSC labelling, where a 97% viability was

determined pre- and post-labelling. These labelled cells were implanted within the hind limb muscle of C57Bl/6 mice. A perfluorocarbon agent was also administered intravenously for uptake by phagocytic macrophages in situ. The labelled MSCs were detected using ^{1}H MRI and MPI, and perfluorocarbon-labelled macrophages were detected using ^{19}F MRI. The MPI signal decreased over a 12 d period, which is consistent with the death and clearance of the MSCs, whereas ^{19}F signal persisted (Fig. 16c), suggesting the continuous infiltration of perfluorocarbon-labelled macrophages, and thus inflammation.

In addition to using established SPIONs in the MPI tracking of labelled MSCs,[299] several groups have synthesised their own optimised tracers. Lemaster et al. synthesised hybrid poly (lactide-co-glycolide acid) (PLGA)-based iron oxide nanobubbles (Fig. 17a), labelled with a fluorophore, that show potential as a trimodal imaging tracer (MPI/photoacoustic/US) for MSC labelling.[8] The PLGA coating facilitates the US signal, the iron oxide core enables the MPI signal, and the fluorophore (DiR, 1,1′-dioctadecyl-3,3,3′,3′-tetramethylindotricarbocyanine iodide) increases the photoacoustic signal (Fig. 17b). They confirmed that there were no adverse effects on cell treatment with nanobubbles in vitro, and hence the nanobubble-labelled cells were injected intramyocardially into live mice for real-time imaging. This multi-modal tracer was shown to track MSCs effectively. In another study, Wang et al. designed a series of specialised cubic tracers with differing edge lengths.[18] The tracer with the most beneficial properties for MPI has an edge length of 22 nm, termed CIONs-22 (Fig. 17c). In comparison to the other synthesised tracers of differing sizes, CIONs-22 exhibit good M_s values (Fig. 17d) and high resolution and sensitivity (~2500 cells) for MPI, (Fig. 17e). With their efficient cellular uptake and labelling, these particles enable the long-term and real-time tracking of bone MSCs in vivo for MPI, exhibiting accurate tracking of their migration and distribution pattern once transplanted to hind-limb ischemia mice.

MPI has also demonstrated promise in the monitoring of neural progenitor cell (NPC) and neural stem cell grafts. Progenitor cells are descendants of stem cells that further differentiate to create specialised cell types. NPCs have been implicated in the treatment of several serious neurodegenerative disorders, such as brain ischemia, epilepsy, and Parkinson's and Alzheimer's disease.[48,107] The high sensitivity in MPI could facilitate the quantification of dynamic events, such as graft movement, in such brain disease models. In an important in vivo study, Zheng et al. implanted SPION-labelled NPCs into the forebrain of rats with forebrain ischemia and monitored the in vivo fate of the implanted cells longitudinally with MPI.[26] First, the NPCs were differentiated from human embryonic stem cells and labelled with ferucarbotran (Resovist). Following injection, it was demonstrated that the labelled cell grafts could be sensitively and quantitatively detected, and that the particles measured nonsignificant signal decay over a period of 87 d (Fig. 18a and b). The authors also demonstrated a detection sensitivity of 200 cells in their custom-built machine. This study therefore exemplifies the
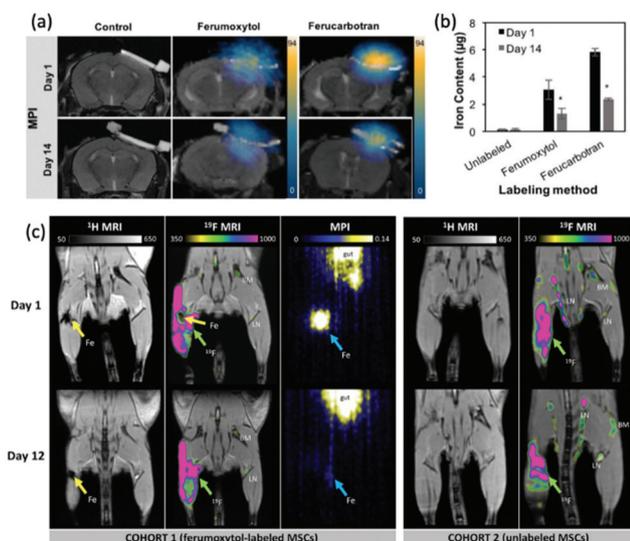

Fig. 16 The in vivo tracking of MSCs with MPI. (a) In vivo MPI images at days 1 and 14 following the implantation of ferumoxytol- or ferucarbotran-labelled therapeutic MSCs, and unlabelled MSCs as a control, in calvarial defects of experimental mouse subjects. (b) Iron content in the calvarial defects at days 1 and 14 following implantation of the differently labelled MSCs, as calculated from the MPI signals. Reproduced with permission of Springer Nature, from ref. 11; permission conveyed through Copyright Clearance Center, Inc. (c) In vivo ^{1}H/^{19}F MRI and MPI images at days 1 and 12 following the implantation of ferumoxytol-labelled therapeutic MSCs, and unlabelled MSCs as a control, in experimental mouse subjects. Reproduced from ref. 19 with permission from the Multidisciplinary Digital Publishing Institute. This is an open access article distributed under the terms of the CC BY-NC-ND License (https://creativecommons.org/licenses/by-nc-nd/4.0/). Copyright 2019, the authors. Article can be found at: https://www.ncbi.nlm.nih.gov/pmc/articles/PMC6935990/. No changes were made to the original figure.
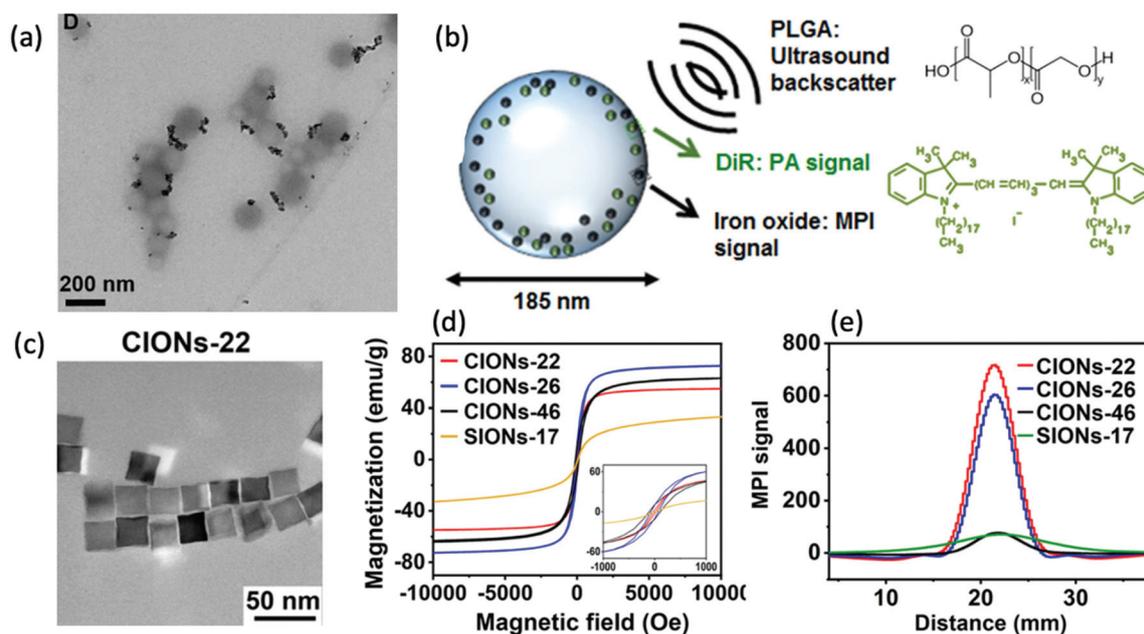
Fig. 17 MPI-tailored nanostructures, designed for the tracking of MSCs. (a) TEM image of PLGA-based iron oxide nanobubbles. (b) Schematic of the nanobubbles demonstrating which structural elements generate the different trackable signals. Reproduced with permission from ref. 8. Copyright 2018 American Chemical Society. (c) TEM image of 22 nm cubic CIONs-22 nanoparticles. (d) Hysteresis curves displaying the field-dependent magnetism of each synthesised nanoparticle, where CIONs refers to cubic iron oxide nanoparticles, and SIONs refers to spherical iron oxide nanoparticles. The number following, refers to the edge length. (e) PSF demonstrating the MPI signal obtained for each synthesised sample. Reproduced with permission from ref. 18. Copyright 2018 American Chemical Society.
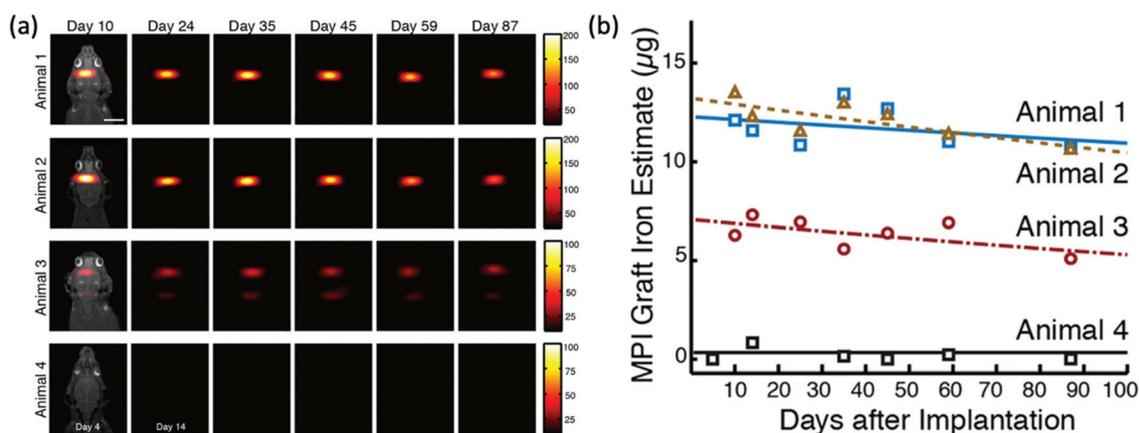

Fig. 18 The *in vivo* tracking of NPCs with MPI. (a) *In vivo* MPI images at days 1 and 14 following the implantation of 5×10^5 ferucarbotran-labelled NPCs in the forebrain cortex (animals 1–2), near lateral ventricle (animal 3), and with ferucarbotran only, in the forebrain cortex as control (animal 4). (b) Total iron estimation from MPI for the *in vivo* cell grafts, as a function of time. Reproduced from ref. 26 with permission from Springer Nature. This is an open access article distributed under the terms of the CC BY License (https://creativecommons.org/licenses/by/4.0/). Copyright 2015, the authors. Article can be found at: https://www.nature.com/articles/srep14055. No changes were made to the original figure.

feasibility and advantages of long-term sensitive tracking of NPC and stem cell transplants with MPI.

Transplantation of stem cell-derived islet organoids is a promising approach for the treatment of type 1 diabetes.[300,301] However, there has traditionally been no appropriate imaging technique for the accurate monitoring of graft outcomes after transplantation. Wang *et al.* demonstrated the use of MPI in

monitoring transplanted islets in animal models for the first time.[302] Pancreatic islets were isolated and labelled with VivoTrax SPIONs before transplantation either under the kidney capsule or in the liver of NOD/scid mice. MPI successfully images and quantifies the islets in these models, postmortem, at days 1 and 14 following transplantation. At the World Molecular Imaging Congress in 2020, Sun described the

feasibility of *in vivo* tracking of transplanted stem cell-derived islet organoids using MPI.[303] Human induced pluripotent stem cells were differentiated to islet organoids, which were subsequently labelled with VivoTrax following 21 d of differentiation. The labelled organoids were then similarly transplanted into the left kidney capsule of NOD/scid mice, which were examined by MPI/CT up to 28 d post transplantation. There is a strong signal initially detected in the kidney, but the intensity decreases over the study, which is to be expected with organoid clearance. Additionally, they performed an artificial intelligence analysis of the MPI images, to assist with total iron value prediction of the transplanted cells on different days, using an accurate machine learning algorithm established by the same team of researchers.[304] MPI, assisted by this machine learning algorithm analysis, was shown to accurately monitor islet organoids labelled with SPIONs post transplantation and provide quantitative information on their presence *in vivo*. These results demonstrate the potential for future imaging of cell transplantation and therapy for type 1 diabetes.

5.2. Theranostics

Theranostics, from a clinical and translational viewpoint, refers to an intimate combination of therapeutic and diagnostic interventions. MPI may open unprecedented opportunities for exploring new nanoparticle-based theranostic applications, stemming from the imaging and therapeutic capabilities of SPIONs and the intrinsic properties of MPI itself. In these approaches, diagnostic interventions are most used in combination with targeted MFH or magnetic drug delivery.

5.2.1. Drug delivery. Non-invasive *in vivo* drug release monitoring approaches are highly advantageous. MPI is particularly useful because of the linear quantitation and lack of background signal, providing spatial information which allows the accurate monitoring of therapeutic agent delivery.[305] This information illustrates the quantity of drug delivered to the target site, as well as the drug dosage distribution within the body. The ability to track drug delivery also allows for real-time adjustment of ensuing doses, ensuring that the dosage at the target site remains within the patient's therapeutic window (Fig. 19), and that there are subcritical drug concentrations at off-target sites within the patient (*e.g.*, organs).[15] The therapeutic window is the dosage range in which the highest therapeutic benefit can be achieved. At suboptimal levels, low non-lethal levels of drug can lead to resistance, where the drug will become less efficient and eventually ineffective (*i.e.*, below the minimum effective dose). At high toxic levels, it can lead to mortality or morbidity (*i.e.*, above the maximum tolerated dose). Drug resistance is the primary reason for the failure of many therapies (*e.g.*, chemotherapy), hence the importance of real-time imaging and adjustments.[306]

Often, the SPION tracer and therapeutic molecules are co-loaded into the same nanoparticle. In this context, the SPION shell is commonly modified with pharmacologically active compounds. This can either be done *via* covalent bonds, or with physical intermolecular interactions, like π–π stacking.[107]
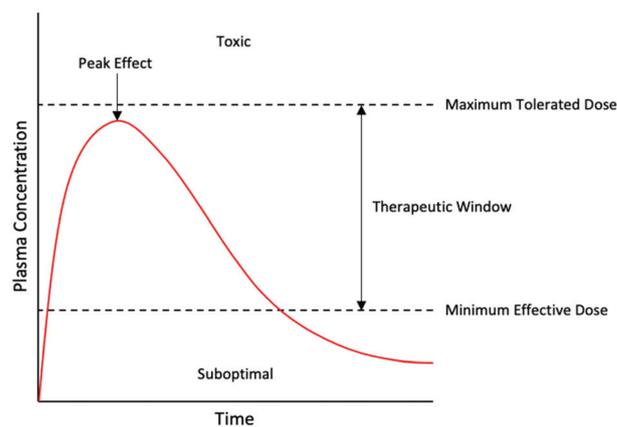
Fig. 19 The therapeutic window for an ideal drug. The red line represents the kinetics of the drug.

SPIONs have been conjugated to many different therapeutics. Most frequently, anti-cancer agents have been employed, from standard chemotherapeutic molecules like doxorubicin (DOX),[307] to more complex therapeutic compounds like siRNA.[308]

In recent years, there have been multiple attempts to assemble 'smart' multifunctional nanoparticles for theranostic applications, owing to their improved therapeutic and imaging capabilities.[309] A common approach here is in the development of nanoparticles with stimuli-responsive polymeric coatings. These coatings typically undergo reversible phase transitions in response to environmental stimuli alterations, most frequently temperature, pH, and enzymatic action. Zhu *et al.* designed the first 'smart' activatable probe for MPI drug delivery applications.[15] In this work, they prepared a nanocluster composed of a clustered SPION core with a PLGA coating. By loading the clinically relevant chemotherapeutic drug, DOX, into the PLGA matrix, this nanocluster (labelled SPNCD) can serve as both a dual drug delivery system and an MPI tracer (Fig. 20a). The PLGA shell degrades under mildly acidic biological environments (pH = 6.5), such as at a tumor site, permitting simultaneous DOX release and disassembly of the clustered SPIONs in the core (Fig. 20b). As the SPIONs are released, the MPI signal intensity increases as they recover their Brownian relaxation (Fig. 20c). This allows accurate quantitation and monitoring of drug release *in vitro* and *in vivo* (Fig. 20d and e).

Fuller *et al.* also composed magnetic nanocarriers combining high DOX loading and MPI capability (Fig. 20f).[21] Unlike SPNCD, these nanocarriers contain the drug within the hydrophobic core, along with the SPIONs, and are coated with a PEG-*block*-poly(lactic acid) block copolymer, for water solubility and colloidal stability. The release rate of SPIONs and DOX from the nanocarriers was also dependent on environmental pH (Fig. 20g). A different 'smart' agent based on the near-infrared-responsive plasmonic properties of tuned nanostars was developed by Tomitaka *et al* (Fig. 20h).[25] These engineered nanoparticles are composed of a SPION core and a star-shaped
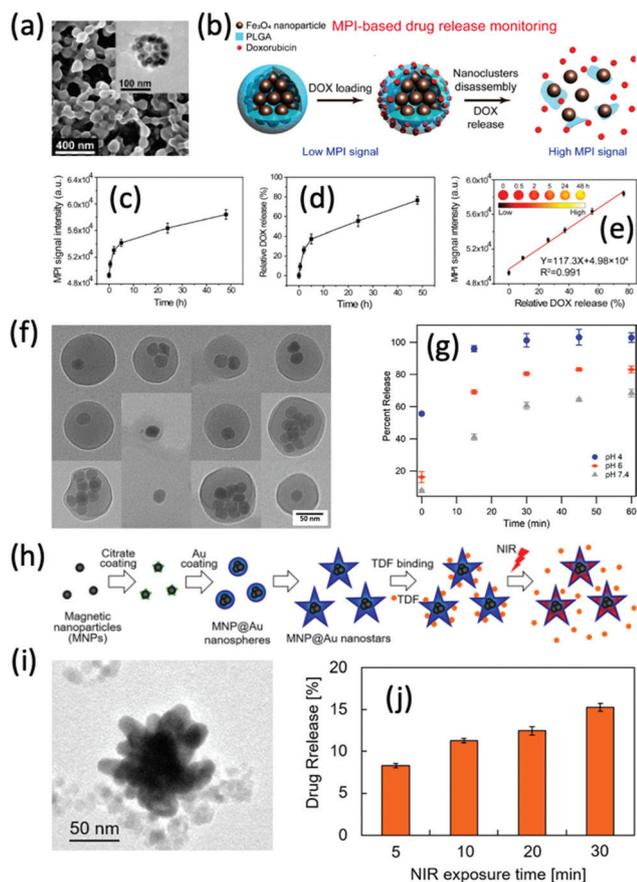
Fig. 20 MPI-tailored nanostructures, designed for drug delivery. (a) TEM image of SPNCD nanoclusters. (b) Schematic of the nanoclusters, demonstrating how degradation of the PLGA shell permits simultaneous DOX release and disassembly of the SPIONs clustered in the core. (c) *In vitro* MPI signal change as a function of time for SPNCD-labelled MDA-MB-231 cells, following degradation of the PLGA shell. (d) *In vitro* relative DOX release percentages as a function of time from SPNCD-labelled MDA-MB-231 cells, following degradation of the PLGA shell. (e) Correlation between DOX release percentage and MPI signal in cells. The curve exhibits perfectly linear behaviour. Reproduced with permission from ref. 15. Copyright 2019 American Chemical Society. (f) TEM image of DOX-loaded SPION-labelled nanocarriers. (g) Percent release of the nanocarriers as a function of time at 37 °C and varying pH values. Values of 4, 6, and 7.4 were selected for pH, representing the lysosomal, intratumoral, and vascular environments, respectively. Reproduced from ref. 21, with permission from Elsevier. (h) Schematic demonstrating the synthetic preparation, drug binding, and NIR-triggered drug release procedure of Tenofovir disoproxil fumarate (TDF)-loaded gold-coated SPION (MNP@Au) nanostars, where NIR is near-infrared radiation. (i) TEM image of the MNP@Au nanostars. (j) Drug release percentage from the nanostars following illumination with NIR for 5–30 min. Reproduced from ref. 25 with permission from Springer Nature. This is an open access article distributed under the terms of the CC BY License (https://creativecommons.org/licenses/by/4.0/). Copyright 2015, the authors. Article can be found at: https://www.nature.com/articles/s41598-020-66706-2. No changes were made to the original figure.

plasmonic shell, made up of high-aspect-ratio gold branches (Fig. 20i). Model drug molecules (TDF) are bound to the gold shell and can be triggered to release upon near-infrared illumination because of the photothermal effect in the shell

(Fig. 20j). Quantitative MPI can be used to monitor the drug release.

Around 30% of breast cancer tumors will metastasise, most commonly to the liver, lungs, brain and bone.[310] Brain metastases are of a particular concern as they are typically fatal. In the treatment of these brain metastases, targeted therapeutics may not be able to, or will have limited penetration, when attempting to cross the BBB, resulting in reduced treatment efficacy.[311] Extracellular vesicles (EVs) are small particles released by cells and are implicated in numerous biological processes, including metastasis. These particles may cross the BBB and can therefore be exploited to deliver therapeutic agents to brain metastases.[311,312] However, before further progress in this field, it is important to understand the activity, localisation, and accumulation of EVs during metastatic progression. Toomajian *et al.* demonstrated the tracking of SPION-labelled EVs within brain metastases using MPI.[313] For *in vivo* experiments, mice received an intracardiac injection of 4T1-BR Fluc/GFP cells, a breast cancer cell line that forms brain metastases and expresses firefly luciferase, which allows for BLI imaging of the metastases. 4T1 SPION-labelled EVs were subsequently injected at either early or late stages of metastatic progression and imaged using MPI and BLI to determine the timing of EV accumulation at the metastatic site. This multi-modal experiment demonstrated that EVs can successfully cross the BBB and accumulate in metastatic sites, implicating their therapeutic potential. With the successful tracking of EVs, this experiment also shows the potential for MPI monitoring of treatment.

Exosomes are a type of membrane-bound cell-derived EV, with diameters ranging from 30 to 200 nm.[314] They had previously been investigated as nanoparticle carriers for therapeutic delivery, but never imaged with MPI.[311,312] Jung *et al.* demonstrated *in vivo* MPI imaging of exosomes for the first time, where the exosomes were isolated from MDA-MB-231 human breast cancer cells and labelled with SPIONs and Olaparib.[314] Olaparib is an inhibitor of the poly (ADP-ribose) polymerase (PARP) enzyme involved in DNA repair, and is an established cancer therapy. This platform successfully monitors and targets therapeutic delivery towards hypoxic tumors, demonstrating theranostic potential. Imaging and treating these hypoxic regions is a crucial clinical challenge for effective cancer therapy as they are an important factor in therapeutic resistance.

5.2.2. Magnetic fluid hyperthermia. MFH treatment refers to when a suspension of MNPs, administered systemically or locally, is combined with an externally applied AMF to produce heat at a site of nanoparticle accumulation.[315] The heat is generated through the rapid switching of the SPION magnetisation and Brownian directions by the AMF. This hyperthermic effect can lead to tissue damage in the target area surrounding the nanoparticles. To achieve a therapeutic response in tissues using hyperthermia, two treatment approaches are generally employed.[315,316] In the primary approach, the temperature of the target tissue is increased to ~42 °C and held for a defined time. It is known that healthy tissues have reduced sensitivity

to hyperthermia as compared with cancerous cells and may withstand temperatures of 42–45 °C, where cancerous cells undergo apoptosis. This results in denaturation of proteins at the tumour site, and subsequent cell death. In the second approach, the target tissue is completely ablated, causing irreversible damage to the pathologic target, at temperatures <46 °C. Such temperatures lead to the necrosis of cancer cells but may also affect healthy cells, thus hyperthermia induced apoptosis is preferable. The specific absorption rate (SAR) is used to quantify the effectiveness of a specific SPION for MFH treatment. It is defined as the magnetic power absorbed per unit mass of magnetic material.[317]

The first proposed use of magnetic hyperthermia with iron oxide particles was as early as 1957,[318] yet it remains a prevalent research field today with significant work on the development of novel hyperthermia-tailored nanocarriers.[142,319] Interest as a therapeutic treatment can be attributed to multiple key advantages, including: no fundamental depth limitation, synergy with many other therapies (e.g., chemotherapies), and internalisation of the 'fluidic' heat source.[320] The most frequently used MFH application paradigms are whole-body MFH (Fig. 21a), where homogeneous AMF-generating alternating current (AC) coils scan the whole-body for sites of accumulation, and local MFH (Fig. 21b), where surface AC coils target localised areas of accumulation.[320] Despite the advantages, both approaches face several challenges towards further development and eventual clinical translation. Local MFH struggles with deep-seated treatment and therefore can only be used for treatments at the surface of the body. The most pressing issue for the clinical translation of the more commonly applied whole-body MFH is in the localisation of SPIONs at the target site. Systematically administered SPIONs, even if targeted, will end up in other critical organs like the liver and spleen, as well as the target site. This is challenging

since accumulation of SPIONs in off-target organs will increase their temperature during AMF application, leading to serious side effects.[315] Experiments in mice with systemically administered SPIONs and whole-body AMF show elevated liver enzymes, liver and spleen necrosis, and even death.[321]

To address these important technical challenges, several research groups have demonstrated theoretically and experimentally the benefits of the combined MFH and MPI approach, MPI–MFH (Fig. 21c).[177,178,322] The same principles for image generation in MPI, as described in section 2.1, can be modified to spatially select and localise thermal heat deposition to a desired region in biological tissue. MPI uses low sinusoidal excitation frequencies in the drive field, in the order of ~20 kHz, but by exciting SPIONs to higher frequencies of >300 kHz, heat can be generated.[320] The particles under the influence of the selection field are locked, and the particles in the FFR are free to rotate, as before, thereby restricting the SPION heating to the FFR alone. Combination with MPI also allows robust treatment planning. It provides precise quantitative imaging of the SPION distribution within the sample before heating, which is essential for quantification of particle accumulation at the target site and thus accurate SAR prediction and appropriate treatment.[315] As a result of this, and because the MPI-based gradients specifically limit the location of the hyperthermia to only a small, adjustable FFR in the sample, MPI–MFH may overcome the previous limitations with off-target heating experienced with whole-body MPI. The established physics of MPI also benefit MFH by providing high resolution targeting anywhere in the body and without depth limitation, addressing the primary problem encountered with local MFH.[320] Recently, newer designs for the FFR are being investigated where its size can be varied through alteration of the gradient field strength, thereby allowing correlation of treatment and dosage to the size of the lesion.[323]

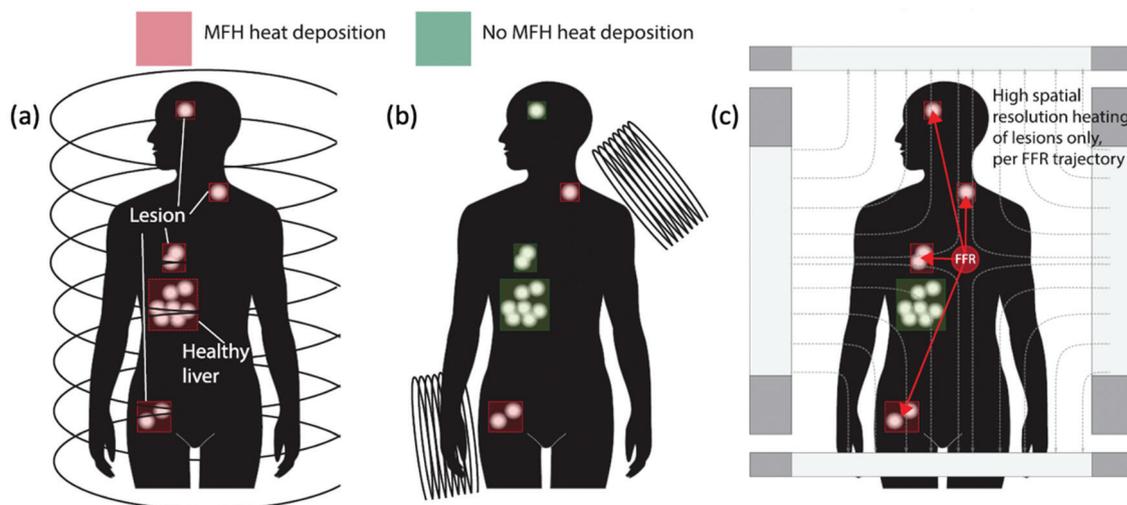**Fig. 21** (a) Whole-body MFH targets all tracer, including healthy sites of accumulation. (b) Local MFH targets tracers near the surface only. (c) MPI–MFH can selectively target tracer anywhere, including those deep in the body, while avoiding tracer accumulations in healthy sites. Reproduced with permission of IOP Publishing, from ref. 23; permission conveyed through Copyright Clearance Center, Inc.

As the physics germane to and exploited by MPI and MFH is similar, the same SPIONs can be used effectively for both. The techniques may also be integrated together in a single device for simultaneous MPI–MFH, that can seamlessly switch between imaging and heating modes through modulation of the AC excitation field magnitude, whilst the subject remains in the scanner. This provides opportunities for real-time diagnostic image monitoring and feedback. Hensley *et al.* developed the first combined MPI–MFH system, which establishes high heating resolution in phantoms.[23] In this work, they applied a 2.35 T m^{-1} magnetic gradient and a 353 kHz, 13 mT excitation frequency, which demonstrates on-demand selective heating of target components in phantoms, separated by just 3 mm (7 mm centre-to-centre distance). They were also able to repeatedly target these components for heating at will, achieving SAR deposition rates of up to 150 W g^{-1} and heating rates of 0.4 °C s^{-1}. This system was adopted by Tay *et al.* for *in vivo* studies.[179] Through this approach, they could localise thermal dose deposition in dual-tumor murine models with a spatio-thermal resolution of 7 mm, and with negligible toxic effects to nearby clearance organs such as the liver. Treatment efficacy and specificity were confirmed with BLI, with a 6-fold decrease in activity shown in the treated tumor and no damage to off-target tissue. More precise localisation of ~2.3 mm can be achieved by improving the gradient from 2.35 to 7 T m^{-1}, based on previous imaging and theory results.[324]

From these promising initial studies, commercial MPI–MFH instruments have been recently developed, one of which is the HYPER system (Magnetic Insight Inc., 0.5–2.6 T m^{-1} gradient field, scan at 340 kHz, 15 mT).[325] Gaudet *et al.* showcased the strong *in vitro* and *in vivo* results of this system, demonstrating precise and localised heating of the target.[325]

Over the last few years, there has been considerable work designing MPI- and hyperthermia-tailored SPIONs with high resolution and sensitivity, as well as efficient heating performance.[13,326] Generally, for better heating characteristics, SPIONs should have colloidal stability, phase purity, a narrow size distribution, and optimal magnetic properties.[327] In a recent study, Bleul *et al.* demonstrated the use of a micromixer synthesis platform (Fig. 22a) for the size-controlled synthesis of monodisperse single-core SPIONs, with a core diameter of ~30 nm.[9] These particles show promising theranostic capabilities with high signal amplitudes in MPI, and SAR values of up to 1 kW g(Fe)$^{-1}$, which exceeds the comparable SAR value of Resovist by more than a factor of three (Fig. 22b). Du *et al.* also designed monodisperse single-core SPIONs with improved hyperthermia therapy.[24] The hyperthermia performance can also be attributed to SPION surface functionalisation with CREKA, a peptide that actively targets fibrin–fibronectin complexes overexpressed in tumor interstitium, therefore improving delivery uniformity and enabling more effective cancer ablation.

Another factor that may affect the heating performance is the choice of coating material. Jordan *et al.* first noticed a SAR difference between dextran-coated and aminosilan-coated SPIONs, with aminosilan particles having a 1.2-fold greater SAR in identical particles.[328] Liu *et al.* then performed a systemic analysis of the SAR produced by SPIONs coated in different PEG molecular weights, observing a SAR increase with thinner coatings.[329] This is attributed to the dominance of Brownian relaxation based heat losses. However, it is noted that reducing the thickness may also affect the colloidal stability of the SPIONs, which detrimentally affects SAR. Differently, shape anisotropy in SPIONs has also been shown to improve hyperthermia performance, as is described in section 4.1. Khurshid *et al.* reported a 1.4-fold improvement in the particle SAR for cubic SPIONs over spherical SPIONs.[330] Bauer *et al.* also reported the high performance of cubic SPIONs, this time selectively doped with anisotropic zinc, increasing the overall anisotropy.[190] They observed a 2-fold enhancement of MPI signal and a 5-fold improvement in SAR, in comparison with equivalent undoped single-core spherical SPIONs.

5.2.3. Combinatorial therapy. The theranostic approaches described above can also be extended for combinatorial therapy, in which the actuated release of drugs from a nanocarrier can be achieved in combination with hyperthermia,

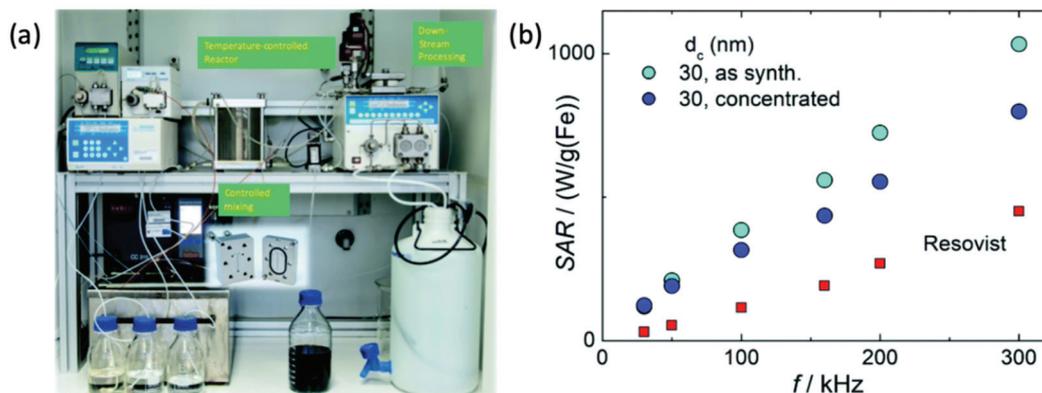**Fig. 22** MPI-tailored single-core SPIONs, designed for MPI–MFH. (a) Photograph of the micromixer system used for the synthesis of 30 nm monodisperse single-core SPIONs. (b) SAR values of the synthesised SPIONs as a function of frequency (f), in comparison to that of the reference, Resovist. Reproduced with permission of the Royal Society of Chemistry, from ref. 9; permission conveyed through Copyright Clearance Center, Inc.

providing great spatial and temporal control of release.[331] The amount of drug release can be tuned *via* alteration in the AMF field strength, and negligible release takes place when the particles are not subjected to an AMF. Maruyama *et al.* developed magnetic nanocarriers that encapsulate SPIONs and DOX, based on thermosensitive liposomes.[332] The results indicated the usefulness of MPI for both *in vitro* and *in vivo* studies for monitoring drug release through SPION release, following disruption of liposomal membranes by AMF-induced hyperthermia. However, these authors characterised the MPI performance of their liposomes using a prototype MPI scanner (400 Hz, 16 mT) that operates at higher drive field amplitudes and much lower drive field frequencies than most commercial scanners, and this influences the MPI resolution and signal intensity. Rost *et al.* demonstrated that the MPI performance of similar SPION-encapsulating liposomes is maintained using the commercially available MOMENTUM scanner (Magnetic Insight Inc., scan at 45 kHz, 16 mT).[180] In a different work, Fuller *et al.* developed a drug co-polymer conjugate encapsulating semispherical 18 nm single-core SPIONs and provided the proof-of-concept for spatially controlled drug release using an FFR, in this case following the breakage of a thermally-labile Diels–Alder bond.[333] The release can potentially be monitored with MPI and activated numerous times, and the magnetic field gradients can be used to spatially control the region of release, thus preventing damage to off-target tissue.

5.3. Perfusion imaging

Perfusion imaging is a technique whereby the passage of a tracer is monitored continuously through the capillary tissue bed, capturing any temporal changes in the tracer. It has seen extensive application in the diagnosis and detection of various pathophysiology's related to blood perfusion and vascular changes. Stemming from the short scanning time and high temporal resolution of MPI, it has become possible to monitor perfusion and blood-flow in real-time.[3] The speed at which images are captured would substantially benefit diseases for which a rapid assessment of the vasculature and perfusion are mandatory for the treatment. Another beneficial property of MPI for perfusion imaging is the high contrast-to-noise, permitting higher accuracy imaging that compares favourably to the traditionally applied techniques of contrast-enhanced CT or MRI, which produce unreliable perfusion images.[334]

Neuropathological diseases such as ischemic stroke, and traumatic brain injury (TBI) are severe conditions requiring immediate medical attention and extensive monitoring following treatment. Specifically stroke, with 17 million cases worldwide every year, is one of the leading annual causes of death and disability.[170] Rapid high quality cerebral perfusion imaging is fundamental in successful stroke diagnosis and management, as it allows for early assessment of penumbra volume and location, as well as in predicting which patients may benefit from cerebral revascularisation therapies.[335] The low temporal resolution of perfusion MRI and CT can cause variations in the penumbra volume estimate, which may affect optimal stroke treatment.[336,337] In a pivotal study, Ludewig

et al. demonstrated the potential of MPI in the real-time perfusion imaging and diagnosis of acute stroke in a rodent model.[170] Cerebral ischemia was induced in the internal carotid artery of C57BL/6 mice, and within seconds and a single injection of long-circulating LS-008 SPIONs, cerebral perfusions could be assessed by MPI. The signal lowered in the ischemic hemisphere, allowing precise detection of an ischemic stroke within a few cubic millimetres. The SPIONs persist in the bloodstream for hours following injection, without any leakage into the brain interstitium.

Long-circulating tracers are crucial in most perfusion imaging applications, enabling blood flow and blood volume studies. Orendorff *et al.* exhibited their importance in the imaging of TBI, where a closed-head rat model was monitored longitudinally to study cerebral bleeding caused by an impact, as well as changes in the blood pool as the wound heals.[169] This work utilised single-core LS-13 nanoparticles (LodeSpin Labs) that show a circulation half-life of approximately 4–6 h. Such times allowed infiltration into the blood pools in the interstitial space, and thus successful monitoring of TBI with MPI over long time scales, without significant signal loss.

In addition to TBI imaging, MPI has shown great promise for various other blood pool imaging applications, including the detection of gastrointestinal (GI) bleeding. GI bleeding is a serious clinical issue associated with the haemorrhaging of organs in the digestive system, yet its diagnosis remains very challenging. Traditionally, diagnosis is achieved using scintigraphy techniques in which a red blood cell (RBC) is tagged using a radioisotope like ^{99m}Tc.[338] However, the bleeding site must be located quickly for rapid diagnosis and intervention, and the long hot chemistry preparation times for ^{99m}Tc RBCs are not ideal.[339] An accurate and timely diagnosis method is therefore essential to reduce morbidity and mortality, and for the determination of transfusion requirements. Yu *et al.* demonstrated that MPI could be utilised for the safe and quantitative detection of GI bleeding, without any hot chemistry preparation time.[58] This work was applied to a murine model that is genetically predisposed to polyp development in the GI lumen (Apc$^{Min/+}$), with subsequent heparin injection to induce acute GI bleeding. Following the injection of long-circulating MPI-tailored SPIONs (single-core LS-017, LodeSpin Laboratories) through the tail vein, dynamic MPI projection images could be analysed to show tracer accumulation in the lower GI tract. These images illustrate that acute GI bleeding could be detected with high sensitivity using MPI *in vivo*, with bleed rates as slow as 1 to 5 μL min^{-1}.

Accurate imaging of lung perfusion is required for the diagnosis of conditions like pulmonary embolism (PE), as many patients experience mild or non-specific symptoms. PE carries a 30% mortality rate when left untreated, however following time-sensitive detection and treatment, this mortality rate may reduce to ~8%.[27] Zhou *et al.* reported the first MPI-based lung perfusion study *in vivo* in a healthy rat model.[27] In this work, they utilised novel multi-core SPIONs that are conjugated to macroaggregated albumin (MAA), aptly termed MAA–SPIONs (Fig. 23a). These are administered intravenously where the par-
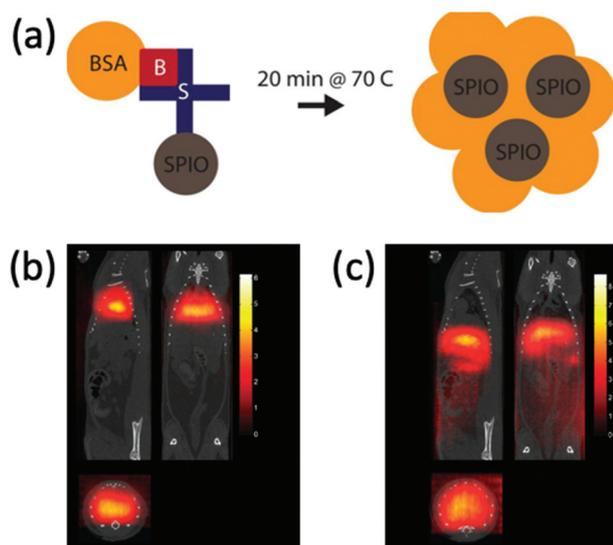
Fig. 23 MPI-tailored MAA–SPIONs, designed for lung perfusion imaging. (a) Schematic demonstrating the synthetic preparation of MAA–SPIONs, where biotinylated albumin is conjugated to streptavidin-functionalized SPIONs, and then heated with stirring to form macroaggregates, and B is biotin, S is streptavidin, and BSA is bovine serum albumin. *In vivo* 3D MPI scans of rats 10 min following intravenous injection, with coronal, sagittal and axial maximum intensity projections (MIPs) shown, where the distribution of (b) MAA–SPIONs are compared with that of the reference, (c) unconjugated SPIONs. Reproduced with permission of IOP Publishing, from ref. 27; permission conveyed through Copyright Clearance Center, Inc.

ticles effectively pass through the lung capillaries after 15 min as the MAA–SPION size is larger than that of the capillary diameter, becoming entrapped in the lung capillary bed (Fig. 23b). This enables the accurate and reliable diagnosis of any vascular related pulmonary defects. In comparison, non-conjugated SPIONs alone cannot target the lung and are instead immediately cleared to the liver and spleen (Fig. 23c). 3D MPI lung perfusion images are comparable in quality to that of traditionally used scintigraphy and SPECT with MMA-conjugated ^{99m}Tc, whilst also demonstrating advantages over many modalities due to no air-tissue interface artifacts nor ionising radiation. In a different study, Tay *et al.* showed that inhaled multi-core SPIONs can be tracked and quantified with MPI in mice, with accuracies comparable to radiolabelled aerosols.[158] When taken with the results from Zhou *et al.*,[27] the authors demonstrated a proof-of-concept for MPI-based perfusion–ventilation mapping.[340] This mapping has been applied clinically using other modalities, for the diagnosis of PE and in preoperative evaluation of the lungs.

5.3.1. Cancer detection and screening. The rate of cancer curing almost directly correlates with the stage at which it is diagnosed, meaning that if it was diagnosed and provided with appropriate treatment at an earlier stage, the cure rate would increase significantly.[341] Biomedical imaging plays a key role in all phases of clinical cancer management. The most important challenge in cancer imaging is the ability to reliably

distinguish the tumor from healthy tissue. Current anatomical imaging techniques, like MRI and CT, are useful in detecting changes in the tissue architecture that generally accompany cancer, but the tumor contrast generated is not sufficiently different from healthy tissues for confident diagnoses.[342] This is most true for metastatic and diffuse tumors. MPI displays excellent contrast, and thus shows great promise for earlier cancer detection and staging than other current imaging methods.

For tumour visualisation, SPIONs must first become localised within the tumor. Currently this process has relied on the enhanced permeability and retention (EPR) effect, otherwise known as 'passive targeting'.[343,344] This is a phenomenon observed in cancer where the improper alignment of endothelial cells, poor drainage of the lymphatic system, and leaky vasculature of a growing tumor allow larger sized therapeutic agents, like SPIONs or antibodies, access to the interstitial portion of the tumor, to some extent (Fig. 24). This leads to substantial non-targeted accumulation of such agents, at concentrations several folds higher than in the plasma.[343]

Yu *et al.* demonstrated the EPR phenomenon with MPI for the detection of triple negative breast cancer xenograft tumors in an immune deficient murine model.[92] Long-circulating LS-008 tracers were administered intravenously through the tail vein, and MPI exhibited quantitative visualisation of the tracer dynamics in the tumor over time, showing initial EPR wash-in into the tumors, and delayed wash-out 48 h later. Notably, the tumor can clearly be detected with MPI, even with large cardiac and liver signals, highlighted with a tumor-to-background ratio of up to 50.

There have also been various examples of non-targeted SPIONs that have been specifically developed to exploit the EPR effect for MPI, demonstrating significant increases in accumulation and MPI signal in tumors based on passive targeting alone.[10,28] Additionally, to improve the specificity and uptake of SPIONs for cancer detection and imaging, and as passive targeting is not possible in all tumors, there have also been many cases of researchers binding tumor biomarker targeting moieties to SPIONs for MPI.[4,24,30] This active targeting should further improve the capability of MPI for early cancer diagnosis.
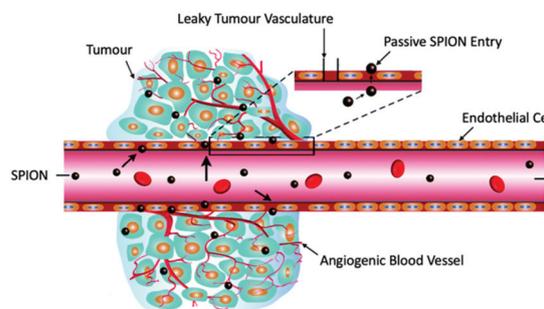

Fig. 24 Schematic representation of the EPR effect. Reproduced with permission of the Royal Society of Chemistry, from ref. 7; permission conveyed through Copyright Clearance Center, Inc.

5.3.2. Angiography. The rate of cancer curing almost directly correlates with the stage at which it is diagnosed, meaning that if it was diagnosed and provided with appropriate treatment at an earlier stage, the cure rate would increase significantly.[341] Biomedical imaging plays a key role in all phases of clinical cancer management. The most important challenge in cancer imaging is the ability to reliably distinguish the tumor from healthy tissue. Current anatomical imaging techniques, like MRI and CT, are useful in detecting changes in the tissue architecture that generally accompany cancer, but the tumor contrast generated is not sufficiently different from healthy tissues for confident diagnoses.[342] This is most true for metastatic and diffuse tumors. MPI displays excellent contrast, and thus shows great promise for earlier cancer detection and staging than other current imaging methods. One of the most compelling applications of MPI is in safe angiography. MPI angiograms allow visualisation of the vasculature. This is of great importance in the diagnostics of many vascular diseases, potentially detecting abnormalities such as deep vein thrombosis, aneurysms, or stenosis. The earliest *in vivo* experiment carried out using MPI was the real-time 3D imaging of the blood-flow in a beating mouse heart.[50] These images displayed large vessels like the vena cava, as well as the cardiac chambers. However, the heart and vena cava of mice have been scanned numerous times since then, with more sophisticated MPI-tailored tracers,[218] and with various improved MPI systems, incorporating advances in MPI technology.[218,233,345] With these advances, there is an obvious improvement in angiographic image quality.

Kaul *et al.* demonstrated the improvement in angiographic imaging quality of single-core LS-008, a tracer tailored towards angiography and blood pool imaging in MPI, over MRI-tailored multi-core Resovist.[3] For *in vivo* experiments, the tracers were injected into equivalent healthy mice. Whilst both tracers could visualise the propagation of the bolus through the inferior vena cava (Fig. 25a and b), LS-008 clearly displayed fewer temporally fluctuating artifacts, and the signal modulation in the caval vein, resulting from periodic cardiac and respiratory motion, could be obviously depicted. Additionally, the aorta was clearly distinguishable from the caval vein (Fig. 25c), and several further vessel structures and processes could be observed and monitored that were missing with Resovist. These results demonstrate that regarding the quality of delineation and number of visualised vessels, tailored LS-008 outperforms Resovist in angiographic and perfusion MPI.

In a similar study, Mohtashamdolatshahi *et al.* compared the *in vivo* imaging quality of angiographic MPI for newly developed multi-core particles (MCP 3),[206] and Resovist, in the inferior vena cava and aorta.[346] The tracers were administered intravenously into the tail veins of rat models at doses of 0.1, 0.05 and 0.025 mmol Fe kg^{-1}. This was followed by serial MPI acquisition using a commercial MPI system. The MCP 3 MPI images demonstrated a significantly higher image quality than those with Resovist. Following administration of MCP 3 at dosages of 0.1, and clinically acceptable 0.05 mmol Fe kg^{-1}, morphological features such as vessel lumen diameters of the
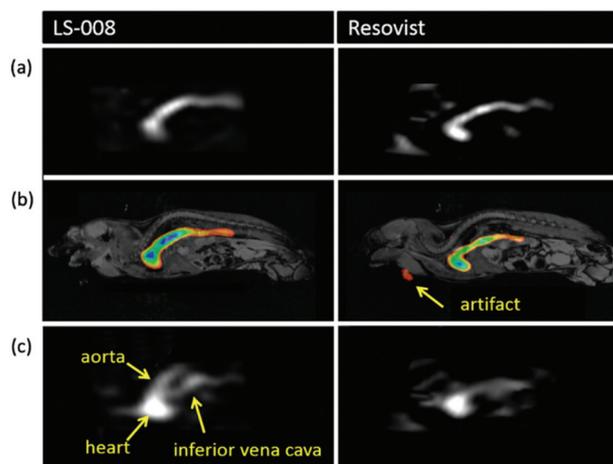

Fig. 25 A comparison between angiographic images produced in mice with MPI, using MPI- and angiography-tailored SPIONs, LS-008 (left column), and a reference, Resovist (right column). Propagation of the bolus through the inferior vena cava to the heart for (a) just the MPI signal, and (b) the MPI signal co-registered with MRI. (c) MPI image clearly displaying the aorta leaving the heart when implementing LS-008, but not when implementing Resovist. Reproduced with permission of IOP Publishing, from ref. 3; permission conveyed through Copyright Clearance Center, Inc.

inferior vena cava and abdominal aorta could be assessed, which was not possible with Resovist images at any dosage. Additionally, there are fewer severe background noise artifacts than with Resovist images. It can therefore be said that MCP 3 increased the visibility of vessel lumens *in vivo* in MPI, towards the possible detection of vascular abnormalities.

Differently, Kaul *et al.* demonstrated the potential of MPI for quantifiable measurements of *in vivo* blood-flow velocities.[347] This study was performed in the inferior vena cava of healthy mice, and the images obtained with MPI were compared with those from MRI. Analysis revealed good agreement between the *in vivo* velocities, with MRI at 4.0 ± 1.5 cm s^{-1} and MPI at 4.8 ± 1.1 cm s^{-1}. They also performed an *in vitro* study, where a phantom setup mimicking the flow within the inferior vena cava concluded that velocities of up to 21 cm s^{-1} can be captured by MPI as they occur.

Recently, Molwitz *et al.* obtained the first angiographic MPI images from organs of human-size.[348] This work was performed using a multi-modal *ex vivo* porcine kidney perfusion system compatible with MPI and well-established magnetic resonance angiography (MRA). This developed system practically evaluates MPI's potential for human-sized angiography, which is especially relevant as current angiography-suited MPI scanners still suffer from subject size and spatial resolution restrictions. All the visible vessels in MRA and MPI were counted and compared, where 33% of all vessels imaged in MRA were visible in MPI. This difference is likely a result of the restricted spatial resolution in MPI. Despite these current limitations, this work does demonstrate MPIs capability for detecting vessels within a single human-sized organ and will be useful for improving MPI's angiographic potential.

5.3.3. **Nanowarming of cryopreserved organs.** The shortage of available donated organs is one of the greatest crises facing modern medicine today, with many patients dying whilst waiting for potentially lifesaving organs. One of the reasons donated organs never reach a recipient is that they exceed their preservation window following removal.[349] There is therefore a dire need for better-quality organ preservation strategies that enable the biobanking of organs and extend their preservation times. Through this, compatible donor to-recipient matching would be possible, allowing extensive treatment planning and decreased recipient organ rejection.[349] One method of particular interest for storage is cryopreservation, where the organ is rapidly cooled to extreme low temperatures.[350] However, this technique is not without its challenges. Cryopreservation agents are toxic and require rapid cooling to vitrify and even more rapid warming to avoid devitrification. Currently applied warming modalities lead to temperature gradients and nonuniform rewarming, as well as thermal stresses that can damage larger organs.[351] These warming limitations can be overcome through application of a nanowarming method, which enables fast and uniform volumetric heating of cryopreserved tissues. In nanowarming, SPION-containing magnetic cryopreservation agents (mCPAs) are uniformly perfused within the target tissue, prior to vitrification.[351] The SPIONs can then be heated when the tissue is required through application of an external AMF, which is capable of penetrating the entire tissue volume without attenuation.

Chiu-lam et al. reported the first successful example of the cryopreservation and nanowarming process in a whole organ, using an mCPA solution.[350] 3D MPI was chosen as an appropriate non-invasive and quantitative technology to evaluate the distribution of the perfused mCPA within the organ. MPI demonstrated that a stable mCPA solution containing a VS55 cryopreservation agent, and especially formulated non-toxic SPIONs that have exceptional stability within VS55, can uniformly perfuse whole rat hearts. Once this uniformity was determined, the hearts were successfully vitrified, cryopreserved in liquid nitrogen for up to 1 wk, and rapidly nanowarmed in a uniform fashion to room temperature using an AMF. These formulated SPIONs demonstrated ultrafast nanowarming rates (>320 °C min^{-1}), that can be controlled with AMF amplitude. To complete the process, the SPIONs were subsequently perfused out, at a 95% success rate as determined by MPI. In this work, there was no evidence of macroscopic damage or stress to the hearts after the processes of vitrification, cryopreservation, and nanowarming. These results support the potential of nanowarming, utilising MPI to visualise mCPA distribution, as a strategy for biobanking tissues for transplantation, potentially significantly enhancing the availability of viable donor organs.

6. Multi-colour MPI

Recently, it has been demonstrated that MPI can take advantage of SPIONs with differential magnetic relaxation or harmonic response behaviors to generate multiple contrasts, enabling 'multi-colour' imaging and the ability to measure distinct signals corresponding to a specific particle subtype.[352,353] This enablement of MPI to simultaneously measure and separate the signal generated by different SPION types would be useful for many applications in the fields of intervention, therapy, and medical imaging.

Multi-colour imaging was first experimentally realised using x-space and SFR-based approaches. Hensley et al. demonstrated that x-space reconstruction is capable of differentiating between the relaxation behaviors of different SPIONs, with multiple measurements at different drive field amplitudes.[354] Rahmer et al. demonstrated that different SPIONs could be differentiated based on the differences in their harmonic response through the SFR approach, where an extensive calibration procedure was performed separately for each SPION type.[38] Through the x-space reconstruction process, the work was first extended to in vivo imaging, where the images successfully differentiate between MAA–SPION tracers in the lungs and Chemicell tracers in the liver of a murine model.[355] However, the x-space and SFR approaches rely on extensive calibrations or measurements to capture the differences in the relaxation behaviors or harmonic responses of the nanoparticles. To negate this, Muslu et al. proposed a calibration-free method for x-space MPI, where no prior information about the SPIONs is required.[356] This technique can generate a multi-colour relaxation time constant map of different SPION types from a single back and forth scan of the FOV, at a single drive field amplitude.

There has been significant progress in using multi-colour MPI for catheter tracking during vascular interventions.[357] In such applications, one SPION type is injected into the blood stream for vessel visualisation, whilst a different type of SPION is used to coat a catheter. Multi-colour MPI can discriminate between the particles impregnated in the catheter and those flowing in the vessels. In a recent work, following the staining of a blood vessel phantom and catheter with different SPIONs, Rahmer et al. demonstrated how 3D real-time multi-colour MPI feedback with an online reconstruction can be used to steer the catheter into a desired vessel phantom, following implementation of an external magnetic field.[358]

With multi-colour MPI, it is not only possible to distinguish between particles with different characteristics, but also identical particles in different environments.[359] Multi-colour MPI can therefore be used to map information relating to the local microenvironment. There are many potential environmental factors where changes could produce different MPI signals. Essentially any factor that causes change in the particle spectrum could form a basis for discrimination. For instance, the temperature mapping capability of multi-colour MPI is well documented, with identical SPIONs in differently heated environments able to be differentiated.[360,361] Recently, Paysen et al. were even able to discriminate between free and cell-bound SPIONs by their relaxation behavior, forming multi-colour images (Fig. 26a and b).[2] They quantified the dynamic changes that occur when free SPIONs come into contact with and are internalised by cells in vitro over time, without any damage to the cells.
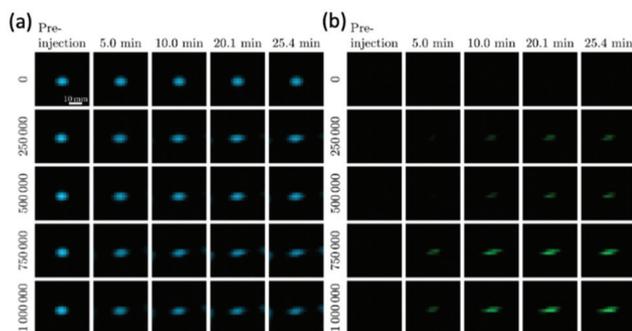
Fig. 26 Multi-colour MPI images that distinguish between free and cell-bound SPIONs. Reconstructed MPI images displaying the distribution of (a) free and (b) cell-bound SPIONs in contact with THP-1 cells, as a function of time. Number of cells injected are displayed along the left-hand side of each figure. Following injection, there is an increasing intensity of cell-bound SPIONs in (b) over time as they become internalised. Reproduced from ref. 2 with permission from Springer Nature. This is an open access article distributed under the terms of the CC BY License (https://creativecommons.org/licenses/by/4.0/). Copyright 2020, the authors. Article can be found at: https://www.nature.com/articles/s41598-020-58853-3. No changes were made to the original figure.
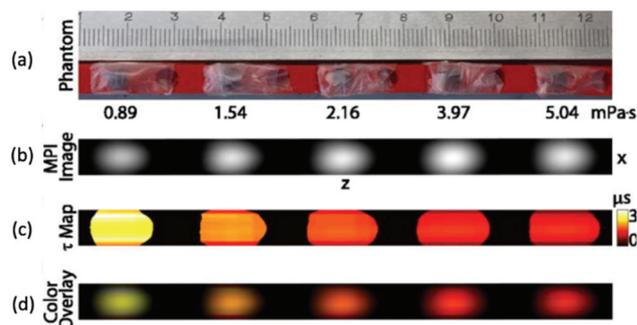

Fig. 27 Multi-colour MPI images for viscosity mapping. (a) An imaging phantom of 5 different samples of SPIONs in increasing viscosity levels from 0.89 mPa s to 5.04 mPa s. (b) The MPI images for each sample, with (c) their corresponding relaxation (τ) maps. (d) The color overlay between the τ maps and MPI images for each sample. Reproduced with permission of IOP Publishing, from ref. 22; permission conveyed through Copyright Clearance Center, Inc.

There has been sustained work in viscosity mapping with multi-colour MPI.[362] Certain diseases, like cancer and atherosclerosis, are known to significantly increase the levels of cellular viscosity. These diseases can be potentially probed with MPI, through tissue viscosity measurements at the locations of SPION accumulation.[22] Möddel *et al.* reported a method that allowed them to experimentally determine the viscosity of a small sample using a novel multi-colour reconstruction approach.[363] This approach was adapted from a previously reported method for temperature mapping with MPI.[361] A series of samples with differing viscosities were prepared with glycerol/distilled water mixtures of varying proportions and a fixed concentration of Resovist. Using these samples, they were able to determine the viscosity of the particle environment within a range of 1.0–51.8 mPa s, with a methodological error of 6%. More recently, Utkur *et al.* demonstrated the results of relaxation-based multi-colour MPI for viscosity mapping.[22] An imaging phantom that contained SPION samples at five different viscosity levels was prepared (Fig. 27a), again using water/glycerol mixtures of varying proportions. The resulting samples covered the biologically relevant viscosity levels, with values between 0.89 mPa s and 5.04 mPa s. Using the relaxation time constant estimation technique outlined by the same group,[356] they showed that relaxation-based experiments can distinguish multi-core SPIONs within the biologically relevant viscosity range (Fig. 27b–d).

7. Clinical translation

Commercial pre-clinical MPI scanners are only available through Magnetic Insight Inc. and Bruker GmbH. Pre-clinical

system specifications are slowly improving as researchers have been highly active in designing improved software for image acquisition and reconstruction.[35,37,39,40,364–372] For example, von Gladiss *et al.* recently demonstrated the advantages of a hybrid system matrix for efficient calibration and image reconstruction.[373] To scale-up MPI hardware to human-size, there are several notable safety considerations and ergonomic challenges that must be overcome. Most notably, issues regarding potential allergic reactions to SPION injections,[374–376] and the higher cost and power consumption requirements for the larger field amplitudes needed for sufficient image resolution at a clinical scale.[80] Initially, tissue heating and peripheral nerve stimulation resulting from time-varying magnetic fields was also thought be an issue. However, studies have demonstrated that the physical properties of the magnetic fields required for scanning human-sized volumes in MPI can be tuned as to not cross the limit at which these effects are generated, without having a negative effect on performance.[377–379]

Despite these obstacles, there has been sustained work on the translation and hardware scale-up.[42,43,79,234,380,381] In the design of a functional MPI brain imager, Mason *et al.* developed simulation studies that demonstrated promising capabilities for human-scale systems.[382] In an alternative approach Graeser *et al.* successfully presented a human-sized MPI hardware set-up, tailored for brain applications, that has low technical requirements for fast and flexible operation in a clinical environment.[383] For a different application, Mason *et al.* also developed a highly sensitive small-bore 2D FFL MPI projection imager, that can rapidly image the distribution of tumors in excised breast tissue, from intravenously injected SPIONs, during breast-conserving surgery treatments for breast cancer.[384] This work shows the potential for MPI as a clinical solution to issues with positive margins often seen in such surgeries.

Another vital area for focus in advancement towards clinical MPI is in the development and commercialisation of SPIONs tailored towards MPI physics. Currently, no such SPIONs have

been approved for clinical treatment, yet it has already been demonstrated that enhanced MPI performance can be realised through specific SPION design, with improvements in for example, MPI spatial resolution and sensitivity.[14,16,218,242,244,245] Notably, further optimisation of the SPIONs for spatial resolution can be traded-off for lower MPI gradients, lowering the overall cost of MPI implementation and easing the scale-up of hardware to human size.[229] With different cores, coatings, and the potential conjugation of targeting and therapeutic moieties, it is anticipated that SPIONs will be designed for many different applications and diseases. Particularly, there has been increased interest in the design of smart multifunctional nanoparticle assemblies for drug delivery applications.[15,21,25,180,332,333] This work could be extended to designing activatable nanomaterials where the breakdown and release of SPIONs is triggered by enzyme activation. Such particles could be used to measure enzymatic levels in an *in vivo* area through enzymatic sensing.

8. Conclusions and perspectives

MPI is an emerging radiation-free imaging modality that utilises sensitive, safe, and biocompatible SPIONs as its tracing material. It demonstrates totally unambiguous depth-independent detection of these tracers, negligible background signal, and superb image sensitivity, which enables an essentially infinite contrast and the production of highly specific images with very low detection limits. MPI is also truly linearly quantitative, demonstrating an almost perfectly linear relationship between MPI signal and iron content, allowing estimation of SPION concentration in target tissues, based on just the signal intensity. This quantitation can even be demonstrated in regions that are challenging for other modalities, like the lungs or bone marrow. These great advantages enable a variety of applications of clinical relevance, as well as unprecedented new applications that were inaccessible using other modalities. Recently, impressive progress has been made in pre-clinical animal studies, in areas such as MFH, drug delivery, inflammation imaging, cell tracking, and perfusion imaging.

For advancing the biomedical applications of MPI, the design of optimal SPIONs and rigorously controlled syntheses have also become important topics of research. Great progress has been made, with many new SPIONs, and other MNPs, demonstrating impressive improvements in general MPI performance,[5,10,14] and performance in specific MPI applications.[15,190,218] Critical parameters to control include the size and shape of the core, the specific functionalisation, and of upmost importance, assessing whether a single- or multi-core is appropriate for an intended application.

Despite the sustained research, there is plenty of space for the further expansion of MPI. The development of multicolour MPI and its reconstruction approaches would drive the modality forward, extracting information relating to the local nanoenvironment that could be used in therapy and diagnostics. Viscosity mapping for example, should be applied in the detection of blood coagulation or diseases that are related to viscosity changes. In addition, MPI has been only recently applied to the nanowarming of cryopreserved organs, where it is implemented to quantitatively assess SPION loading in an organ before vitrification and after nanowarming.[350] To further this, nanowarming could potentially be coupled with the capability of MPI to control the location of SPION heating.[179] This would facilitate great control over the resulting temperature distribution during the rewarming process. There has also been encouraging progress in the design and development of hybrid scanning systems where MPI is merged with complementary imaging techniques to improve imaging quality, such as in MPI/MRI and MPI/CT.[122,123,126,127,132]

With multiple promising approaches for clinical translation, improved SPION design, and sustained research into the great number of biomedical applications of clinical promise, it can be anticipated that MPI will be a crucial complimentary clinical diagnostic and therapeutic tool in the near future.

Author contributions

Stanley Harvell-Smith: Investigation, visualization, writing – original draft, writing – review & editing. Le Duc Tung: Writing – review & editing. Nguyen T. K. Thanh: Conceptualization, supervision, writing – review & editing.

Conflicts of interest

There are no conflicts to declare.

Acknowledgements

References

1 L. Gloag, M. Mehdipour, M. Ulanova, K. Mariandry, M. A. Nichol, D. J. Hernandez-Castillo, J. Gaudet, R. R. Qiao, J. Zhang, M. Nelson, B. Thierry, M. A. Alvarez-Lemus, T. T. Tan, J. J. Gooding, N. Braidy, P. S. Sachdev and R. D. Tilley, *Chem. Commun.*, 2020, **56**, 3504–3507.

2 H. Paysen, N. Loewa, A. Stach, J. Wells, O. Kosch, S. Twamley, M. R. Makowski, T. Schaeffter, A. Ludwig and F. Wiekhorst, *Sci. Rep.*, 2020, **10**, 1922.

3 M. G. Kaul, T. Mummert, C. Jung, J. Salamon, A. P. Khandhar, R. M. Ferguson, S. J. Kemp, H. Ittrich, K. M. Krishnan, G. Adam and T. Knopp, *Phys. Med. Biol.*, 2017, **62**, 3454–3469.

4 H. Arami, E. Teeman, A. Troksa, H. Bradshaw, K. Saatchi, A. Tomitaka, S. S. Gambhir, U. O. Hafeli, D. Liggitt and K. M. Krishnan, *Nanoscale*, 2017, **9**, 18723–18730.

5   S. K. Avugadda, S. Wickramasinghe, D. Niculaes, M. Ju, A. Lak, N. Silvestri, S. Nitti, I. Roy, A. C. S. Samia and T. Pellegrino, *Nanomaterials*, 2020, **11**, 62.

6   P. Prajapati and D. W. Lambert, *J. Bone Oncol.*, 2016, **5**, 128–131.

7   Y. Dai, C. Xu, X. Sun and X. Chen, *Chem. Soc. Rev.*, 2017, **46**, 3830–3852.

8   J. E. Lemaster, F. Chen, T. Kim, A. Hariri and J. V. Jokerst, *ACS Appl. Nano Mater.*, 2018, **1**, 1321–1331.

9   R. Bleul, A. Baki, C. Freese, H. Paysen, O. Kosch and F. Wiekhorst, *Nanoscale Adv.*, 2020, **2**, 4510–4521.

10 G. Song, M. Kenney, Y. S. Chen, X. Zheng, Y. Deng, Z. Chen, S. X. Wang, S. S. Gambhir, H. Dai and J. Rao, *Nat. Biomed. Eng.*, 2020, **4**, 325–334.

11 H. Nejadnik, P. Pandit, O. Lenkov, A. P. Lahiji, K. Yerneni and H. E. Daldrup-Link, *Mol. Imaging Biol.*, 2019, **21**, 465–472.

12 G. Song, M. Chen, Y. Zhang, L. Cui, H. Qu, X. Zheng, M. Wintermark, Z. Liu and J. Rao, *Nano Lett.*, 2018, **18**, 182–189.

13 N. Silvestri, H. Gavil, P. Guardia, R. Brescia, S. Fernandes, A. C. S. Samia, F. J. Teran and T. Pellegrino, *Nanoscale*, 2021, **13**, 13665–13680.

14 Z. W. Tay, S. Savliwala, D. W. Hensley, K. L. B. Fung, C. Colson, B. D. Fellows, X. Zhou, Q. Huynh, Y. Lu, B. Zheng, P. Chandrasekharan, S. M. Rivera-Jimenez, C. M. Rinaldi-Ramos and S. M. Conolly, *Small Methods*, 2021, 2100796.

15 X. Zhu, J. Li, P. Peng, N. H. Nassab and B. R. Smith, *Nano Lett.*, 2019, **19**, 6725–6733.

16 M. Unni, A. M. Uhl, S. Savliwala, B. H. Savitzky, R. Dhavalikar, N. Garraud, D. P. Arnold, L. F. Kourkoutis, J. S. Andrew and C. Rinaldi, *ACS Nano*, 2017, **11**, 2284–2303.

17 P. Chandrasekharan, K. L. B. Fung, X. Y. Zhou, W. Cui, C. Colson, D. Mai, K. Jeffris, Q. Huynh, C. Saayujya, L. Kabuli, B. Fellows, Y. Lu, E. Yu, Z. W. Tay, B. Zheng, L. Fong and S. M. Conolly, *Nanotheranostics*, 2021, **5**, 240–255.

18 Q. Y. Wang, X. B. Ma, H. W. Liao, Z. Y. Liang, F. Y. Li, J. Tian and D. S. Ling, *ACS Nano*, 2020, **14**, 2053–2062.

19 O. C. Sehl, A. V. Makela, A. M. Hamilton and P. J. Foster, *Tomography*, 2019, **5**, 367–376.

20 S. Liu, A. Chiu-Lam, A. Rivera-Rodriguez, R. DeGroff, S. Savliwala, N. Sarna and C. M. Rinaldi-Ramos, *Nanotheranostics*, 2021, **5**, 348–361.

21 E. G. Fuller, G. M. Scheutz, A. Jimenez, P. Lewis, S. Savliwala, S. Liu, B. S. Sumerlin and C. Rinaldi, *Int. J. Pharm.*, 2019, **572**, 118796.

22 M. Utkur, Y. Muslu and E. U. Saritas, *Phys. Med. Biol.*, 2017, **62**, 3422–3439.

23 D. Hensley, Z. W. Tay, R. Dhavalikar, B. Zheng, P. Goodwill, C. Rinaldi and S. Conolly, *Phys. Med. Biol.*, 2017, **62**, 3483–3500.

24 Y. Du, X. Liu, Q. Liang, X. J. Liang and J. Tian, *Nano Lett.*, 2019, **19**, 3618–3626.

25 A. Tomitaka, H. Arami, A. Ahmadivand, N. Pala, A. J. McGoron, Y. Takemura, M. Febo and M. Nair, *Sci. Rep.*, 2020, **10**, 10115.

26 B. Zheng, T. Vazin, P. W. Goodwill, A. Conway, A. Verma, E. U. Saritas, D. Schaffer and S. M. Conolly, *Sci. Rep.*, 2015, **5**, 14055.

27 X. Y. Zhou, K. E. Jeffris, E. Y. Yu, B. Zheng, P. W. Goodwill, P. Nahid and S. M. Conolly, *Phys. Med. Biol.*, 2017, **62**, 3510–3522.

28 G. Song, X. Zheng, Y. Wang, X. Xia, S. Chu and J. Rao, *ACS Nano*, 2019, **13**, 7750–7758.

29 K. P. Melo, A. V. Makela, A. M. Hamilton and P. J. Foster, *bioRxiv*, 2020, DOI: 10.1101/2020.07.12.197780, preprint.

30 A. Tomitaka, S. Ota, K. Nishimoto, H. Arami, Y. Takemura and M. Nair, *Nanoscale*, 2019, **11**, 6489–6496.

31 B. Gleich and R. Weizenecker, *Nature*, 2005, **435**, 1214–1217.

32 P. W. Goodwill and S. M. Conolly, *IEEE Trans. Magn.*, 2011, **30**, 1581–1590.

33 P. W. Goodwill, PhD Thesis, UC Berkeley, 2010.

34 Bruker BioSpin GmbH, https://ir.bruker.com/press-releases/press-release-details/2013/Bruker-Announces-the-Worlds-First-Preclinical-Magnetic-Particle-Imaging-MPI-System/default.aspx, (accessed March 2021).

35 H. Bagheri and M. E. Hayden, *J. Magn. Magn. Mater.*, 2020, **498**, 166021.

36 K. Murase, T. Konishi, Y. Takeuchi, H. Takata and S. Saito, *Radiol. Phys. Technol.*, 2013, **6**, 399–414.

37 K. Murase, S. Hiratsuka, R. X. Song and Y. Takeuchi, *Jpn. J. Appl. Phys.*, 2014, **53**, 067001.

38 J. Rahmer, A. Halkola, B. Gleich, I. Schmale and J. Borgert, *Phys. Med. Biol.*, 2015, **60**, 1775–1791.

39 V. Schulz, M. Straub, M. Mahlke, S. Hubertus, T. Lammers and F. Kiessling, *IEEE Trans. Magn.*, 2015, **51**, 6501804.

40 M. Straub and V. Schulz, *IEEE Trans. Magn.*, 2018, **37**, 1192–1203.

41 J. Borgert, J. D. Schmidt, I. Schmale, C. Bontus, B. Gleich, B. David, J. Weizenecker, J. Jockram, C. Lauruschkat, O. Mende, M. Heinrich, A. Halkola, J. Bergmann, O. Woywode and J. Rahmer, *Biomed. Tech.*, 2013, **58**, 551–556.

42 J. Rahmer, C. Stehning and B. Gleich, *PLoS One*, 2018, **13**, e0193546.

43 C. B. Top, S. Ilbey and H. E. Güven, *Med. Phys.*, 2017, **44**, 6225–6238.

44 E. U. Saritas, P. W. Goodwill, L. R. Croft, J. J. Konkle, K. Lu, B. Zheng and S. M. Conolly, *J. Magn. Reson.*, 2013, **229**, 116–126.

45 B. Zheng, E. Yu, R. Orendorff, K. Lu, J. J. Konkle, Z. W. Tay, D. Hensley, X. Y. Zhou, P. Chandrasekharan, E. U. Saritas, P. W. Goodwill, J. D. Hazle and S. M. Conolly, *Mol. Imaging Biol.*, 2017, **19**, 385–390.

46 P. W. Goodwill, J. J. Konkle, B. Zheng, E. U. Saritas and S. M. Conolly, *IEEE Trans. Med. Imaging*, 2012, **31**, 1076–1085.

47 A. P. Khandhar, R. M. Ferguson, H. Arami and K. M. Krishnan, *Biomaterials*, 2013, **34**, 3837–3845.

48 A. Meola, J. Rao, N. Chaudhary, G. Song, X. Zheng and S. D. Chang, *World Neurosurg.*, 2019, **125**, 261–270.

49 J. Haegele, J. Rahmer, B. Gleich, J. Borgert, H. Wojtczyk, N. Panagiotopoulos, T. M. Buzug, J. Barkhausen and F. M. Vogt, *Radiology*, 2012, **265**, 933–938.

50 J. Weizenecker, B. Gleich, J. Rahmer, H. Dahnke and J. Borgert, *Phys. Med. Biol.*, 2009, **54**, L1–L10.

51 R. M. Ferguson, A. P. Khandhar and K. M. Krishnan, *J. Appl. Phys.*, 2012, **111**, 7B318-317B3185.

52 R. M. Ferguson, K. R. Minard, A. P. Khandhar and K. M. Krishnan, *Med. Phys.*, 2011, **38**, 1619–1626.

53 R. M. Ferguson, K. R. Minard and K. M. Krishnan, *J. Magn. Magn. Mater.*, 2009, **321**, 1548–1551.

54 C. Lu, L. B. Han, J. N. Wang, J. C. Wan, G. S. Song and J. H. Rao, *Chem. Soc. Rev.*, 2021, **50**, 8102–8146.

55 P. W. Goodwill and S. M. Conolly, *IEEE Trans. Med. Imaging*, 2010, **29**, 1851–1859.

56 J. Rahmer, J. Weizenecker, B. Gleich and J. Borgert, *BMC Med. Imaging*, 2009, **9**, 4.

57 T. M. Buzug and J. Borgert, *Magnetic Particle Imaging*, Springer Proceedings in Physics, New York, 2012.

58 E. Y. Yu, P. Chandrasekharan, R. Berzon, Z. W. Tay, X. Y. Zhou, A. P. Khandhar, R. M. Ferguson, S. J. Kemp, B. Zheng, P. W. Goodwill, M. F. Wendland, K. M. Krishnan, S. Behr, J. Carter and S. M. Conolly, *ACS Nano*, 2017, **11**, 12067–12076.

59 P. W. Goodwill, L. R. Croft, J. J. Konkle, K. Lu, E. U. Saritas, B. Zheng and S. M. Conolly, *A 7 T/M 3D X-space MPI mouse and rat scanner*, IEEE, New York, 2013.

60 L. Gutierrez, R. Costo, C. Gruttner, F. Westphal, N. Gehrke, D. Heinke, A. Fornara, Q. A. Pankhurst, C. Johansson, S. Veintemillas-Verdaguer and M. P. Morales, *Dalton Trans.*, 2015, **44**, 2943–2952.

61 J. Wells, N. Lowa, H. Paysen, U. Steinhoff and F. Wiekhorst, *J. Magn. Magn. Mater.*, 2019, **475**, 421–428.

62 L. C. Wu, Y. Zhang, G. Steinberg, H. Qu, S. Huang, M. Cheng, T. Bliss, F. Du, J. Rao, G. Song, L. Pisani, T. Doyle, S. M. Conolly, K. M. Krishnan, G. Grant and M. Wintermark, *Am. J. Neuroradiol.*, 2019, **40**, 206–212.

63 R. M. Ferguson, A. P. Khandhar, S. J. Kemp, H. Arami, E. U. Saritas, L. R. Croft, J. Konkle, P. W. Goodwill, A. Halkola, J. Rahmer, J. Borgert, S. M. Conolly and K. M. Krishnan, *IEEE Trans. Med. Imaging*, 2015, **34**, 1077–1084.

64 B. Gleich, J. Weizenecker and J. Borgert, *Phys. Med. Biol.*, 2008, **53**, N81–N84.

65 J. Weizenecker, J. Borgert and B. Gleich, *Phys. Med. Biol.*, 2007, **52**, 6363–6374.

66 T. F. Sattel, T. Knopp, S. Biederer, B. Gleich, J. Weizenecker, J. Borgert and T. M. Buzug, *J. Phys. D: Appl. Phys.*, 2009, **42**, 022001.

67 T. Knopp, S. Biederer, T. F. Sattel, J. Rahmer, J. Weizenecker, B. Gleich, J. Borgert and T. M. Buzug, *Med. Phys.*, 2010, **37**, 485–491.

68 T. Knopp, T. F. Sattel, S. Biederer, J. Rahmer, J. Weizenecker, B. Gleich, J. Borgert and T. M. Buzug, *IEEE Trans. Med. Imaging*, 2010, **29**, 12–18.

69 T. Knopp, S. Biederer, T. Sattel, J. Weizenecker, B. Gleich, J. Borgert and T. M. Buzug, *Phys. Med. Biol.*, 2009, **54**, 385–397.

70 P. W. Goodwill, K. Lu, B. Zheng and S. M. Conolly, *Rev. Sci. Instrum.*, 2012, **83**, 033708.

71 S. Kurt, Y. Muslu and E. U. Saritas, *IEEE Trans. Med. Imaging*, 2020, **39**, 3441–3450.

72 M. Weber, J. Beuke, A. Gladiss, K. Gräfe, P. Vogel, V. C. Behr and T. M. Buzug, *Int. J. Magn. Part. Imaging*, 2018, **4**, 1811004.

73 E. Yagiza, A. R. Cagila and E. U. Saritasa, *Int. J. Magn. Part. Imaging*, 2020, **6**, 2006001.

74 M. Erbe, T. Knopp, T. F. Sattel, S. Biederer and T. M. Buzug, *Med. Phys.*, 2011, **38**, 5200–5207.

75 K. Nomura, K. Yamauchi, T. Matsuda, S. Tonooka, K. Yoshida, Y. Susumu, Y. Okada and S. Sato, presented in part of World Molecular Imaging Congress (WMIC), Virtual, October 2020.

76 J. Weizenecker, B. Gleich and J. Borgert, *J. Phys. D: Appl. Phys.*, 2008, **41**, 105009.

77 M. H. Pablico-Lansigan, S. F. Situ and A. C. Samia, *Nanoscale*, 2013, **5**, 4040–4055.

78 T. Knopp, M. Erbe, T. F. Sattel, S. Biederer and T. M. Buzug, *Appl. Phys. Lett.*, 2010, **97**, 092505.

79 C. B. Top and A. Gungor, *IEEE Trans. Med. Imaging*, 2020, **39**, 4164–4173.

80 A. C. Bakenecker, M. Ahlborg, C. Debbeler, C. Kaethner, T. M. Buzug and K. Ludtke-Buzug, *Innovative Surg. Sci.*, 2018, **3**, 179–192.

81 J. Guzy, S. Chakravarty, F. J. Buchanan, H. Chen, J. M. Gaudet, J. M. L. Hix, C. L. Mallett and E. M. Shapiro, *ACS Appl. Nano Mater.*, 2020, **3**, 3991–3999.

82 P. Chandrasekharan, Z. W. Tay, X. Y. Zhou, E. Yu, R. Orendorff, D. Hensley, Q. Huynh, K. L. B. Fung, C. C. VanHook, P. Goodwill, B. Zheng and S. Conolly, *Br. J. Radiol.*, 2018, **91**, 20180326.

83 R. E. Rosensweig, *J. Magn. Magn. Mater.*, 2002, **252**, 370–374.

84 R. J. Deissler, Y. Wu and M. A. Martens, *Med. Phys.*, 2014, **41**, 012301.

85 P. W. Goodwill, A. Tamrazian, L. R. Croft, C. D. Lu, E. M. Johnson, R. Pidaparthi, R. M. Ferguson, A. P. Khandhar, K. M. Krishnan and S. M. Conolly, *Appl. Phys. Lett.*, 2011, **98**, 262502.

86 K. M. Krishnan, *IEEE Trans. Magn.*, 2010, **46**, 2523–2558.

87 G. Hong, A. L. Antaris and H. Dai, *Nat. Biomed. Eng.*, 2017, **1**, 0010.

88 H. Hong, Y. Yang, Y. Zhang and W. Cai, *Curr. Top. Med. Chem.*, 2010, **10**, 1237–1248.

89 E. T. Ahrens and J. W. Bulte, *Nat. Rev. Immunol.*, 2013, **13**, 755–763.

90 W. Cai, G. Niu and X. Chen, *Curr. Pharm. Des.*, 2008, **14**, 2943–2973.

91 T. F. Massoud and S. S. Gambhir, *Genes Dev.*, 2003, **17**, 545–580.

92 E. Y. Yu, M. Bishop, B. Zheng, R. M. Ferguson, A. P. Khandhar, S. J. Kemp, K. M. Krishnan,

P. W. Goodwill and S. M. Conolly, *Nano Lett.*, 2017, **17**, 1648–1654.

93   N. Panagiotopoulos, R. L. Duschka, M. Ahlborg, G. Bringout, C. Debbeler, M. Graeser, C. Kaethner, K. Lüdtke-Buzug, H. Medimagh, J. Stelzner, T. M. Buzug, J. Barkhausen, F. M. Vogt and J. Haegele, *Int. J. Nanomed.*, 2015, **10**, 3097–3114.

94   R. Hachani, M. Lowdell, M. Birchall and N. T. Thanh, *Nanoscale*, 2013, **5**, 11362–11373.

95   Q. A. Pankhurst, N. K. T. Thanh, S. K. Jones and J. Dobson, *J. Phys. D: Appl. Phys.*, 2009, **42**, 224001.

96   A. R. Kherlopian, T. Song, Q. Duan, M. A. Neimark, M. J. Po, J. K. Gohagan and A. F. Laine, *BMC Syst. Biol.*, 2008, **2**, 74.

97   N. Talebloo, M. Gudi, N. Robertson and P. Wang, *J. Magn. Reson. Imaging*, 2020, **51**, 1659–1668.

98   J. F. Schenck, *Med. Phys.*, 1996, **23**, 815–850.

99   J. W. M. Bulte, P. Walczak, B. Gleich, J. Weizenecker, D. E. Markov, H. C. J. Aerts, H. Boeve, J. Borgert and M. Kuhne, *Proc. SPIE-Int. Soc. Opt. Eng.*, 2011, **7965**, 79650z.

100   E. B. Ehlerding, P. Grodzinski, W. B. Cai and C. H. Liu, *ACS Nano*, 2018, **12**, 2106–2121.

101   G. Kandasamy and D. Maity, *Mater. Sci. Eng., C*, 2021, **127**, 112199.

102   Y. X. Wang, *Quant. Imaging Med. Surg.*, 2011, **1**, 35–40.

103   A. B. Nayak, A. Luhar, M. Hanudel, B. Gales, T. R. Hall, J. P. Finn, I. B. Salusky and J. Zaritsky, *Pediatr. Nephrol.*, 2015, **30**, 515–521.

104   R. A. Revia and M. Q. Zhang, *Mater. Today*, 2016, **19**, 157–168.

105   E. A. Neuwelt, B. E. Hamilton, C. G. Varallyay, W. R. Rooney, R. D. Edelman, P. M. Jacobs and S. G. Watnick, *Kidney Int.*, 2009, **75**, 465–474.

106   S. Caspani, R. Magalhaes, J. P. Araujo and C. T. Sousa, *Materials*, 2020, **13**, 2586.

107   S. M. Dadfar, K. Roemhild, N. I. Drude, S. von Stillfried, R. Knuchel, F. Kiessling and T. Lammers, *Adv. Drug Delivery Rev.*, 2019, **138**, 302–325.

108   J. W. Bulte, J. Vymazal, R. A. Brooks, C. Pierpaoli and J. A. Frank, *J. Magn. Reson. Imaging*, 1993, **3**, 641–648.

109   J. W. Bulte, *AJR, Am. J. Roentgenol.*, 2009, **193**, 314–325.

110   Y. Wang, C. Xu, Y. Chang, L. Zhao, K. Zhang, Y. Zhao, F. Gao and X. Gao, *ACS Appl. Mater. Interfaces*, 2017, **9**, 28959–28966.

111   W. C. Xiao, P. Legros, P. Chevallier, J. Lagueux, J. K. Oh and M. A. Fortin, *ACS Appl. Nano Mater.*, 2018, **1**, 894–907.

112   H. Groult, N. Poupard, F. Herranz, E. Conforto, N. Bridiau, F. Sannier, S. Bordenave, J. M. Piot, J. Ruiz-Cabello, I. Fruitier-Arnaudin and T. Maugard, *Biomacromolecules*, 2017, **18**, 3156–3167.

113   S. Magnitsky, J. Zhang, D. Idiyatullin, G. Mohan, M. Garwood, N. E. Lane and S. Majumdar, *Magn. Reson. Med.*, 2017, **78**, 1900–1910.

114   J. Zhang, H. L. Ring, K. R. Hurley, Q. Shao, C. S. Carlson, D. Idiyatullin, N. Manuchehrabadi, P. J. Hoopes, C. L. Haynes, J. C. Bischof and M. Garwood, *Magn. Reson. Med.*, 2017, **78**, 702–712.

115   J. Pellico, J. Ruiz-Cabello, I. Fernandez-Barahona, L. Gutierrez, A. V. Lechuga-Vieco, J. A. Enriquez, M. P. Morales and F. Herranz, *Langmuir*, 2017, **33**, 10239–10247.

116   L. Sandiford, A. Phinikaridou, A. Protti, L. K. Meszaros, X. Cui, Y. Yan, G. Frodsham, P. A. Williamson, N. Gaddum, R. M. Botnar, P. J. Blower, M. A. Green and R. T. de Rosales, *ACS Nano*, 2013, **7**, 500–512.

117   F. Hu, Q. Jia, Y. Li and M. Gao, *Nanotechnology*, 2011, **22**, 245604.

118   M. Jeon, M. V. Halbert, Z. R. Stephen and M. Q. Zhang, *Adv. Mater.*, 2021, **33**, 1906539.

119   Z. J. Zhou, Z. H. Zhao, H. Zhang, Z. Y. Wang, X. Y. Chen, R. F. Wang, Z. Chen and J. H. Gao, *ACS Nano*, 2014, **8**, 7976–7985.

120   M. O. Besenhard, L. Panariello, C. Kiefer, A. P. LaGrow, L. Storozhuk, F. Perton, S. Begin, D. Damien Mertz, N. T. K. Thanh and A. Gavriilidis, *Nanoscale*, 2021, **13**, 8795–8805.

121   M. S. Judenhofer, H. F. Wehrl, D. F. Newport, C. Catana, S. B. Siegel, M. Becker, A. Thielscher, M. Kneilling, M. P. Lichy, M. Eichner, K. Klingel, G. Reischl, S. Widmaier, M. Rocken, R. E. Nutt, H. J. Machulla, K. Uludag, S. R. Cherry, C. D. Claussen and B. J. Pichler, *Nat. Med.*, 2008, **14**, 459–465.

122   J. Franke, U. Heinen, H. Lehr, A. Weber, F. Jaspard, W. Ruhm, M. Heidenreich and V. Schulz, *IEEE Trans. Med. Imaging*, 2016, **35**, 1993–2004.

123   P. Vogel, S. Lother, M. A. Ruckert, W. H. Kullmann, P. M. Jakob, F. Fidler and V. C. Behr, *IEEE Trans. Med. Imaging*, 2014, **33**, 1954–1959.

124   M. G. Kaul, O. Weber, U. Heinen, A. Reitmeier, T. Mummert, C. Jung, N. Raabe, T. Knopp, H. Ittrich and G. Adam, *RöFo*, 2015, **187**, 347–352.

125   J. Salamon, M. Hofmann, C. Jung, M. G. Kaul, F. Werner, K. Them, R. Reimer, P. Nielsen, A. Vom Scheidt, G. Adam, T. Knopp and H. Ittrich, *PLoS One*, 2016, **11**, e0156899.

126   J. Franke, U. Heinen, L. Matthies, V. Niemann, F. Jaspard, M. Heidenreich and T. M. Buzug, *First hybrid MPI-MRI imaging system as integrated design for mice and rats: Description of the instrumentation setup*, IEEE, New York, 2013.

127   J. Franke, U. Heinen, H. Lehr, A. Weber, F. Jaspard, W. Ruhm, M. Heidenreich and V. Schulz, *First 3D dual modality phantom measurements of a hybrid MPI-MRI system using a resistive 12 channel MPI-MRI magnet design*, IEEE, New York, 2015.

128   J. Franke, N. Baxan, H. Lehr, U. Heinen, S. Reinartz, J. Schnorr, M. Heidenreich, F. Kiessling and V. Schulz, *IEEE Trans. Med. Imaging*, 2020, **39**, 4335–4345.

129   T. C. Kwee, R. M. Kwee and R. A. Nievelstein, *Blood*, 2008, **111**, 504–516.

130   D. Lardinois, W. Weder, T. F. Hany, E. M. Kamel, S. Korom, B. Seifert, G. K. von Schulthess and H. C. Steinert, *N. Engl. J. Med.*, 2003, **348**, 2500–2507.

131   S. Monti, C. Cavaliere, M. Covello, E. Nicolai, M. Salvatore and M. Aiello, *J. Healthcare Eng.*, 2017, **2017**, 2634389.

132 P. Vogel, J. Markert, M. A. Ruckert, S. Herz, B. Kessler, K. Dremel, D. Althoff, M. Weber, T. M. Buzug, T. A. Bley, W. H. Kullmann, R. Hanke, S. Zabler and V. C. Behr, *Sci. Rep.*, 2019, **9**, 12627.

133 P. Goodwill, K. M. Krishnan and S. M. Conolly, in *Magnetic Nanoparticles: From Fabrication to Clinical Applications*, ed. N. T. K. Thanh, Taylor & Francis, Oxfordshire, 1st edn, 2012, vol. 20, pp. 523–541.

134 X. Y. Zhou, Z. W. Tay, P. Chandrasekharan, E. Y. Yu, D. W. Hensley, R. Orendorff, K. E. Jeffris, D. Mai, B. Zheng, P. W. Goodwill and S. M. Conolly, *Curr. Opin. Chem. Biol.*, 2018, **45**, 131–138.

135 A. K. Gupta, R. R. Naregalkar, V. D. Vaidya and M. Gupta, *Nanomedicine*, 2007, **2**, 23–39.

136 H. Ittrich, K. Peldschus, N. Raabe, M. Kaul and G. Adam, *RöFo*, 2013, **185**, 1149–1166.

137 M. H. Schwenk, *Pharmacotherapy*, 2010, **30**, 70–79.

138 S. S. Vasanawala, K. L. Nguyen, M. D. Hope, M. D. Bridges, T. A. Hope, S. B. Reeder and M. R. Bashir, *Magn. Reson. Med.*, 2016, **75**, 2107–2111.

139 J. He, M. Huang, D. Wang, Z. Zhang and G. Li, *J. Pharm. Biomed. Anal.*, 2014, **101**, 84–101.

140 D. W. Inglis, R. Riehn, R. H. Austin and J. C. Sturm, *Appl. Phys. Lett.*, 2004, 5093.

141 K. Hola, Z. Markova, G. Zoppellaro, J. Tucek and R. Zboril, *Biotechnol. Adv.*, 2015, **33**, 1162–1176.

142 L. Wang, A. Hervault, P. Southern, O. Sandre, F. Couillaud and N. T. K. Thanh, *J. Mater. Chem. B*, 2020, **8**, 10527–10539.

143 L. Wu, Y. Cao, C. Liao, J. Huang and F. Gao, *Eur. J. Radiol.*, 2011, **80**, 582–589.

144 J. J. Pouw, M. R. Grootendorst, R. Bezooijen, C. A. Klazen, W. I. De Bruin, J. M. Klaase, M. A. Hall-Craggs, M. Douek and B. Ten Haken, *Br. J. Radiol.*, 2015, **88**, 20150634.

145 S. Namkung, C. J. Zech, T. Helmberger, M. F. Reiser and S. O. Schoenberg, *J. Magn. Reson. Imaging*, 2007, **25**, 755–765.

146 S. Tokunaga, M. Koda, T. Matono, T. Sugihara, T. Nagahara, M. Ueki, Y. Murawaki, S. Kakite and E. Yamashita, *Br. J. Radiol.*, 2012, **85**, 745–752.

147 N. Ruangwattanapaisarn, A. Hsiao and S. S. Vasanawala, *Pediatr. Radiol.*, 2015, **45**, 831–839.

148 B. Bonnemain, *J. Drug Targeting*, 1998, **6**, 167–174.

149 R. Jin, B. Lin, D. Li and H. Ai, *Curr. Opin. Pharmacol.*, 2014, **18**, 18–27.

150 M. Lu, M. H. Cohen, D. Rieves and R. Pazdur, *Am. J. Hematol.*, 2010, **85**, 315–319.

151 P. Reimer and T. Balzer, *Eur. Radiol.*, 2003, **13**, 1266–1276.

152 C. Sun, J. S. Lee and M. Zhang, *Adv. Drug Delivery Rev.*, 2008, **60**, 1252–1265.

153 Y. X. Wang, S. M. Hussain and G. P. Krestin, *Eur. Radiol.*, 2001, **11**, 2319–2331.

154 J. Weizenecker, B. Gleich, J. Rahmer and J. Borgert, *Phys. Med. Biol.*, 2012, **57**, 7317–7327.

155 J. P. Bullivant, S. Zhao, B. J. Willenberg, B. Kozissnik, C. D. Batich and J. Dobson, *Int. J. Mol. Sci.*, 2013, **14**, 17501–17510.

156 J. Lodhia, G. Mandarano, N. J. Ferris, P. Eu and S. F. Cowell, *Biomed. Imaging Intervention J.*, 2010, **6**, e12.

157 F. Ludwig, T. Wawrzik, T. Yoshida, N. Gehrke, A. Briel, D. Eberbeck and M. Schilling, *IEEE Trans. Magn.*, 2012, **48**, 3780–3783.

158 Z. W. Tay, P. Chandrasekharan, X. Y. Zhou, E. Yu, B. Zheng and S. Conolly, *Theranostics*, 2018, **8**, 3676–3687.

159 Z. W. Tay, D. W. Hensley, E. C. Vreeland, B. Zheng and S. M. Conolly, *Biomed. Phys. Eng. Express*, 2017, **3**, 035003.

160 P. Bender, J. Fock, C. Frandsen, M. F. Hansen, C. Balceris, F. Ludwig, O. Posth, E. Wetterskog, L. K. Bogart, P. Southern, W. Szczerba, L. Zeng, K. Witte, C. Grüttner, F. Westphal, D. Honecker, D. Gonzalez-Alonso, L. F. Barquín and C. Johansson, *J. Phys. Chem. C*, 2018, **122**, 3068–3077.

161 K. Ludtke-Buzug, J. Haegele, S. Biederer, T. F. Sattel, M. Erbe, R. L. Duschka, J. Barkhausen and F. M. Vogt, *Biomed. Tech.*, 2013, **58**, 527–533.

162 H. Kratz, M. Taupitz, A. Ariza de Schellenberger, O. Kosch, D. Eberbeck, S. Wagner, L. Trahms, B. Hamm and J. Schnorr, *PLoS One*, 2018, **13**, e0190214.

163 D. Eberbeck, C. L. Dennis, N. F. Huls, K. L. Krycka, C. Grüttner and F. Westphal, *IEEE Trans. Magn.*, 2013, **49**, 269–274.

164 C. Jonasson, V. Schaller, L. J. Zeng, E. Olsson, C. Frandsen, A. Castro, L. Nilsson, L. K. Bogart, P. Southern, Q. A. Pankhurst, M. P. Morales and C. Johansson, *J. Magn. Magn. Mater.*, 2019, **477**, 198–202.

165 M. Wetegrove, K. Witte, W. Bodnar, D. E. Pfahl, A. Springer, N. Schell, F. Westphal and E. Burkel, *CrystEngComm*, 2019, **21**, 1956–1966.

166 K. Riahi, M. M. van de Loosdrecht, L. Alic and B. ten Haken, *J. Magn. Magn. Mater.*, 2020, **514**, 167238.

167 R. Dhavalikar, D. Hensley, L. Maldonado-Camargo, L. R. Croft, S. Ceron, P. W. Goodwill, S. M. Conolly and C. Rinaldi, *J. Phys. D: Appl. Phys.*, 2016, **49**, 305002.

168 A. P. Khandhar, R. M. Ferguson, H. Arami, S. J. Kemp and K. M. Krishnan, *IEEE Trans. Magn.*, 2015, **51**, 5300304.

169 R. Orendorff, A. J. Peck, B. Zheng, S. N. Shirazi, R. Matthew Ferguson, A. P. Khandhar, S. J. Kemp, P. Goodwill, K. M. Krishnan, G. A. Brooks, D. Kaufer and S. Conolly, *Phys. Med. Biol.*, 2017, **62**, 3501–3509.

170 P. Ludewig, N. Gdaniec, J. Sedlacik, N. D. Forkert, P. Szwargulski, M. Graeser, G. Adam, M. G. Kaul, K. M. Krishnan, R. M. Ferguson, A. P. Khandhar, P. Walczak, J. Fiehler, G. Thomalla, C. Gerloff, T. Knopp and T. Magnus, *ACS Nano*, 2017, **11**, 10480–10488.

171 I. Hilger and W. A. Kaiser, *Nanomedicine*, 2012, 7, 1443–1459.

172 L. Storozhuk, M. O. Besenhard, S. Mourdikoudis, A. P. LaGrow, M. R. Lees, L. Tung, A. Gavriilidis and N. T. K. Thanh, *ACS Appl. Mater. Interfaces*, 2021, **13**, 45870–45880.

173 S. Dutz, M. Kettering, I. Hilger, R. Muller and M. Zeisberger, *Nanotechnology*, 2011, **22**, 265102.

174 S. Dutz, J. H. Clement, D. Eberbeck, T. Gelbrich, R. Hergt, R. Muller, J. Wotschadlo and M. Zeisberger, *J. Magn. Magn. Mater.*, 2009, **321**, 1501–1504.

175 G. Hemery, C. Genevois, F. Couillaud, S. Lacomme, E. Gontier, E. Ibarboure, S. Lecommandoux, E. Garanger and O. Sandre, *Mol. Syst. Des. Eng.*, 2017, **2**, 629–639.

176 C. Blanco-Andujar, D. Ortega, P. Southern, Q. A. Pankhurst and N. T. K. Thanh, *Nanoscale*, 2015, **7**, 1768–1775.

177 T. Kuboyabu, M. Yamawaki, M. Aoki, A. Ohki and K. Murase, *Int. J. Nanomed. Nanosurg.*, 2016, **2**, 1–7.

178 E. Myrovali, N. Maniotis, T. Samaras and M. Angelakeris, *Nanoscale Adv.*, 2020, **2**, 408–416.

179 Z. W. Tay, P. Chandrasekharan, A. Chiu-Lam, D. W. Hensley, R. Dhavalikar, X. Y. Zhou, E. Y. Yu, P. W. Goodwill, B. Zheng, C. Rinaldi and S. M. Conolly, *ACS Nano*, 2018, **12**, 3699–3713.

180 N. C. V. Rost, K. Sen, S. Savliwala, I. Singh, S. Liu, M. Unni, L. Raniero and C. Rinaldi, *J. Magn. Magn. Mater.*, 2020, **504**, 166675.

181 L. H. Wu, A. Mendoza-Garcia, Q. Li and S. H. Sun, *Chem. Rev.*, 2016, **116**, 10473–10512.

182 D. L. LesliePelecky and R. D. Rieke, *Chem. Mater.*, 1996, **8**, 1770–1783.

183 R. M. Ferguson, A. P. Khandhar, H. Arami, L. Hua, O. Hovorka and K. M. Krishnan, *Biomed. Eng.-Biomed. Tech.*, 2013, **58**, 493–507.

184 W. Xie, Z. Guo, F. Gao, Q. Gao, D. Wang, B. S. Liaw, Q. Cai, X. Sun, X. Wang and L. Zhao, *Theranostics*, 2018, **8**, 3284–3307.

185 P. Guardia, R. Di Corato, L. Lartigue, C. Wilhelm, A. Espinosa, M. Garcia-Hernandez, F. Gazeau, L. Manna and T. Pellegrino, *ACS Nano*, 2012, **6**, 3080–3091.

186 S. Behzadi, V. Serpooshan, W. Tao, M. A. Hamaly, M. Y. Alkawareek, E. C. Dreaden, D. Brown, A. M. Alkilany, O. C. Farokhzad and M. Mahmoudi, *Chem. Soc. Rev.*, 2017, **46**, 4218–4244.

187 H. L. Ye, Z. Q. Shen, L. Yu, M. Wei and Y. Li, *Proc. R. Soc. A*, 2018, **474**, 20170845.

188 S. Ziemian, N. Lowa, O. Kosch, D. Bajj, F. Wiekhorst and G. Schutz, *Nanomaterials*, 2018, **8**, 180.

189 S. H. Noh, W. Na, J. T. Jang, J. H. Lee, E. J. Lee, S. H. Moon, Y. Lim, J. S. Shin and J. Cheon, *Nano Lett.*, 2012, **12**, 3716–3721.

190 L. M. Bauer, S. F. Situ, M. A. Griswold and A. C. Samia, *Nanoscale*, 2016, **8**, 12162–12169.

191 A. Lak, M. Cassani, B. T. Mai, N. Winckelmans, D. Cabrera, E. Sadrollahi, S. Marras, H. Remmer, S. Fiorito, L. Cremades-Jimeno, F. J. Litterst, F. Ludwig, L. Manna, F. J. Teran, S. Bals and T. Pellegrino, *Nano Lett.*, 2018, **18**, 6856–6866.

192 D. Niculaes, A. Lak, G. C. Anyfantis, S. Marras, O. Laslett, S. K. Avugadda, M. Cassani, D. Serantes, O. Hovorka, R. Chantrell and T. Pellegrino, *ACS Nano*, 2017, **11**, 12121–12133.

193 T. Knopp, N. Gdaniec and M. Moddel, *Phys. Med. Biol.*, 2017, **62**, R124–R178.

194 S. F. Hasany, I. Ahmed, J. Rajan and A. Rehman, *Nanosci. Nanotechnol.*, 2012, **2**, 148–158.

195 J. K. Oh and J. M. Park, *Prog. Polym. Sci.*, 2011, **36**, 168–189.

196 M. L. Mojica Pisciotti, E. Lima Jr., M. Vasquez Mansilla, V. E. Tognoli, H. E. Troiani, A. A. Pasa, T. B. Creczynski-Pasa, A. H. Silva, P. Gurman, L. Colombo, G. F. Goya, A. Lamagna and R. D. Zysler, *J. Biomed. Mater. Res., Part B*, 2014, **102**, 860–868.

197 M. Yu, S. Huang, K. J. Yu and A. M. Clyne, *Int. J. Mol. Sci.*, 2012, **13**, 5554–5570.

198 P. Keselman, E. Y. Yu, X. Y. Zhou, P. W. Goodwill, P. Chandrasekharan, R. M. Ferguson, A. P. Khandhar, S. J. Kemp, K. M. Krishnan, B. Zheng and S. M. Conolly, *Phys. Med. Biol.*, 2017, **62**, 3440–3453.

199 A. Tomitaka, H. Arami, S. Gandhi and K. M. Krishnan, *Nanoscale*, 2015, **7**, 16890–16898.

200 M. P. Morales, O. Bomati-Miguel, R. P. de Alejo, J. Ruiz-Cabello, S. Veintemillas-Verdaguer and K. O'Grady, *J. Magn. Magn. Mater.*, 2003, **266**, 102–109.

201 S. H. Chaki, T. J. Malek, M. D. Chaudhary, J. P. Tailor and M. P. Deshpande, *Adv. Nat. Sci.: Nanosci. Nanotechnol.*, 2015, **6**, 035009.

202 A. Ali, H. Zafar, M. Zia, I. Ul Haq, A. R. Phull, J. S. Ali and A. Hussain, *Nanotechnol., Sci. Appl.*, 2016, **9**, 49–67.

203 H. Kratz, D. Eberbeck, S. Wagner, M. Taupitz and J. Schnorr, *Biomed. Eng.-Biomed. Tech.*, 2013, **58**, 509–515.

204 M. C. Mascolo, Y. B. Pei and T. A. Ring, *Materials*, 2013, **6**, 5549–5567.

205 M. O. Besenhard, A. P. LaGrow, A. Hodzic, M. Kriechbaum, L. Panariello, G. Bais, K. Loizou, S. Damilos, M. M. Cruz, N. T. K. Thanh and A. Gavriilidis, *Chem. Eng. J.*, 2020, **399**, 125740.

206 H. Kratz, A. Mohtashamdolatshahi, D. Eberbeck, O. Kosch, R. Hauptmann, F. Wiekhorst, M. Taupitz, B. Hamm and J. Schnorr, *Nanomaterials*, 2019, **9**, 1466.

207 W. Wu, Z. H. Wu, T. Yu, C. Z. Jiang and W. S. Kim, *Sci. Technol. Adv. Mater.*, 2015, **16**, 023501.

208 C. Kim, J. Lee, D. Schmucker and J. D. Fortner, *npj Clean Water*, 2020, **3**, 8.

209 R. Hufschmid, H. Arami, R. M. Ferguson, M. Gonzales, E. Teeman, L. N. Brush, N. D. Browning and K. M. Krishnan, *Nanoscale*, 2015, **7**, 11142–11154.

210 N. T. K. Thanh, I. Robinson and T. L. D. Dekker, *Encycl. Nanosci. Nanotechnol.*, 2007, **1**, 1–10.

211 C. Blanco-Andujar, L. D. Tung and N. T. K. Thanh, *Annu. Rep. Prog. Chem., Sect. A: Inorg. Chem.*, 2010, **106**, 553–568.

212 M. H. M. Dias and P. C. Lauterbur, *Magn. Reson. Med.*, 1986, **3**, 328–330.

213 S. Hildebrand, N. Löwa, H. Paysen, R. M. Fratila, L. Reverte-Salisa, T. Trakoolwilaiwan, Z. Niu, G. Kasparis, S. F. Preuss, O. Kosch, J. M. de la Fuente, N. T. K. Thanh, F. Wiekhorst and A. Pfeifer, *ACS Nano*, 2021, **15**, 434–446.

214 V. Herynek, M. Babic, O. Kaman, H. Charvatova, M. Vesela, O. Buchholz, M. Vosmanska, D. Kubaniova, J. Kohout, U. G. Hofmann and L. Sefc, *J. Nanopart. Res.*, 2021, **23**, 52.

215 Z. Jiang, X. Han, Y. Du, Y. Li, Y. Li, J. Li, J. Tian and A. Wu, *Nano Lett.*, 2021, **21**, 2730–2737.

216 A. Baki, A. Remmo, N. Lowa, F. Wiekhorst and R. Bleul, *Int. J. Mol. Sci.*, 2021, **22**, 6235.

217 J. Haegele, R. L. Duschka, M. Graeser, C. Schaecke, N. Panagiotopoulos, K. Ludtke-Buzug, T. M. Buzug, J. Barkhausen and F. M. Vogt, *Int. J. Nanomed.*, 2014, **9**, 4203–4209.

218 A. P. Khandhar, P. Keselman, S. J. Kemp, R. M. Ferguson, P. W. Goodwill, S. M. Conolly and K. M. Krishnan, *Nanoscale*, 2017, **9**, 1299–1306.

219 H. Kratz, A. Mohtashamdolatshahi, D. Eberbeck, O. Kosch, F. Wiekhorst, M. Taupitz, B. Hamm, N. Stolzenburg and J. Schnorr, *Nanomaterials*, 2021, **11**, 1532.

220 A. H. Lu, E. L. Salabas and F. Schuth, *Angew. Chem., Int. Ed.*, 2007, **46**, 1222–1244.

221 Y. Takeuchi, H. Suzuki, H. Sasahara, J. Ueda, I. Yabata, K. Itagaki, S. Saito and K. Murase, *Adv. Biomed. Eng.*, 2014, **4**, 37–43.

222 A. Antonelli, C. Sfara, L. Mosca, E. Manuali and M. Magnani, *J. Nanosci. Nanotechnol.*, 2008, **8**, 2270–2278.

223 D. E. Markov, H. Boeve, B. Gleich, J. Borgert, A. Antonelli, C. Sfara and M. Magnani, *Phys. Med. Biol.*, 2010, **55**, 6461.

224 J. Rahmer, A. Antonelli, C. Sfara, B. Tiemann, B. Gleich, M. Magnani, J. Weizenecker and J. Borgert, *Phys. Med. Biol.*, 2013, **58**, 3965–3977.

225 A. Antonelli, P. Szwargulski, E. Scarpa, F. Thieben, G. Cordula, G. Ambrosi, L. Guidi, P. Ludewig, T. Knopp and M. Magnani, *Nanomedicine*, 2020, **15**, 739–753.

226 A. Tomitaka, H. Arami, Z. Huang, A. Raymond, E. Rodriguez, Y. Cai, M. Febo, Y. Takemura and M. Nair, *Nanoscale*, 2017, **10**, 184–194.

227 World Health Organization, https://gco.iarc.fr/today/fact-sheets-cancers, (accessed May 2021).

228 W. Tong, H. Hui, W. Shang, Y. Zhang, F. Tian, Q. Ma, X. Yang, J. Tian and Y. Chen, *Theranostics*, 2021, **11**, 506–521.

229 Z. W. Tay, presented in part of World Molecular Imaging Congress (WMIC), Montreal, September 2019.

230 Z. W. Tay, D. W. Hensley, P. Chandrasekharan, B. Zheng and S. M. Conolly, *IEEE Trans. Med. Imaging*, 2020, **39**, 1724–1734.

231 K. P. Melo, A. V. Makela, N. N. Knier, A. M. Hamilton and P. J. Foster, *Magnetic Resonance in Medicine*, 2021.

232 T. Knopp, S. Biederer, T. F. Sattel, M. Erbe and T. M. Buzug, *IEEE Trans. Med. Imaging*, 2011, **30**, 1284–1292.

233 M. Graeser, T. Knopp, P. Szwargulski, T. Friedrich, A. von Gladiss, M. Kaul, K. M. Krishnan, H. Ittrich, G. Adam and T. M. Buzug, *Sci. Rep.*, 2017, **7**, 6872.

234 H. Paysen, O. Kosch, J. Wells, N. Loewa and F. Wiekhorst, *Phys. Med. Biol.*, 2020, **65**, 235031.

235 P. W. Goodwill, E. U. Saritas, L. R. Croft, T. N. Kim, K. M. Krishnan, D. V. Schaffer and S. M. Conolly, *Adv. Mater.*, 2012, **24**, 3870–3877.

236 R. Dhavalikar and C. Rinaldi, *J. Appl. Phys.*, 2014, **115**, 074308.

237 C. Shasha, E. Teeman and K. M. Krishnan, *Biomed. Phys. Eng. Express*, 2019, **5**, 055010.

238 J. J. Gevaert, N. D. Calvert, O. C. Sehl, K. P. Melo, A. J. Shuhendler and P. J. Foster, presented in part of World Molecular Imaging Congress (WMIC), Virtual, October 2020.

239 Z. W. Tay, PhD Thesis, UC Berkeley, 2018.

240 C. Colson, Z. W. Tay, K. L. B. Fung, D. W. Hensley, S. Savliwala, B. D. Fellows, X. Y. Zhou, Y. Lu, P. Chandrasekharan, C. Rinaldi and S. M. Conolly, presented in part of World Molecular Imaging Congress (WMIC), Virtual, October 2020.

241 C. Saayujya, presented in part of World Molecular Imaging Congress (WMIC), Virtual, October 2020.

242 Z. Zhao and C. Rinaldi, *Phys. Med. Biol.*, 2020, **65**, 185013.

243 S. Arsalani, N. Lowa, O. Kosch, P. Radon, O. Baffa and F. Wiekhorst, *Phys. Med. Biol.*, 2021, **66**, 015002.

244 S. M. Dadfar, D. Camozzi, M. Darguzyte, K. Roemhild, P. Varvarà, J. Metselaar, S. Banala, M. Straub, N. Güvener, U. Engelmann, I. Slabu, M. Buhl, J. Leusen, P. Kögerler, B. Hermanns-Sachweh, V. Schulz, F. Kiessling and T. Lammers, *J. Nanobiotechnol.*, 2020, **18**, 22.

245 S. Horvat, P. Vogel, T. Kampf, A. Brandl, A. Alshamsan, H. A. Alhadlaq, M. Ahamed, K. Albrecht, V. C. Behr, A. Beilhack and J. Groll, *ChemNanoMat*, 2020, **6**, 755–758.

246 A. J. McGrath, S. Cheong, A. M. Henning, J. J. Gooding and R. D. Tilley, *Chem. Commun.*, 2017, **53**, 11548–11551.

247 T. J. Yoon, H. Lee, H. L. Shao and R. Weissleder, *Angew. Chem., Int. Ed.*, 2011, **50**, 4663–4666.

248 W. S. Seo, J. H. Lee, X. M. Sun, Y. Suzuki, D. Mann, Z. Liu, M. Terashima, P. C. Yang, M. V. McConnell, D. G. Nishimura and H. J. Dai, *Nat. Mater.*, 2006, **5**, 971–976.

249 J. M. Liu, K. Wu and J. P. Wang, *AIP Adv.*, 2016, **6**, 056126.

250 Y. L. Hou, H. Kondoh, T. Kogure and T. Ohta, *Chem. Mater.*, 2004, **16**, 5149–5152.

251 J. Yu, C. Yang, J. D. S. Li, Y. C. Ding, L. Zhang, M. Z. Yousaf, J. Lin, R. Pang, L. B. Wei, L. L. Xu, F. G. Sheng, C. H. Li, G. J. Li, L. Y. Zhao and Y. L. Hou, *Adv. Mater.*, 2014, **26**, 4114–4120.

252 J. H. Gao, G. L. Liang, J. S. Cheung, Y. Pan, Y. Kuang, F. Zhao, B. Zhang, X. X. Zhang, E. X. Wu and B. Xu, *J. Am. Chem. Soc.*, 2008, **130**, 11828–11833.

253 A. Rivera-Rodriguez and C. M. Rinaldi-Ramos, *Annu. Rev. Chem. Biomol. Eng.*, 2021, **12**, 163–185.

254 S. B. Goldhaber, *Regul. Toxicol. Pharmacol.*, 2003, **38**, 232–242.

255 M. Irfan, N. Dogan, A. Bingolbali and F. Aliew, *J. Magn. Magn. Mater.*, 2021, **537**, 168150.

256 J. W. Bulte, M. W. De Jonge, R. L. Kamman, K. G. Go, F. Zuiderveen, B. Blaauw, J. A. Oosterbaan, T. H. The and L. de Leij, *Magn. Reson. Med.*, 1992, **23**, 215–223.

257 J. W. Bulte, L. D. Ma, R. L. Magin, R. L. Kamman, C. E. Hulstaert, K. G. Go, T. H. The and L. de Leij, *Magn. Reson. Med.*, 1993, **29**, 32–37.

258 T. C. Yeh, W. Zhang, S. T. Ildstad and C. Ho, *Magn. Reson. Med.*, 1993, **30**, 617–625.

259 P. K. Nguyen, J. Riegler and J. C. Wu, *Cell Stem Cell*, 2014, **14**, 431–444.

260 E. M. Shapiro, K. Sharer, S. Skrtic and A. P. Koretsky, *Magn. Reson. Med.*, 2006, **55**, 242–249.

261 C. Heyn, J. A. Ronald, S. S. Ramadan, J. A. Snir, A. M. Barry, L. T. MacKenzie, D. J. Mikulis, D. Palmieri, J. L. Bronder, P. S. Steeg, T. Yoneda, I. C. MacDonald, A. F. Chambers, B. K. Rutt and P. J. Foster, *Magn. Reson. Med.*, 2006, **56**, 1001–1010.

262 E. M. Shapiro, S. Skrtic, K. Sharer, J. M. Hill, C. E. Dunbar and A. P. Koretsky, *Proc. Natl. Acad. Sci. U. S. A.*, 2004, **101**, 10901–10906.

263 A. V. Makela, presented in part of World Molecular Imaging Congress (WMIC), Montreal, September 2019.

264 B. Laffon, N. Fernandez-Bertolez, C. Costa, F. Brandao, J. P. Teixeira, E. Pasaro and V. Valdiglesias, *Adv. Exp. Med. Biol.*, 2018, **1048**, 199–213.

265 M. Geppert, M. C. Hohnholt, S. Nurnberger and R. Dringen, *Acta Biomater.*, 2012, **8**, 3832–3839.

266 M. Geppert, M. C. Hohnholt, K. Thiel, S. Nurnberger, I. Grunwald, K. Rezwan and R. Dringen, *Nanotechnology*, 2011, **22**, 145101.

267 C. Costa, F. Brandao, M. J. Bessa, S. Costa, V. Valdiglesias, G. Kilic, N. Fernandez-Bertolez, P. Quaresma, E. Pereira, E. Pasaro, B. Laffon and J. P. Teixeira, *J. Appl. Toxicol.*, 2016, **36**, 361–372.

268 R. Weissleder, D. D. Stark, B. L. Engelstad, B. R. Bacon, C. C. Compton, D. L. White, P. Jacobs and J. Lewis, *AJR, Am. J. Roentgenol.*, 1989, **152**, 167–173.

269 S. Laurent, J. L. Bridot, L. V. Elst and R. N. Muller, *Future Med. Chem.*, 2010, **2**, 427–449.

270 M. Hidalgo, F. Amant, A. V. Biankin, E. Budinska, A. T. Byrne, C. Caldas, R. B. Clarke, S. de Jong, J. Jonkers, G. M. Maelandsmo, S. Roman-Roman, J. Seoane, L. Trusolino and A. Villanueva, *Cancer Discovery*, 2014, **4**, 998–1013.

271 N. N. Knier, V. P. Dubois, Y. Chen, J. A. Ronald and P. J. Foster, *J. Biol. Methods*, 2021, **8**, e154.

272 K. M. Parkins, K. P. Melo, Y. Chen, J. A. Ronald and P. J. Foster, *Nanoscale*, 2021, **13**, 6016–6023.

273 T. L. Whiteside, *Oncogene*, 2008, **27**, 5904–5912.

274 C. Fink, M. Smith, O. C. Sehl, J. M. Gaudet, T. C. Meagher, N. A. Sheikh, J. D. Dikeakos, M. J. Rieder, P. J. Foster and G. A. Dekaban, *Diagn. Interv. Imaging*, 2020, **101**, 577–588.

275 R. Rohani, S. N. Chickera, C. Willert, Y. Chen, G. A. Dekaban and P. J. Foster, *Mol. Imaging Biol.*, 2011, **13**, 679–694.

276 E. Obeid, R. Nanda, Y. X. Fu and O. I. Olopade, *Int. J. Oncol.*, 2013, **43**, 5–12.

277 A. V. Makela, J. M. Gaudet, M. A. Schott, O. C. Sehl, C. H. Contag and P. J. Foster, *Mol. Imaging Biol.*, 2020, **22**, 958–968.

278 A. V. Makela, J. M. Gaudet and P. J. Foster, *Sci. Rep.*, 2017, **7**, 42109.

279 A. V. Makela and P. J. Foster, *Magn. Reson. Med.*, 2018, **80**, 1138–1147.

280 M. Gerosa, G. Ren, Y. Zhang, P. W. Goodwill, J. Mansfield, P. Marzola and M. Wintermark, *Int. J. Magn. Part. Imaging*, 2020, **6**, 2009029.

281 J. Mansfield, presented in part of World Molecular Imaging Congress (WMIC), Virtual, October 2020.

282 I. Baccelli, A. Schneeweiss, S. Riethdorf, A. Stenzinger, A. Schillert, V. Vogel, C. Klein, M. Saini, T. Bäuerle, M. Wallwiener, T. Holland-Letz, T. Höfner, M. Sprick, M. Scharpff, F. Marmé, H. P. Sinn, K. Pantel, W. Weichert and A. Trumpp, *Nat. Biotechnol.*, 2013, **31**, 539–544.

283 A. Rivera-Rodriguez, L. B. Hoang-Minh, A. Chiu-Lam, N. Sarna, L. Marrero-Morales, D. A. Mitchell and C. M. Rinaldi-Ramos, *Nanotheranostics*, 2021, **5**, 431–444.

284 S. Lefevre, D. Ruimy, F. Jehl, A. Neuville, P. Robert, C. Sordet, M. Ehlinger, J. L. Dietemann and G. Bierry, *Radiology*, 2011, **258**, 722–728.

285 S. G. Ruehm, C. Corot, P. Vogt, S. Kolb and J. F. Debatin, *Circulation*, 2001, **103**, 415–422.

286 D. B. Mangarova, J. Brangsch, A. Mohtashamdolatshahi, O. Kosch, H. Paysen, F. Wiekhorst, R. Klopfleisch, R. Buchholz, U. Karst, M. Taupitz, J. Schnorr, B. Hamm and M. R. Makowski, *Sci. Rep.*, 2020, **10**, 12410.

287 W. Zakrzewski, M. Dobrzynski, M. Szymonowicz and Z. Rybak, *Stem Cell Res. Ther.*, 2019, **10**, 68.

288 M. F. Kircher, S. S. Gambhir and J. Grimm, *Nat. Rev. Clin. Oncol.*, 2011, **8**, 677–688.

289 M. Zhang, X. Liu, J. Huang, L. Wang, H. Shen, Y. Luo, Z. Li, H. Zhang, Z. Deng and Z. Zhang, *Nanomedicine*, 2018, **14**, 2475–2483.

290 M. Edmundson, N. T. Thanh and B. Song, *Theranostics*, 2013, **3**, 573–582.

291 F. Chen, M. Ma, J. Wang, F. Wang, S. X. Chern, E. R. Zhao, A. Jhunjhunwala, S. Darmadi, H. Chen and J. V. Jokerst, *Nanoscale*, 2017, **9**, 402–411.

292 M. Hofmann, K. C. Wollert, G. P. Meyer, A. Menke, L. Arseniev, B. Hertenstein, A. Ganser, W. H. Knapp and H. Drexler, *Circulation*, 2005, **111**, 2198–2202.

293 F. Fidler, M. Steinke, A. Kraupner, C. Grüttner, K. H. Hiller, A. Briel, F. Westphal, H. Walles and P. M. Jakob, *IEEE Trans. Magn.*, 2015, **51**, 5100704.

294 J. W. M. Bulte, P. Walczak, M. Janowski, K. M. Krishnan, H. Arami, A. Halkola, B. Gleich and J. Rahmer, *Tomography*, 2015, **1**, 91–97.

295 K. Lüdtke-Buzug, D. H. Rapoport and D. Schneider, *AIP Conf. Proc.*, 2010, **1311**, 244–248.

296 B. Zheng, M. P. von See, E. Yu, B. Gunel, K. Lu, T. Vazin, D. V. Schaffer, P. W. Goodwill and S. M. Conolly, *Theranostics*, 2016, **6**, 291–301.

297 H. S. Kim, S. Y. Oh, H. J. Joo, K. R. Son, I. C. Song and W. K. Moon, *NMR Biomed.*, 2010, **23**, 514–522.

298 S. Schrepfer, T. Deuse, H. Reichenspurner, M. P. Fischbein, R. C. Robbins and M. P. Pelletiera, *Transplant. Proc.*, 2007, **39**, 573–576.

299 O. C. Sehl and P. J. Foster, *Sci. Rep.*, 2021, **11**, 22198.

300 A. A. Dayem, S. B. Lee, K. Kim, K. M. Lim, T. I. Jeon and S. G. Cho, *BMB Rep.*, 2019, **52**, 295–303.

301 Y. Wang, C. Blanco-Andujar, Z. L. Zhi, P. W. So, N. T. Thanh and J. C. Pickup, *Chem. Commun.*, 2013, **49**, 7255–7257.

302 P. Wang, P. W. Goodwill, P. Pandit, J. Gaudet, A. Ross, J. Wang, E. Yu, D. W. Hensley, T. C. Doyle, C. H. Contag, S. Conolly and A. Moore, *Quant. Imaging Med. Surg.*, 2018, **8**, 114–122.

303 A. Sun, presented in part of World Molecular Imaging Congress (WMIC), Virtual, October 2020.

304 H. Hayat, A. Sun, H. Hayat, S. Liu, N. Talebloo, C. Pinger, J. O. Bishop, M. Gudi, B. F. Dwan, X. Ma, Y. Zhao, A. Moore and P. Wang, *Mol. Imaging Biol.*, 2021, **23**, 18–29.

305 T. Kuboyabu, A. Ohki, N. Banura and K. Murase, *Open J. Med. Imaging*, 2016, **6**, 33–41.

306 Y. Zhang, presented in part of World Molecular Imaging Congress (WMIC), Virtual, October 2020.

307 P. C. Liang, Y. C. Chen, C. F. Chiang, L. R. Mo, S. Y. Wei, W. Y. Hsieh and W. L. Lin, *Int. J. Nanomed.*, 2016, **11**, 2021–2037.

308 K. Li, H. Nejadnik and H. E. Daldrup-Link, *Drug Discovery Today*, 2017, **22**, 1421–1429.

309 B. K. Lee, Y. H. Yun and K. Park, *Chem. Eng. Sci.*, 2015, **125**, 158–164.

310 C. Aversa, V. Rossi, E. Geuna, R. Martinello, A. Milani, S. Redana, G. Valabrega, M. Aglietta and F. Montemurro, *Breast*, 2014, **23**, 623–628.

311 G. Jia, Y. Han, Y. An, Y. Ding, C. He, X. Wang and Q. Tang, *Biomaterials*, 2018, **178**, 302–316.

312 T. Yang, P. Martin, B. Fogarty, A. Brown, K. Schurman, R. Phipps, V. P. Yin, P. Lockman and S. Bai, *Pharm. Res.*, 2015, **32**, 2003–2014.

313 V. Toomajian, E. E. Ural, C. H. Contag and A. V. Makela, presented in part of World Molecular Imaging Congress (WMIC), Virtual, October 2020.

314 K. O. Jung, H. Jo, J. H. Yu, S. S. Gambhir and G. Pratx, *Biomaterials*, 2018, **177**, 139–148.

315 P. Chandrasekharan, Z. W. Tay, D. Hensley, X. Y. Zhou, B. K. L. Fung, C. Colson, Y. Lu, B. D. Fellows, Q. Huynh, C. Saayujya, E. Yu, R. Orendorff, B. Zheng, P. W. Goodwill, C. Rinaldi and S. M. Conolly, *Theranostics*, 2020, **10**, 2965–2981.

316 A. Hervault and N. T. Thanh, *Nanoscale*, 2014, **6**, 11553–11573.

317 S. Laurent, S. Dutz, U. O. Hafeli and M. Mahmoudi, *Adv. Colloid Interface Sci.*, 2011, **166**, 8–23.

318 R. K. Gilchrist, R. Medal, W. D. Shorey, R. C. Hanselman, J. C. Parrott and C. B. Taylor, *Ann. Surg.*, 1957, **146**, 596–606.

319 A. A. Sousa-Junior, S. A. Mendanha, M. S. Carriao, G. Capistrano, A. G. Prospero, G. A. Soares, E. R. Cintra, S. F. O. Santos, N. Zufelato, A. Alonso, E. M. Lima, J. R. A. Miranda, E. P. Silveira-Lacerda, C. G. Cardoso and A. F. Bakuzis, *Mol. Pharm.*, 2020, **17**, 837–851.

320 Y. Lu, A. Rivera-Rodriguez, Z. W. Tay, D. Hensley, K. L. B. Fung, C. Colson, C. Saayujya, Q. Huynh, L. Kabuli, B. Fellows, P. Chandrasekharan, C. Rinaldi and S. Conolly, *Int. J. Hyperthermia*, 2020, **37**, 141–154.

321 C. Kut, Y. Zhang, M. Hedayati, H. Zhou, C. Cornejo, D. Bordelon, J. Mihalic, M. Wabler, E. Burghardt, C. Gruettner, A. Geyh, C. Brayton, T. L. Deweese and R. Ivkov, *Nanomedicine*, 2012, **7**, 1697–1711.

322 R. Dhavalikar and C. Rinaldi, *J. Magn. Magn. Mater.*, 2016, **419**, 267–273.

323 A. R. Sebastian, S. H. Ryu, H. M. Ko and S. H. Kim, *IEEE Access*, 2019, **7**, 96094–96104.

324 E. Y. Yu, P. W. Goodwill and S. M. Conolly, *Preliminary characterization of a laminated iron-core 6.3 T/m FFL magnet*, IEEE, New York, 2015.

325 J. M. Gaudet, presented in part of World Molecular Imaging Congress (WMIC), Virtual, October 2020.

326 M. S. A. Darwish, H. Kim, M. P. Bui, T. A. Le, H. Lee, C. Ryu, J. Y. Lee and J. Yoon, *Nanomaterials*, 2021, **11**, 1096.

327 A. P. Khandhar, R. M. Ferguson, J. A. Simon and K. M. Krishnan, *J. Biomed. Mater. Res., Part A*, 2012, **100**, 728–737.

328 A. Jordan, R. Scholz, P. Wust, H. Schirra, T. Schiestel, H. Schmidt and R. Felix, *J. Magn. Magn. Mater.*, 1999, **194**, 185–196.

329 X. L. Liu, H. M. Fan, J. B. Yi, Y. Yang, E. S. G. Choo, J. M. Xue, D. D. Fana and J. Ding, *J. Mater. Chem.*, 2012, **22**, 8235–8244.

330 H. Khurshid, J. Alonso, Z. Nemati, M. H. Phan, P. Mukherjee, M. L. Fdez-Gubieda, J. M. Barandiarán and H. Srikanth, *J. Appl. Phys.*, 2015, **117**, 17A337.

331 J. F. Liu, N. Neel, P. Dang, M. Lamb, J. McKenna, L. Rodgers, B. Litt, Z. Cheng, A. Tsourkas and D. Issadore, *Small*, 2018, **14**, e1802563.

332 S. Maruyama, K. Shimada, K. Enmeiji and K. Murase, *Int. J. Nanomed. Nanosurg.*, 2016, **2**, 1–11.

333 E. G. Fuller, H. Sun, R. D. Dhavalikar, M. Unni, G. M. Scheutz, B. S. Sumerlin and C. Rinaldi, *ACS Appl. Polym. Mater.*, 2019, **1**, 211–220.

334 M. Wintermark, M. Sesay, E. Barbier, K. Borbely, W. P. Dillon, J. D. Eastwood, T. C. Glenn, C. B. Grandin, S. Pedraza, J. F. Soustiel, T. Nariai, G. Zaharchuk, J. M. Caille, V. Dousset and H. Yonas, *Stroke*, 2005, **36**, e83–e99.

335 R. E. Latchaw, H. Yonas, G. J. Hunter, W. T. Yuh, T. Ueda, A. G. Sorensen, J. L. Sunshine, J. Biller, L. Wechsler, R. Higashida, G. Hademenos and A. Council on Cardiovascular Radiology of the American Heart, *Stroke*, 2003, **34**, 1084–1104.

336 X. Huang, D. Kalladka, B. K. Cheripelli, F. C. Moreton and K. W. Muir, *J. Neuroimaging*, 2017, **27**, 602–606.

337 N. D. Forkert, P. Kaesemann, A. Treszl, S. Siemonsen, B. Cheng, H. Handels, J. Fiehler and G. Thomalla, *AJNR Am. J. Neuroradiol.*, 2013, **34**, 1697–1703.

338 H. Q. Dam, D. C. Brandon, V. V. Grantham, A. J. Hilson, D. M. Howarth, A. H. Maurer, M. G. Stabin, M. Tulchinsky, H. A. Ziessman and L. S. Zuckier, *J. Nucl. Med. Technol.*, 2014, **42**, 308–317.

339 S. C. Srivastava and L. R. Chervu, *Semin. Nucl. Med.*, 1984, **14**, 68–82.

340 F. Wegner, T. M. Buzug and J. Barkhausen, *Theranostics*, 2018, **8**, 3691–3692.

341 K. Miles, *Cancer Imaging*, 2011, **11**, S86–S92.

342 J. V. Frangioni, *J. Clin. Oncol.*, 2008, **26**, 4012–4021.

343 K. Greish, *J. Drug Targeting*, 2007, **15**, 457–464.

344 N. Schleich, C. Po, D. Jacobs, B. Ucakar, B. Gallez, F. Danhier and V. Preat, *J. Controlled Release*, 2014, **194**, 82–91.

345 P. Vogel, M. A. Ruckert, P. Klauer, W. H. Kullmann, P. M. Jakob and V. C. Behr, *Phys. Med. Biol.*, 2016, **61**, 6620–6634.

346 A. Mohtashamdolatshahi, H. Kratz, O. Kosch, R. Hauptmann, N. Stolzenburg, F. Wiekhorst, I. Sack, B. Hamm, M. Taupitz and J. Schnorr, *Sci. Rep.*, 2020, **10**, 17247.

347 M. G. Kaul, J. Salamon, T. Knopp, H. Ittrich, G. Adam, H. Weller and C. Jung, *Phys. Med. Biol.*, 2018, **63**, 064001.

348 I. Molwitz, H. Ittrich, T. Knopp, T. Mummert, J. Salamon, C. Jung, G. Adam and M. G. Kaul, *Physiol. Meas.*, 2019, **40**, 105002.

349 J. K. Lewis, J. C. Bischof, I. Braslavsky, K. G. Brockbank, G. M. Fahy, B. J. Fuller, Y. Rabin, A. Tocchio, E. J. Woods, B. G. Wowk, J. P. Acker and S. Giwa, *Cryobiology*, 2016, **72**, 169–182.

350 A. Chiu-Lam, E. Staples, C. J. Pepine and C. Rinaldi, *Sci. Adv.*, 2021, **7**, eabe3005.

351 M. L. Etheridge, Y. Xu, L. Rott, J. Choi, B. Glasmacher and J. C. Bischof, *Technology*, 2014, **2**, 229–242.

352 J. Haegele, S. Vaalma, N. Panagiotopoulos, J. Barkhausen, F. M. Vogt, J. Borgert and J. Rahmer, *Phys. Med. Biol.*, 2016, **61**, N415.

353 S. H. Han, E. Cho, D. K. Lee, G. Cho, Y. R. Kim and H. Cho, *Phys. Med. Biol.*, 2014, **59**, 6521.

354 D. Hensley, P. W. Goodwill, L. Croft and S. Conolly, *Preliminary experimental X-space color MPI*, IEEE, New York, 2015.

355 D. Hensley, PhD Thesis, UC Berkeley, 2017.

356 Y. Muslu, M. Utkur, O. M. Demirel and E. U. Saritas, *IEEE Trans. Med. Imaging*, 2018, **37**, 1920–1931.

357 J. Haegele, N. Panagiotopoulos, S. Cremers, J. Rahmer, J. Franke, R. L. Duschka, S. Vaalma, M. Heidenreich, J. Borgert, P. Borm, J. Barkhausen and F. M. Vogt, *IEEE Trans. Med. Imaging*, 2016, **35**, 2312–2318.

358 J. Rahmer, D. Wirtz, C. Bontus, J. Borgert and B. Gleich, *IEEE Trans. Med. Imaging*, 2017, **36**, 1449–1456.

359 K. Murase, R. Song and S. Hiratsuka, *Appl. Phys. Lett.*, 2014, **104**, 252409.

360 J. B. Weaver, A. M. Rauwerdink and E. W. Hansen, *Med. Phys.*, 2009, **36**, 1822–1829.

361 C. Stehning, B. Gleich and J. Rahmer, *Int. J. Magn. Part. Imaging*, 2016, **2**, 1612001.

362 S. Draack, F. Ludwig, M. Schilling and T. Viereck, *J. Magn. Magn. Mater.*, 2021, **522**, 167478.

363 M. Möddel, C. Meins, J. Dieckhoff and T. Knopp, *New J. Phys.*, 2018, **20**, 083001.

364 N. Gdaniec, P. Szwargulski and T. Knopp, *Med. Phys. Lett.*, 2017, **44**, 6456–6460.

365 T. Knopp and M. Hofmann, *Phys. Med. Biol.*, 2016, **61**, N257–N267.

366 K. Lu, P. Goodwill, B. Zheng and S. Conolly, *IEEE Trans. Med. Imaging*, 2018, **37**, 1989–1998.

367 M. Storath, C. Brandt, M. Hofmann, T. Knopp, J. Salamon, A. Weber and A. Weinmann, *IEEE Trans. Med. Imaging*, 2017, **36**, 74–85.

368 A. Tateo, A. Iurino, G. Settanni, A. Andrisani, P. F. Stifanelli, P. Larizza, F. Mazzia, R. M. Mininni, S. Tangaro and R. Bellotti, *Phys. Med. Biol.*, 2016, **61**, 4061–4077.

369 A. Weber, F. Werner, J. Weizenecker, T. M. Buzug and T. Knopp, *Phys. Med. Biol.*, 2016, **61**, 475–487.

370 X. J. Chen, X. Han and X. Y. Tang, *J. Med. Imaging Health Inf.*, 2021, **11**, 703–711.

371 K. Murase, *Jpn. J. Appl. Phys.*, 2021, **60**, 088001.

372 F. Lieb and T. Knopp, *Med. Phys.*, 2021, **48**, 3893–3903.

373 A. von Gladiss, M. Graeser, A. Behrends, X. Chen and T. M. Buzug, *Sci. Rep.*, 2020, **10**, 18432.

374 H. Bernd, E. De Kerviler, S. Gaillard and B. Bonnemain, *Invest. Radiol.*, 2009, **44**, 336–342.

375 D. T. Kehagias, A. D. Gouliamos, V. Smyrniotis and L. J. Vlahos, *J. Magn. Reson. Imaging*, 2001, **14**, 595–601.

376 A. Singh, T. Patel, J. Hertel, M. Bernardo, A. Kausz and L. Brenner, *Am. J. Kidney Dis.*, 2008, **52**, 907–915.

377 E. U. Saritas, P. W. Goodwill, G. Z. Zhang and S. M. Conolly, *IEEE Trans. Med. Imaging*, 2013, **32**, 1600–1610.

378 I. Schmale, B. Gleich, J. Rahmer, C. Bontus, J. Schmidt and J. Borgert, *IEEE Trans. Magn.*, 2015, **51**, 6502604.

379 O. Dossel and J. Bohnert, *Biomed. Tech.*, 2013, **58**, 611–621.

380 M. Graeser, P. Ludewig, P. Szwargulski, F. Foerger, T. Liebing, N. D. Forkert, F. Thieben, T. Magnus and T. Knopp, *Phys. Med. Biol.*, 2020, **65**, 235007.

381 J. Pagan, C. McDonough, T. Vo and A. Tonyushkin, *IEEE Trans. Magn.*, 2021, **57**, 5300105.

382 E. E. Mason, C. Z. Cooley, S. F. Cauley, M. A. Griswold, S. M. Conolly and L. L. Wald, *Int. J. Magn. Part. Imaging*, 2017, **3**, 1703008.

383 M. Graeser, F. Thieben, P. Szwargulski, F. Werner, N. Gdaniec, M. Boberg, F. Griese, M. Moddel, P. Ludewig, D. van de Ven, O. M. Weber, O. Woywode, B. Gleich and T. Knopp, *Nat. Commun.*, 2019, **10**, 1936.

384 E. E. Mason, E. Mattingly, K. Herb, M. Sliwiak, S. Franconi, C. Z. Cooley, P. J. Slanetz and L. L. Wald, *Sci. Rep.*, 2021, **11**, 13456.